Design and development of High Current Radio-Frequency Quadrupole Accelerator

By

Sista V Lalitha Sanyasirao

(Enrollment No : PHYS 01200704018)

Bhabha Atomic Research Centre

Mumbai 400 085, India

A thesis submitted to the

Board of Studies in Physical Sciences

In partial fullfillment of requirements

for the Degree of

DOCTOR OF PHILOSOPHY

of

HOMI BHABHA NATIONAL INSTITUTE

November, 2014

Homi Bhabha National Institute

Recommendations of the Viva Voce Board

As members of the Viva Voce Board, we certify that we have read the dissertation prepared by Sista V Lalitha Sanyasirao entitled "Design and Development of High Current Radio-Frequency Quadrupole Accelerator" and recommend that it may be accepted as fulfilling the dissertation requirement for the Degree of Doctor of Philosophy.

		Date: 7/11/2014
Chairman:	**Prof. S. Kailas**	
		Date: 7/11/2014
Guide\Convenor:	**Prof. P. Singh**	
	Kailash C. Mittal	**Date:** 7/11/2014
Member 1:	**Prof. K. C. Mittal**	
	Absent	**Date:**
Member 2:	**Prof. Alok Chakrabarti**	
	D Kanjilal	**Date:** 07/11/2014
External Examiner:	**Prof. D. Kanjilal**	
		Date: 7/11/2014
Invitee:	**Prof. V. S. Pandit**	

Final approval and acceptance of this dissertation is contingent upon the candidate's submission of final copies of the dissertation to HBNI. I hereby certify that I have read this dissertation prepared under my direction and recommend that it may be accepted as fulfilling the dissertation requirement.

Date: 7.11.2014

7.11.2014

Place: Mumbai **Guide: Prof. P. Singh**

STATEMENT BY AUTHOR

This dissertation has been submitted in partial fulfillment of requirements for an advanced degree at Homi Bhabha National Institute (HBNI) and is deposited in the Library to be made available to borrowers under rules of the HBNI.

Brief quotations from this dissertation are allowable without special permission, provided that accurate acknowledgement of source is made. Requests for permission for extended quotation from or reproduction of this manuscript in whole or in part may be granted by the Competent Authority of HBNI when in his or her judgement the proposed use of the material is in the interests of scholarship. In all other instances, however, permission must be obtained from the author.

Sista V Lalitha Sanyasirao

DECLARATION

I, here by declare that the investigation presented in the thesis has been carried out by me. The work is original and has not been submitted earlier as a whole or in part for a degree/diploma at this or any other Institution / University.

Sista V Lalitha Sanyasirao

List of Publications:

Journal Publications:

1. Design, development and acceleration trials of Radio-frequency quadrupole, S.V.L.S Rao, Piyush Jain, Rajni Pande, Shweta Roy, Jose Mathew, Rajesh Kumar, Manjiri Pande, Srinivas Krishnagopal, S K Gupta and Pitamber Singh, Rev. Sci. Instrum. 85, 043304 (2014).

2. Design studies of a high current RFQ for ADS programme, S.V.L.S Rao and P. Singh, Pramana. J. Physics, Vol.74, No.2, February 2010, pp. 247-259.

3. An improved permanent magnet quadrupole design with larger good field region for high intensity proton linacs, Jose V Mathew, S. V. L. S Rao, S. Krishnagopal, P Singh, Nuclear Instruments and Methods in Physics Research A 727 (2013) 12-20.

4. Role of Beam dynamics studies for accelerator safety, P Singh, S. V. L. S. Rao and Rajni Pande, Indian Journal of Pure & Applied Physics, Vol. 50, July 2012, pp. 439-441.

5. Physics design of a CW high-power Linac for accelerator-driven system, Rajni Pande, Shweta Roy, S.V.L.S Rao, P. Singh and S. Kailas, Pramana. J. Physics, Vol.78, No.2, February 2012, pp. 247-255.

6. Optimization of 1 MeV RFQ accelerator parameters for 9Be(d,n)10B based pulsed neutron source, A. K. Singh, R Baskaran, T. S. Selvakumaran, V L S Rao Sista and P Singh, Indian Journal of Pure & Applied Physics, Vol. 49, January 2011, pp. 13-20.

7. Note: Studies on target placement in TE_{111} cylindrical cavity of electron cyclotron resonance x-ray source for the enhancement of x-ray dose, T. S. Selvakumaran, R. Baskaran, A. K. Singh and V.L.S. Rao Sista, Rev. Sci. Instrum. 81, 036104 (2010).

Conference publications:

1. Low Energy High Intensity Proton Accelerator project at BARC, V.L.SRao Sista, DAE-BRNS workshop on Cyclotrons: Rising Expectations and Mounting Challenges, Jun 25-26, 2008.

2. Dipole stabilizer rods for 400 keV deuteron RFQ, V.L.S Rao Sista, S.C.L. Srivastava, Rajni Pande, Shweta Roy, P. Singh, InPAC-2009, 10-14 February, 2009, RRCAT, Indore

3. Low energy proton linac development at BARC for ADS program, S.V.L.S Rao, Rajni Pande, Shweta Roy, Piyush Jain, Rajesh Kumar, S. Krishnagopal, P. Singh, P.K. Nema, R.K. Choudhury, S. Kailas & V.C. Sahni, International Conference on Peaceful Uses of Atomic Energy-2009, Sept 29-Oct 1, 2009, New Delhi, Page 498.

4. Beam dynamics studies of Radio Frequency Quadrupole accelerator for Project-X, S.V.L.S. Rao, Nikolay Solyak, C.S. Mishra, Rajni Pande, Shweta Roy and P.Singh, InPAC-2011, 15-18 February, 2011, IUAC, New Delhi.

5. Development & characterization of Prototype RFQ at BARC, S.V.L.S. Rao, Piyush Jain, Rajni Pande, Shweta Roy, Rajesh Kumar, M.R. Mishra, Gireesh Singh, L.D Tayade, P.R Parate, Sumit Garg, S.Krishnagopal, P.Singh, P.K.Nema and S. Kailas, InPAC-2011, 15-18 February, 2011, IUAC, New Delhi.

6. Design, Development and Acceleration experiments of a four-vane RFQ at BARC, S.V.L.S Rao, Piyush Jain, Jose V. Mathew, Rajni Pande, Shweta Roy, S. Shrotriya, N. Patel, Shiju, M. R. Mishra, Gireesh Singh, L. Tayade, Praveen P, B. M. Kukreti, Rajesh Kumar, Manjiri Pande, S. Krishnagopal, S. K. Gupta, P. Singh, InPAC-2013, 19-22 November, 2013, VECC, Kolkata.

7. Transverse emittance measurement studies of a Deuteron Ion source beam, Jose V. Mathew, S. V. L. S. Rao, Rajni Pande, M. R. Mishra, L. D. Tayade, P. R. Parate, P. Singh, InPAC-2013, November 19-22 November, 2013, VECC, Kolkata. .

8. An Improved Permanent Magnet Quadrupole Design with Larger Good Field Region for High Intensity Proton Linacs, Jose V. Mathew, S. V. L. S Rao, S. Krishnagopal and P. Singh, InPAC-2013, 19-22, November, 2013, VECC, Kolkata. .

9. Design of Superconducting RF structures for a Superconducting Proton Linac, Rajni Pande, Shweta Roy, S. V. L. S. Rao, S. Krishnagopal, P. Singh, InPAC 2013, 19-22 November, 2013, VECC, Kolkata. .

10. Design & Development of LEBT for LEHIPA Project, Rajni Pande, Shweta Roy, S.V.L.S. Rao, M.R. Mishra and P.Singh, InPAC-2011, 15-18 February, 2011, IUAC, New Delhi.

11. A LEBT for the 400 keV RFQ based Neutron Generator at BARC, Rajni Pande, S.V.L.S.Rao, Shweta Roy, M.R. Mishra, L.D. Tayade, P.R Parate, Sapna P, Shailaja Ware, S.K.Singh, A. Agarwal, S.K. Gupta, P. Singh, InPAC-2011, 15-18 February,2011, IUAC, New Delhi..

12. RF characterization of DTL Prototype, Shweta Roy, S.V.L.S.Rao, Rajni Pande, Piyush Jain, Sumit Garg, Gireesh Singh, S.Krishnagopal and P.Singh, InPAC-2011, 15-18 February, 2011, IUAC, New Delhi..

13. Manufacturing Design and status of LEHIPA RFQ, Piyush Jain, S.V.L.S.Rao, P.K. Nema, S.Krishnagopal and P.Singh, InPAC-2011, 15-18 February, 2011, IUAC, New Delhi.

14. Frequency analysis and field-stabilization for the LEHIPA DTL prototype, Shweta Roy, S.C.L. Srivastava, Rajni Pande, V.L.S. Rao Sista, S. Krishnagopal and P. Singh, Ind. Particle Accelerator Conf. (InPAC-2009), 10-14 February, 2009, RRCAT, Indore.

15. Design Studies of a 650 MeV Proton Linac for MPRR, Rajni Pande, Shweta Roy, V.L.S Rao Sista, P. Singh, P.K. Nema and R.K. Choudhury, InPAC-2009, 10-14 February, 2009, RRCAT, Indore.

16. High intensity accelerator development for ADS, P. Singh, Rajni Pande, Shweta Roy and S.V.L.S Rao, Indian Nuclear Society News, Vol. 6, No. 2 April-June 2009, p 21-29.

17. Developmental Studies of High Current Proton Linac for ADS Program, P. Singh, S.V.L.S. Rao, Rajni Pande, Shweta Roy, Rajesh Kumar, Piyush Jain, P.K. Nema, S. Krishnagopal, R. K. Choudhury, S. Kailas, V.C. Sahni, International Topical Meeting on Nuclear Research Applications and Utilization of Accelerators, May 4-8, '09, Vienna, Austria.

18. A compact RFQ Linac based pulsed neutron source, A.K. Singh, T.S.Selvakumaran, R. Baskaran, S.V.L.S.Rao and P. Singh, InPAC-2009, 10-14 February, 2009, RRCAT, Indore.

19. RF coupler development for LEHIPA, Rajesh kumar, Piyush Jain, S.V.L.S. Rao, Manish Kumar, P.K. Biswas, S. Guha, S. B. Jawale, P.K. Nema and P. Singh, InPAC-2009, 10-14 February, 2009, RRCAT, Indore.

Sista V Lalitha Sanyasirao

I Dedicate this to My Parents (S Venugopal, Bramaramba), Wife (Swarna) and Son (Saishoumik)

Acknowledgments

I would like to express my heartful gratitude to my mentor and guide Dr. P. Singh, Head, Ion Accelerator Development Division, BARC for guidance, support and encouragement during the entire period. His parental affection, infectious optimism, bright spirits and belief in me were invaluable at every stumble or wrong turn. He provided a pleasant working environment in the lab. Words can never be enough to thank him and I will remain indebted forever.

I wish to express my deep gratitude to my doctoral committee members Dr. S. Kailas, Dr. K. C. Mittal and Dr. Alok Chakrabarti for their support and valuable suggestions.I would like to take this opportunity to thank Dr. V. C. Sahni, Former Director, Physics Group, BARC for his interest in this project.

I wish to acknowledge all senior colleagues in division and group for all the help, support and encouragement that they have provided. I take this opportunity to thank Shri S.K. Gupta, Dr. Srinivas Krishnagopal, Smt. Manjiri Pande, Dr. S Santra, Shri Rajesh kumar, Sudheer Singh and Arun Agarwal.

Special thanks are due to my lab mates and friends Rajni pande, Shweta Roy, Piyush Jain, Jose V Mathew, S.C.L Srivastava, Sandip Shrotriya, Sumit Garg and Dr. G. Kondayya for their cooperation, help and pleasure of their company. I would like to thank M.R. Mishra, Gireesh N Singh, L D Tayade, P. Parate, Niranjan Patel and Shiju for their technical assistance.

I will take this opportunity to thank Drs. Arvind Kumar and K. K Pant, RRCAT for their help in using the designing codes and Dr. Vinit Kumar, RRCAT for his suggestions while writing the thesis.

On the personal front, words are not enough to thank my parents for making me what I am. Above all I would reserve my heartiest thanks for my better half, for loving me for who I am. My thesis could never have seen the light of the day without them.

Contents

List of Figures

List of Tables

SYNOPSIS

Radio-frequency quadrupole (RFQ) [1] accelerators are extensively used as injectors in the high current Linacs because of their remarkable capability of simultaneously focussing, bunching and accelerating the low-energy ion beams with high transmission (> 90 %) and minimum emittance growth. However, in any RF accelerator the beam must be longitudinally bunched so that all particles will be accelerated. In a conventional acceleator such as the drift tube Linac (DTL), bunching is accomplished prior to injection into the Linac using one or more RF bunching cavities. In buncher cavities RF electric fields are applied to the DC input beam to produce a velocity modulation in which early particles are decelerated and late partciles are accelerated. After a suitable drift space, the beam becomes bunched, ready for injection into the Linac. The bunching is usually not very efficient, especially for high-current beams because of the high space-charge forces at low energies, since the forces on the particle are proportional to $(1 - \beta^2)$, where $\beta = \frac{v}{c}$ is the velocity. In high-intensity beams, the bunching process causes an increase in the beam density, which increases the space-charge forces further which results in a blow-up of the transverse beam emittance. The conventional DTL linacs are efficient only in the velocity range of $0.04 \leq \beta \leq 0.28$. In order to make the efficient use of DTL structures in older Linacs, the extraction voltage of the ion source was increased to ~ 0.7 MV. These high voltages were generated using the Cockroft Walton generators. The fundamental limitations of the conventional linacs is not only in terms of beam current, but also the reliable operation of HV columns, which is reponsible for the large fraction of machine downtime. However, the RFQ accelerator, proposed by Kapchinskii and Teplyakov in 1970, is well suited for acceleration of beams with low velocities in the range of about 0.01 to 0.1 times the speed of light.

A RFQ uses the velocity independent transverse electric focusing at low energies which gives a significant strong focusing as compared to conventional linacs that use velocity dependent magnetic lenses. This allows one to extend the practical range of operation of RFQs to low velocities, thus eliminating the need for large, high voltage dc accelerators. The RFQs bunch the beam adiabatically and by proper choice of parameters one can achieve a high transmission ($> 90\%$). Because of their high capture efficiency at low energies, the RFQs are well suited as a first unit of all high current RF linear accelerators in many advanced applications, such as Accelerator Driven Systems (ADS) [2] for effective utilization of throium resources, Spallation Neutron Sources (SNS) [3] and production of radioactive ion beams (RIB) [4].

In view of the importance of RFQ accelerators for high-current machines, the R&D activity for the design and development of 2 different continuous wave (CW) RFQs was initiated at BARC, Mumbai.

1. A 400 keV deuteron RFQ [5] for neutron production

2. A 3 MeV, 30 mA Proton RFQ for Low Energy High Intensity Proton accelerator (LEHIPA) [6], which will be used as a front-end injector to 1 GeV Linac for ADS application

The work reported in the thesis deals with the design aspects of these RFQs and characterization of the 400 keV RFQ. It is presented in seven chapters. In chapter 1, we present the brief introduction about the operating principle of a RFQ, a list of existing RFQs and also review the status of various upcoming high current RFQs at different labs. In chapter 2, we present the beam dynamics simulations studies for our 400 keV deuteron RFQ. The beam dynamics studies of RFQ [7] linacs have been extensively done, and a generalized method was used, where the RFQ was divided into four sections, namely radial matching (RM), shaper (SH), gentle buncher (GB) and accelerator (AC) sections. Several design methods have been proposed at different laboratories for minimizing the emittance growth and the resulting beam losses. We have extensively studied two popular design philosophies [8], and compared their advantages and disadvantages from the beam dynamics, fabrication and tuning point of view. Based on these studies, the 400 keV and 3 MeV RFQ's have been designed. The following criteria are kept in mind while designing these RFQs

1. Maximize the beam transmission

2. Minimize the emittance growth

3. Minimize the length

4. Peak surface field <1.8 Kilpatric field (k_p) [9]

Based on these criteria, the optimization of the RFQ parameters was done using the computer code LIDOS [10]. In order to minimize the activation of the structure, it is advisable not to loose the beam at high energies. The distribution of beam losses and energy of the lost particles was studied for 4 different input beam distributions and observed that the losses are concentrated below 200 keV for the 400 keV RFQ and less than 2 MeV for 3 MeV proton RFQ.

In RFQ design, it is crucial to study the effect of errors on the beam dynamics. Various effects such as beam misalignment and tilt, variations in the input energy and vane voltage, etc., can degrade the beam dynamics-typically through reduced transmission and increase of emittance. Further, it is necessary to study not just the effects of individual errors, but also of combination of these errors. Such a study is essential to get an idea of the errors that can be tolerated, which would in turn place limits on the tolerances that are needed in the fabrication of the RFQ, power supplies etc. The effects of various errors (specified above) on beam transmission was studied. Based on these studies the tolerances on the input beam alignments, input energy deviation and energy spread of the input beam have been specified.

In chapter 3, we present the Electromagnetic simulation of the 400 keV deuteron RFQ. The transverse cross-section of the RFQ was optimized using the computer code SUPERFISH [11]. The 2D cavity parameters are optimized based on the following criteria

1. Maximizing the Quality factor

2. Minimizing the peak surface field for a given vane voltage

Effect of various parameters on the resonat frequeny of the RFQ was studied. Based on these studies an empherical formula for frequency variation with respect to three main parameters namely: transverse radius of curvature (ρ_t), average bore radius (r_0) and Corner radius (R_c) was given. This was very helpful, while aligning the vanes before brazing.

The field distribution inside the RFQ cavity should be flat similar to TE_{210}mode. In the closed ideal RFQ the field distribution will be peaked at the center and reduces to zero at the ends of the cavity. In order to produce a longitudinally uniform field throughout the length, the end regions of the RFQ have to be provided with undercuts, which are called end cells [12]. The resonant frequency of these end cells should be equal to the quadrupolar cross sectional frequency, to have a flat field distribution along the length. These end cells were designed using 3D Electromagnetic simulation code CST Microwave studio.

While optimizing the end cells the unwanted dipolar mode frequencies increase and come closer to the desired quadrupolar mode. Since the frequency difference between the modes reduces, the contribution from the dipole mode in the field distribution increase for small mechanical perturbations. In order to separate the modes farther from each other the dipole stabilizer rods (DSRs) are used. The positions of the DSRs are chosen in such a way that they disturb only the dipole modes. The length and radius of the DSRs are optimized in such a way that the dipole mode frequency should be as far as possible from the required quadrupole mode.

In chapter 4, we present the analytical tool which was developed to foresee the effect of geometric perturbations on the voltage profile. In this chapter, we give theory of five conductor transmission line equivalent circuit for the four-vane RFQ and the effects of geometrical pertubations on the voltage profiles are analyzed for some particular cases and are compared with simulated results. Based on this theory, we have developed a tuning algorithm for our 400 keV RFQ. The goal of tuning program is to reduce the perturbative components up to a desired value, typically chosen by beam transmission considerations. Initially when the field distribution is measured, we assume that the errors in the field are due to capacitive errors. From the perturbative analysis we can calculate the capacitive errors which are responsible for the measured field distribution. Then we will calculate the required inductance to compensate these capacitive errors. With the help of the tuners located at discrete positions these inductances can be introduced, which leads to the required field distribution. The input for this tuning alogirthm was the measured field distribution, Based on this it will give the depth of the tuners required in order to have desired field distribution. A particular case study was performed in order to validate this algorithm.

Based on these simulation studies a 400 keV deuteron RFQ has been built.. The vacuum brazing of the RFQ has been done in two stages. In the first stage, all the 4 vanes are brazed (i.e., copper to copper) and in the second stage the ports and end flanges are brazed (i.e., copper to SS). The brazed RFQ along with bead pull measurement setup is shown in Figure 1.

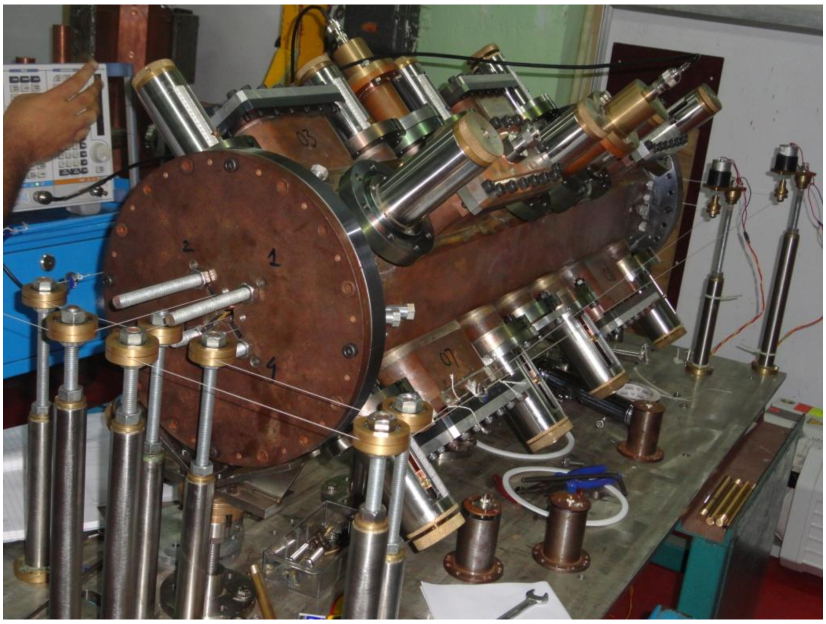

Figure 0.1: 400 keV RFQ along with bead pull measurement setup

The low power RF characterization, which mainly involves the meaurement of Quality factor, resonant frequency and field distribution (using bead pull system) of the RFQ, high power condition and beam commissioning was done and the results of these measurements are presented in chapter 5. In order to have a flat field distribution in 400 keV RFQ, we have used our tuning program and after 7 iterations, the quadrupole field levels were tuned within ± 5 % ($^{dQ}/_{Q_0}$) and dipole contibution $<$ 4 % ($^{d1}/_{Q_0}$,$^{d2}/_{Q_0}$), where $Q_0$is the average quadrupole mode. While tuning the RFQ for field flatness, the resonant frequency was measured to be 352.48 MHz which is more than the desired frequency (350 MHz). In order to tune the RFQ to the desired frequency without disturbing the field flatness, the tuners have to be moved outward in such a way that the frequency shift because of each tuner should be equal to 0.16 MHz. The field distribution results are shown in Figure 2.

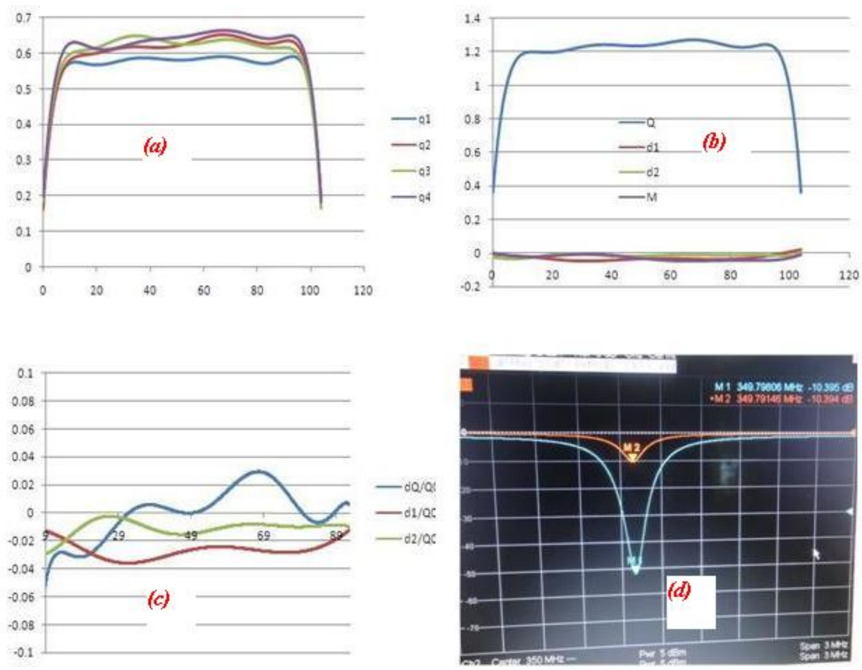

Figure 0.2: (a) Field distribution in all the 4 quadrants (b) Quadrupole and dipole mode contributions in field (c) Deviation of field with average quadrupole field (d) s11, s22 reflection measurements

In order to avoid the neutron production by deuteron beam, inital beam trials were done using the proton beam. The beam dynamics simulations to accelerate the proton in this RFQ have been done. Since the RFQ is a constant $\beta(\frac{v}{c})$ structure, so the input energy and the intervane voltage has to be halved to accelerate the proton beam. The intervane voltage needed to accelerate the proton beam is ˜ 22 kV, which corresponds to the input power of ˜ 15 kW. In order to validate our calculations high power RF ($\sim$ 30 kW) conditioning of the RFQ has been done in pulsed mode. The proton beam of input energy 25 keV was injected into the RFQ and accelerated the beam to 200 keV . The variation of the output proton beam energy and transmission with the input RF power has been studied. The 200 keV proton RFQ beam line is shown in Figure 3. The output beam energy was measured using a 90^0deg bending magnet and the results shown in Figure 4 was in good agreement with the simulations.

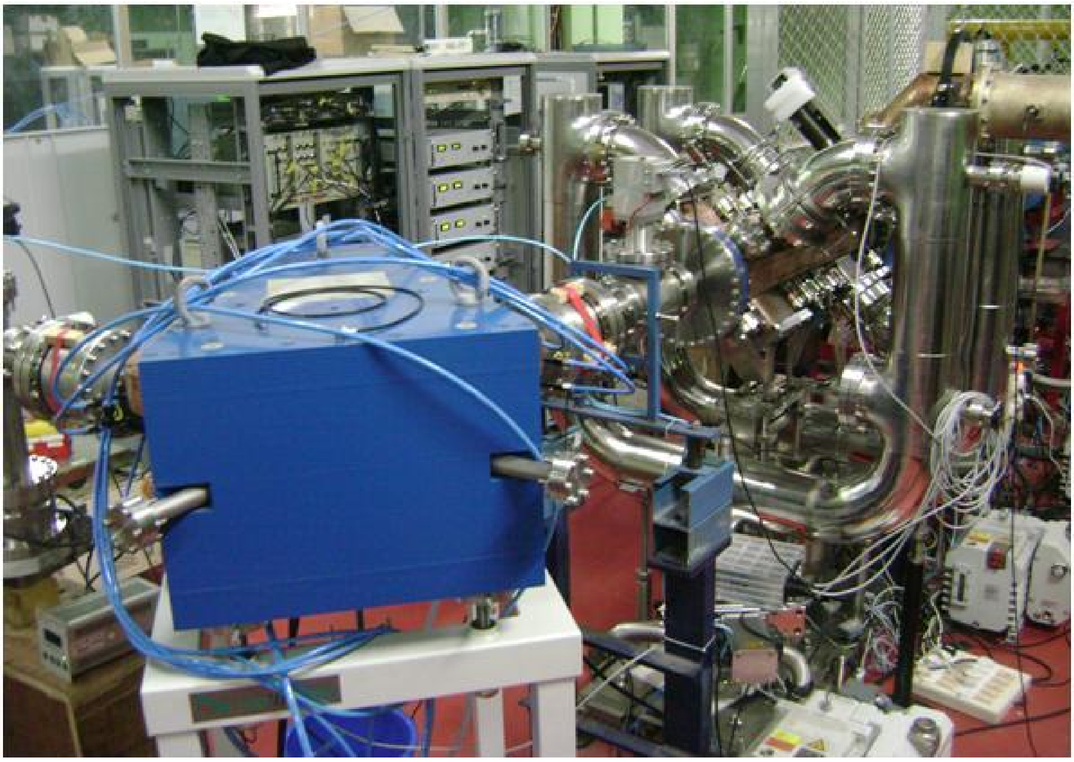

Figure 0.3: 200 keV RFQ Beam line

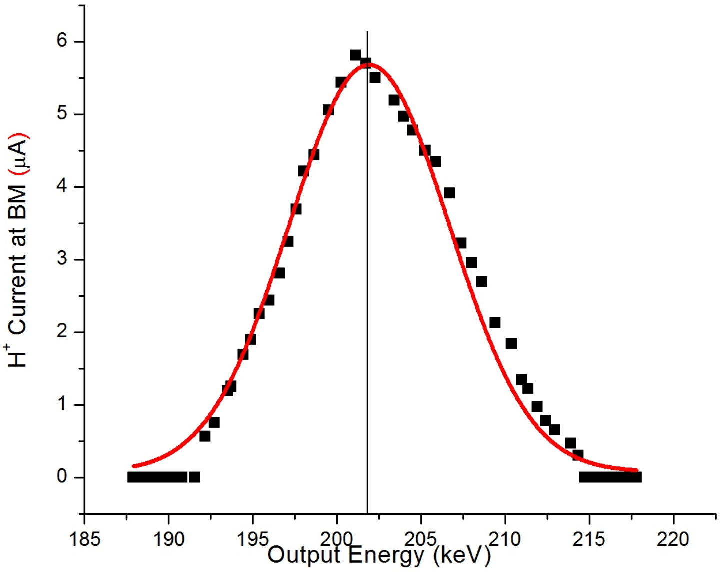

Figure 0.4: Energy and energy spread of the output beam

As part of our on going project LEHIPA [13] for development of 20 MeV, 30 mA proton linac, the design studies of the 3 MeV RFQ were also done. In chapter 6, we present some of the simulations studies of the 3 MeV proton RFQ. The length of this 3 MeV RFQ is ~4 m. For long RFQ structures the frequencies of the higher order modes will come closer to the desired quadrupole mode. So with a mechanical perturbations, the contribution of the higher order modes in the field distribution will increase as the difference between the modes decreases. This makes the structure sensitive to the perturbations. It is therefore planned to make this RFQ in 4 sections of 1 m each. 2 sections are mechanically joined to make a two 2 m long segments and these segments are coupled via a coupling cell [14]. The gap between the vanes of the two segments are adjusted in such a way that the superior and inferior mode frequencies will lie above and below the desired mode frequency. This will make the structure insensitive to the mechanical perturbations. The parameters of these coupling cells have been optimized using the computer code CST Microwave studio.The effect of these coupling cells on the beam dynamics have been studied. It was observed that the more number of coupling gaps will deteriorate the beam quality as well as transmission. From the beam dynamics point of view, it is advisable to have minimum number of coupling gaps. Based on these we have decided to have only one coupling cell in 3 MeV proton RFQ.

Summary, conclusions and the scope for the future developments are presented in chapter 7.

References:

1. I M Kapchiskiy and V A Tepliakov, Prib. Tekh. Eksp. 2,19 (1970).

2. H Nifenecker, O Maplan and S David, Accelerator-driven subcritical reactors, Institute of Physics, Series in fundamental and applied nuclear physics, June 1, 2003.

3. National Spallation Neutron Source, NSNS/CDR-2/VI, May 1997.

4. J Vervier (GANIL): EURISOL, Preliminary design study of the next-generation European ISOL radioactive nuclear beam facility, Contract Number HPRI-1999-

CT-50001.

5. Conceptual design Report of 400 keV D^+RFQ for PURNIMA Sub-Critical Facility, Shweta Roy, T Basak, Rajni pande, S V L S Rao, M Aslam, P Jain, P Singh, P K Nema, S Kailas and V C Sahni, BARC/2005/I/005.

6. P Singh, Status of the LEHIPA Project at BARC, INPAC-2006, p. 50.

7. K R Crandall, R H Stokes and T P Wangler, RF Quadrupole beam dynamics design studies, Proceedings of 1979 Linear Accelerator Conference (Brookhaven National Laboratory, Upton, NY, 1980), BNL-51134, P. 205; LANL Manual of RFQ design codes (Los Alamos National Laboratory Report LA-UR-96-1836 (revised February 12, 1997).

8. S V L S Rao and P Singh, Design studies of a high current radiofrequency quadrupole for accelerator-driven systems programme, PRAMANA-Journal of Physics, Vol.74, No. 2, February 2010, pp. 247-259.

9. W D Kilpatrick, A criterion for vacuum sparking design both RF and Dc, Radiation Lab Report URCL-2321 (1953).

10. LIDOS, A Computer Code for Beam Dynamics of RFQ Linac, Version 1.1.

11. J H Billen and L M Young, Poisson, Superfish, LA-UR-96-1834, LANL.

12. T P Wangler, Principles of RF Linear Accelerators (Wiley, New York, 1998)

13. P Singh et al, Accelerator development in India for ADS programme, Pramana-J. Phys. 68, 331 (2007).

14. J Browman et al, Couple RFQs as compensated structures, Linac90, Albuquerque, p. 70

Chapter 1

Introduction

The particle accelerator delivers the energy to charged particle beams by application of an electric field. The first particle accelerators were electrostatic (DC) accelerators in which the particle acquires an energy equal to the product of its electric charge times the potential drop. The accelerators using DC field for acceleration of charged particles are Cockroft-Waltor [1], Van de Graaff [2] and Tandem accelerators [3]. The main limitation of DC accelerators is that the maximum energy obtainable cannot exceed the product of charge times the potential difference that can be maintained, and in practice this potential difference is limited by electric breakdown to not more than few tens of megavolts. RF accelerators bypass this limitation by applying a harmonic time-varying electric field to the beam, which is localized into bunches, such that the bunches always arrive when the field has the correct polarity for acceleration. The time variation of the field removes the restriction that the energy gain be limited by a fixed potential drop. The beam is accelerated through a structure in which a particular electromagnetic mode is excited from a high-frequency external power source. For acceleration, the beam particles must be properly phased with respect to the fields, and for sustained energy gain they must maintain synchronism with those fields, this requirement has led to the name resonance accelerators, which include the Linear accelerators [4-7] (linacs), cyclotron [8] and synchrotron. The ideal particle orbit in an RF accelerator is a straight line for a linac, a spiral for a cyclotron and a circle for a synchrotron. In cyclic accelerators (cyclotrons and synchrontrons), the magnets are used to confine the beam in closed orbits and radio frequency cavities are used for imparting energy to the beam. Initially, these particle accelerators are developed as tools for nuclear and particle physics research. The vast amount of applied research did grow from these technologies. More recently there is an active, ongoing work to utilize the high current, high energy particle accelerators for nuclear power generation and transmutation of nuclear waste.

In these high current applications, the linear accelerator have more advantages than the cyclic accelerators because of their capability of producing high-energy, high-intensity charged particle beams of small diameter and small energy spread. Since the beam traverses the structure in a single pass therefore repetitive error conditions causing destructive beam resonance are avoided. Also, there is no power loss from synchrotron radiation, which is the limitation, particularly for high energy beams in circular accelerators. Besides, injection and extraction are simpler than in circular accelerators, since the natural orbit of the linac is open at each end, so special techniques for beam injection and extraction are not needed. The linac can operate at any duty factor, which results in acceleration of beams with high average current. So the linacs have therefore become the obvious choice for all the high current advanced applications such as Accelerator Driven systems (ADS) [9] for effective utilization of thorium resources, Spallation Neutron Sources (SNS) [10] and production of Radioactive Ion Beams (RIB) [11].

In RF accelerators the beam must be longitudinally bunched so that all particles will be accelerated. In a conventional accelerator such as the drift tube linac (DTL), bunching is accomplished prior to injection into the Linac using one or more RF bunching cavities. In buncher cavities RF electric fields are applied to the DC input beam to produce a velocity modulation in which early particles are decelerated and late particles are accelerated. After a suitable drift space, the beam becomes bunched, ready for injection into the Linac. The bunching is usually not very efficient, especially for high-current beams because of the high space-charge forces at low energies, since the forces on the particle are proportional to $(1-\beta^2)$, where $\beta = \frac{v}{c}$ is the velocity. In high-intensity beams, the bunching process causes an increase in the beam density, which increases the space-charge forces further which results in the blow-up of the transverse beam emittance. The conventional DTL linacs are efficient only in the velocity range of $0.04 \leq \beta \leq 0.28$. In order to make the efficient use of DTL strcutures in older Linacs, the extraction voltage of the ion source was increased to $\sim 0.7\,MV$. These high voltages were generated using the Cockroft Walton Generators. The fundamental limitations of the conventional linacs is not only in terms of beam current, but also the reliable operation of HV columns, which is responsible for the large fraction of machine downtime. However, the RFQ accelerator, proposed by Kapchinskii [12] and Tepliakov in 1970, is well suited for acceleration of beams with low velocities in the range of about 0.01 to 0.1 times the speed of light.

The RFQ uses the velocity independent transverse electric focusing at low energies which gives a significant strong focusing as compared to conventional linacs that use velocity dependent magnetic lenses. This allows one to extend the practical range of operation of RFQs to low velocities, thus eliminating the need for large, high voltage dc accelerators. The RFQs bunch the beam adiabatically and by proper choice of parameters one can achieve a high transmission ($> 90\%$). Becasue of their remarkable capability of simultaneous focussing, bunching and accelerating the low-energy ion beams with high beam quality, the RFQs are well suited as a first unit of all high current RF linear accelerators. In view of the importance of RFQ accelerators for high-current machines, the R&D activities for the design and development of 2 different continuous wave (CW) RFQs were initiated at BARC, Mumbai.

1. A 400 keV Deuteron RFQ [13] for neutron production

2. A 3 MeV, 30 mA proton RFQ for Low Energy High Intensity Proton Accelerator (LEHIPA) [14], which will be used as a front-end injector to 1 GeV Linac for ADS application.

1.1 Deuteron RFQ:

A 14 MeV neutron generator based on the T(d,n) reaction using a 400 keV DC accelerator is operational at PURNIMA lab, BARC (Figure 1.1).The 14 MeV neutrons are produced when deuteron (D^+) ion beam accelerated up to 400 keV is bombarded on thick Tritium (${}_1H^3$) target.

$$ {}_1H^3 +_1 H^2 \rightarrow_2 He^4 +_0 n^1 + 17.6\, MeV $$

The angular distribution of 14 MeV neutrons is slightly forward peak in the lab system. The D^+ ion beam is obtained using a RF ion source. The RF ion source was able to produce ion current up to $300 - 400\, \mu A$ out of which only $\sim\, 100 - 200\, \mu A$ could be accelerated up to 400 keV. This beam current when bombarded on a tritium target can produce a neutron flux of $\sim\, 10^9\, {}^n\!/\!_s$.

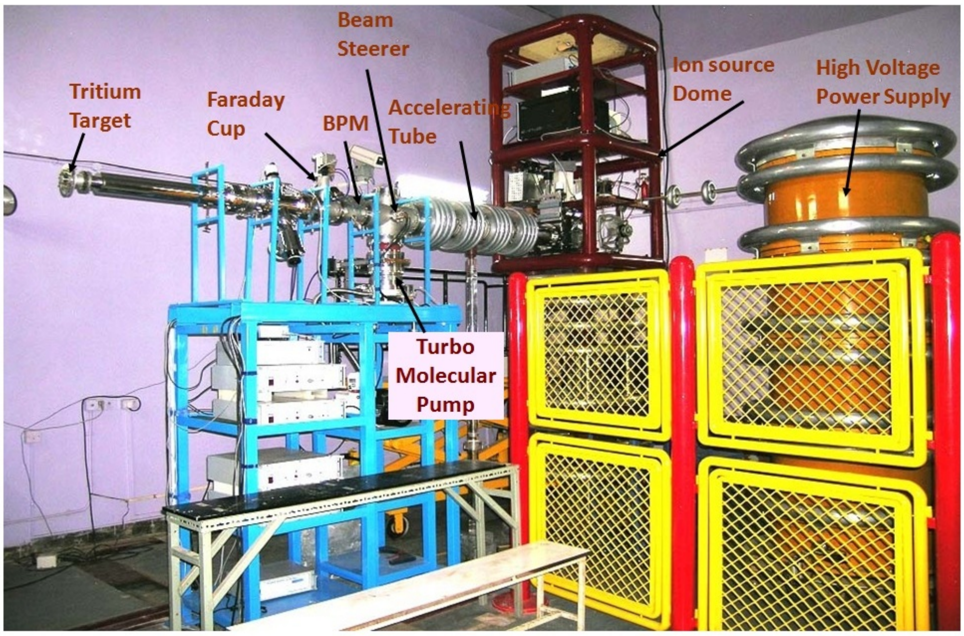

Figure 1.1: 400 keV DC Accelerator at PURNIMA, BARC

In order to increase the flux by an order of magnitude, it was felt that it would be useful to modify the ion source to get a beam current of 1 mA and to replace the DC accelerator with an RFQ.As the beam transmission through the RFQ is more than 90 %, this will increase the neutron flux to $\sim 10^{10}\, n/s$ (Figure 1.2), which will enable experiments to be conducted with greater accuracy.

In addition to this, it will also generate useful experience, at an intermediate level of energy and RF power, in operating such systems. This experience will be of great value towards the objective of building and operating a 20 MeV, 30 mA proton linac (LEHIPA) which will serve as a front-end injector of 1 GeV accelerator for ADS.

This 400 keV RFQ based system consists mainly of a 50 keV ion source, and a 400 keV RFQ. The DC beam from the ion-source is matched to the RFQ using a Low Energy Beam Transport (LEBT) system, which has been designed with two solenoids. The schematic layout of the 400 keV RFQ based accelerator system is shown in Figure 1.3.

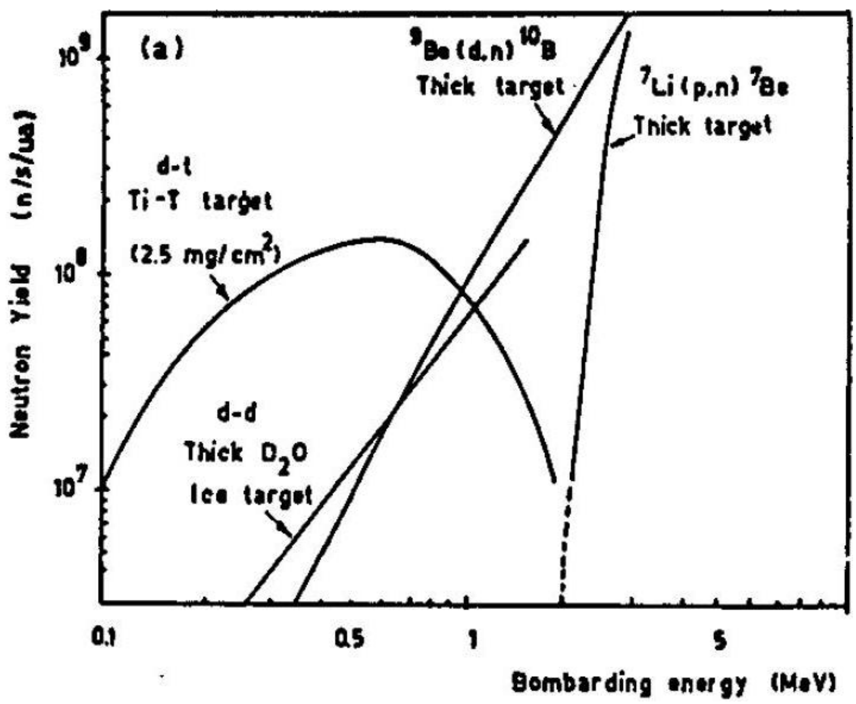

Figure 1.2: Neutron Yield vs deuteron energy [15]

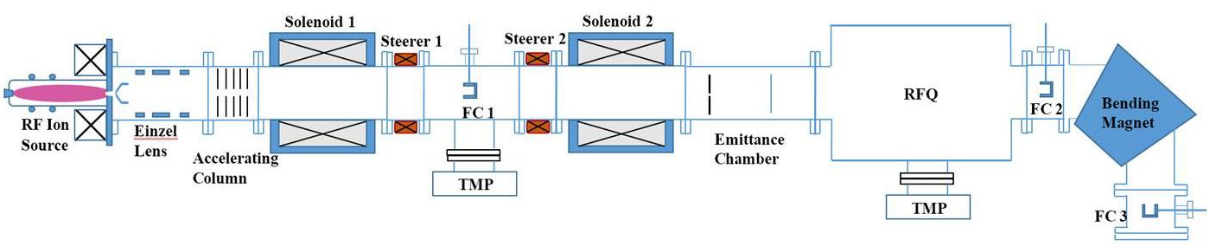

Figure 1.3: Layout of 400 keV RFQ based accelerator system

1.2 Proton RFQ for LEHIPA

Accelerator driven sub-critical reactor systems (ADS) have evoked considerable interest in the nuclear community of the world over because of their capability to incinerate the MA (Minor actinides) and LLFP (long-lived fission products) radiotoxic waste and for converting a fertile material (throium) into fissile nuclear fuel. Since india has vast resources of thorium, ADS offers a potential route for accelerated thorium utilization [16].

ADS mainly consists of a sub-critical reactor coupled to a high power proton accelerator through spallation target as outline in the Figure 1.4. The practical realization of ADS requires development of a high energy ($\sim 1\,GeV$) and high current ($> 20\,mA$) proton accelerator to produce the intense spallation neutron source needed to drive the sub-critical reactor assembly. Also, it is necessary that the accelerator is reliable, rugged and stable in order to provide uninterrupted beam power to the spallation target, over long periods of time. It should also have a high efficiency for conversion of electric power to beam power. The beam loss in the accelerator must be less than 1 W/m so that hands-on maintenance of the accelerator sub-assemblies can be safely done. For ADS, operation of accelerator should be in CW mode to avoid undesirable thermal shocks to the spallation target and fuel elements.

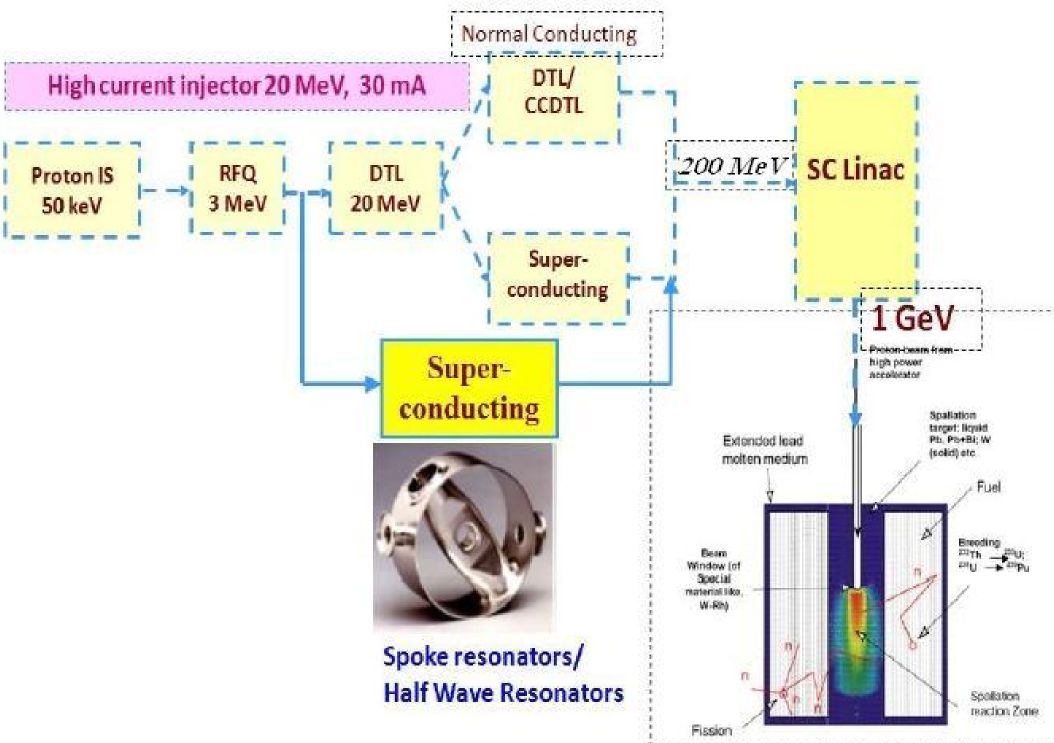

Figure 1.4: Schematic of ADS

In high current proton accelerators, the dominance of space charge effect at low energies causes beam loss and also initiates oscillatory particle motions that appear later as a beam halo in the high-energy sections. The beam halo is the dominant particle loss mechanism and is closely connected to the emittance mismatch in the low energy sections of the accelerating structure, resulting in severe activation of components in the Linac. For these reasons, it is very important for beam to smoothly move across segments in the low-energy injector sections. It is envisioned that the 1 GeV accelerator for ADS be pursued in three phases, namely 20 MeV, 200 MeV and 1 GeV. The most challenging part of this CW proton accelerator is development of the low-energy injector, typically up to 20 MeV, because the space charge effects are maximal at low energies. Therefore, the development of a 20 MeV, 30 mA proton accelerator (LEHIPA) as the front-end injector of the 1 GeV accelerator for the ADS programme has been initiated at BARC.

The major components of LEHIPA are a 50 keV ECR ion source, a 3 MeV RFQ and a 20 MeV drift tube linac (DTL). The LEBT and MEBT (Medium energy beam transport) lines will match the beam from the ion source to RFQ and from RFQ to DTL respectively. The main criterion for the design of the Linac is to have minimum beam loss and maximum acceleration efficiency. The layout of the 20 MeV accelerator is shown in Figure 1.5.

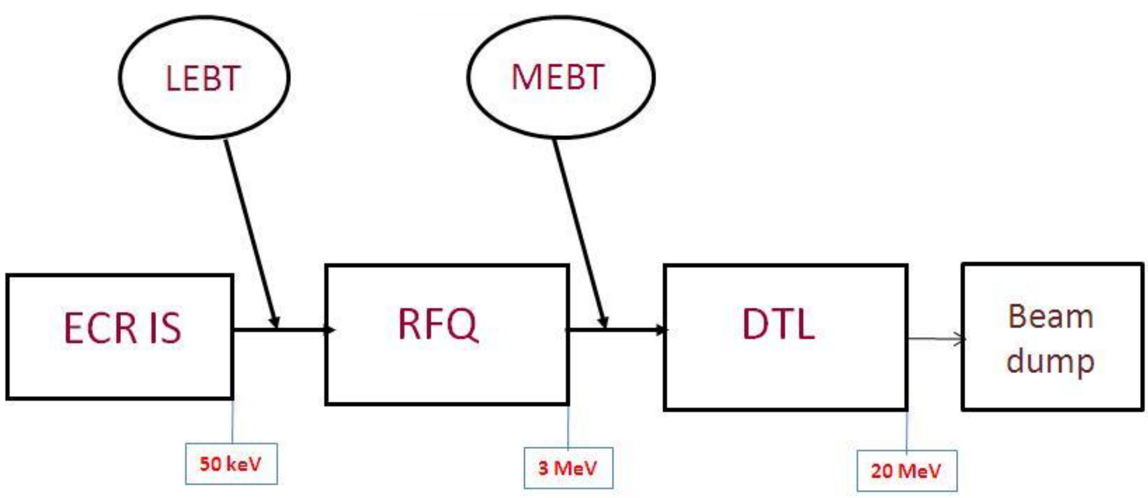

Figure 1.5: Layout of LEHIPA

1.3 List of RFQs

Here, we present the list of existing and status of the proposed H^+/D^+ RFQs.

Table 1.1: List of RFQs

Project	Country	Ions	type	Freqeuncy (MHz)	Peak current (mA)	duty cycle	status
LEHIPA	*India*	H^+	*4-vane*	*352.2*	*30*	*100 %*	*fabrication stage*
LEDA	*US*	H^+	*4-Vane*	*350*	*110*	*100 %*	*demonstrated*
Trasco	*Italy*	H^+	*4-Vane*	*352.2*	*30*	*100 %*	*Fabrication completed*
IPHI	*France*	H^+	*4-Vane*	*352.2*	*100*	*100 %*	*RF Testing*
PXIE	*US*	H^-	*4-Vane*	*162.5*	*1-10*	*100 %*	*under construction*
IFMIF	*Italy*	D^+	*4-vane*	*175*	*140*	*100 %*	*design stage*
Franz	*Germany*	H^+	*4-rod*	*175*	*200*	*100 %*	*testing stage*
SARAF	*Israel*	D^+	*4-rod*	*176*	*4*	*100 %*	*operated*
C-ADS	*China*	H^+	*4-vane*	*162.5*	*15*	*100 %*	*design stage*
PEFP	*korea*	H^+	*4-vane*	*350*	*20*	*24 %*	*Commissioned and working*
JAERI-BTA	*Japan*	H^+	*4-vane*	*201.5*	*110*	*10 %*	*operated*
SNS	*US*	H^-	*4-vane*	*402.5*	*56*	*6.2 %*	*Commissioned and working*
LINAC 4	*Swiss*	H^-	*4-vane*	*352.2*	*70*	*6 %*	*Commissioned*
J-parc	*Japan*	H^-	*4-vane*	*324*	*50*	*3 %*	*RF Testing*

I-SNS	*India*	H^-	*4-vane*	*352.2*	*30*	*1.25 %*	*design stage*
RFQ2	*Swiss*	H^+	*4-vane*	*202.5*	*200*	*0.03 %*	*operated*
ATS	*US*	H^-	*4-vane*	*350*	*100*	*0.025 %*	*operated*

Here in this thesis, we present the design and development of 400 keV RFQ. The theses is organized in seven chapters.

In Chapter 2, basic theory of RFQ, and beam simulations results are given. In chapter 3, complete 2D and 3D RFQ cavity design is discussed. In chapter 4, the perturbative analysis of the 4-vane RFQ and tuning algorithm are discussed. In chapter 5, the RF characterization, low power conditioning and beam commissioning results were presented. In chapter 6, the simulations results of LEHIPA RFQ are given. In chapter 7, summary and scope for future work are presented.

Chapter 2

RFQ Beam Dynamics and Simulation results

2.1 Introduction

The radiofrequency quadrupole (RFQ) is relatively a new type of linear accelerator, and its recent development was a major innovation in the linac field. Although the operating principle is basically simple, the RFQ was unknown until the late sixties. The major contributions were made to RFQ design by the Los Alamos National Laboratory (LANL), where a demonstrator named POP (proof of principle) was built and run in 1980. Since then, RFQ has become so popular that, within a few years, several RFQs were built and commissioned in numerous laboratories and universities throughout the world.

In this chapter, we present the principle of RFQ operation including the field description that describe the beam dynamics. This is followed by a discussion of the design strategy, which we have adopted for our 400 keV RFQ and give the results of the simulation studies.

2.2 Principle of RFQ

In RFQ the electric field distribution is generated by four vanes arranged symmetrically around the beam axis, as seen schematically in Figure 2.1. The vanes are excited with RF power so that at any given time, adjacent vane tips have equal voltages of opposite sign. If the vane tips are at a constant radius along the beam axis, designated the z-axis, then only a transverse quadrupole field is present. This electric field is focusing in each plane during half of the RF period and defocusing during the other half, giving the structure the properties of an alternating-gradient focusing system with a strength independent of the particle velocity. Because the geometry of the electrodes described above does not introduce any longitudinal field component, so this setup cannot be used to form bunches and for acceleration.

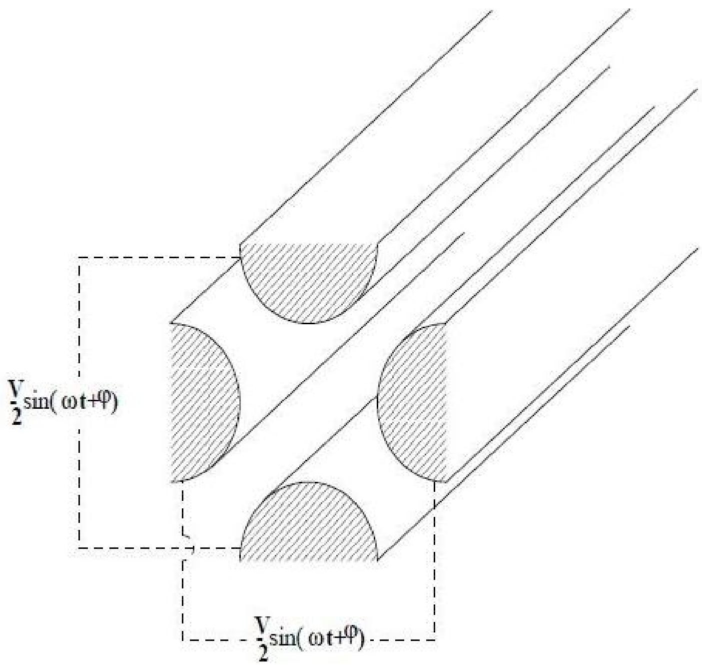

Figure 2.1: Four vanes of Quadrupole with alternating polarity

In order to generate a longitudinal accelerating field, the quadrupole symmetry of the electrodes needs to be distrubed. Which is as shown in Figure 2.2. When the vertical electrode has a distance $'a'$ from the beam axis, the horizontal electrode has a distance of $'m * a'$ from the axis, where $'a'$ is known as the aperture and $'m'$ is the modulation, which is typically varied between 1 to 3. After a certain distance c_l, the perturbation has changed, so that vertical electrode has a distance of $'m * a'$ and the horizontal electrode was at a distance of $'a'$ from the beam axis. If the distance c_l is synchronized with the RF field and the particle's velocity as $c_l = \frac{\beta\lambda}{2}$, where $\beta = \frac{v}{c}$ and λ is wavelength of the RF, then the particle sees a net accelerating field in every cell. This is the key idea of RFQ principle.

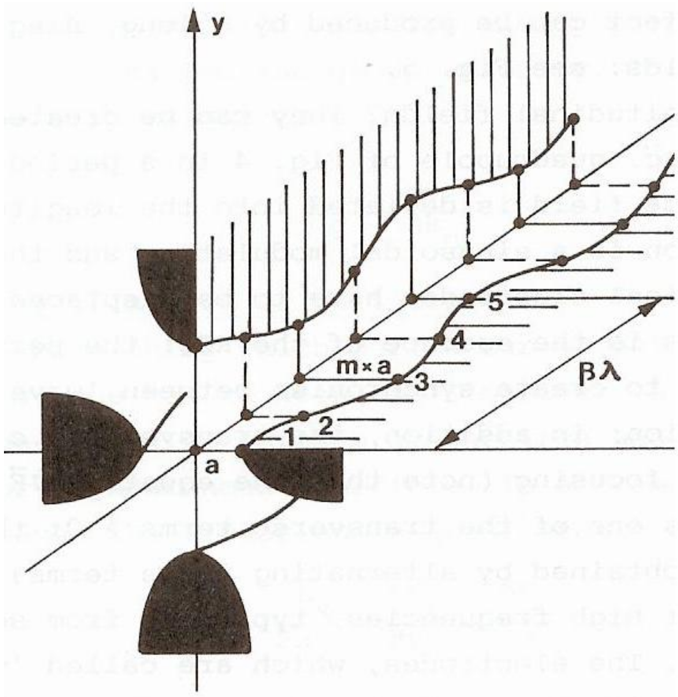

Figure 2.2: Quadrupole with modulated vanes

The variation of parameters of the RFQ (ie., modulation, synchronous phase and aperture) are chosen carefully in order to keep the beam well focussed and accelerate with maximum transmission.

2.2.1 Field description

The time varying electric field (E) in terms of the scalar and vector potentials $\left(\phi, \vec{A}\right)$ is given as

$$\vec{E} = -\vec{\nabla}\phi - \frac{\partial \vec{A}}{\partial t} \tag{2.1}$$

In all types of RFQ structures, the magnetic fields near to the vane tips is zero. Only the electric fields are present near the tips. This concides with the fact that the area near the beam axis refers to capacitive component of the RF-structure. Therefore, the variation of vector potential can be neglected in the above equation 2.1, so the electric field is purely a function of scalar potential (ϕ), which is equivalent to static case. This is called a quasi-static approximation. So in order to find the field in the region near to beam axis, the Laplace equation has to be solved taking the boundary conditions into account.

The Laplace equation in cylindrical coordinates is given by

$$\frac{\partial^2\phi}{\partial r^2} + \frac{1}{r}\frac{\partial\phi}{\partial r} + \frac{1}{r^2}\frac{\partial^2\phi}{\partial\theta^2} + \frac{\partial^2\phi}{\partial z^2} = 0 \tag{2.2}$$

Using the variable seperables method for solving the above equation assuming

$$\phi(r,\theta,z,t) = R(r)\Theta(\theta)Z(z)\,sin(\omega t + \varphi) \tag{2.3}$$

The solution of the laplace equation can be written as

$$\phi(r,\theta,z) = \sum_{s=0}^{\infty} A_s r^{2(2s+1)} cos(2(2s+1)\theta) + \sum_{n=1}^{\infty}\sum_{s=0}^{\infty} A_{ns} I_{2s}(knr) cos(2s\theta) sin(knz) \tag{2.4}$$

The above equation 2.4 is the general K-T potential function, from which the electric field in the vicinity of the beam may be calculated.

2.2.1.1 Two-Term potential function

By looking at general K-T potential function, the RFQ look like a complicated three dimensional structure, for which a simple analytical form for the fields would be difficult to obtain. The analytical solution gives the dependence of the fields on the vane shape, and which in turn greatly simplify our task of choosing the optimized electrode geomtries. One way to obtain a self-consistent solution is to select only the lowest-order terms from the general solution for the potential, and then construct the electrode shapes that conform to the resulting equipotential surfaces. This is the approach that was used by K-T [12] in their original paper. By considering only the first two terms from the equation 2.4, the potential function is written as

$$\phi(r,\theta,z) = A_0 r^2 cos(2\theta) + A_{10} I_0(kr) cos(kz) \tag{2.5}$$

Where A_0 and A_{10} are constants that are determined by the electrode geometry, and $k = {}^{2\pi}/_{L}$, where L is the period of the electrode modulation. We choose $L = \beta_s\lambda$, where

β_s is the velocity of the synchronous particle. The constants A_0 and A_{10} are determined by assuming the potential at a particular time on the horizontal and vertical vanes as $+V_0/2$ and $-V_0/2$, respectively and also assuming that the vertical vane displacement as $r = m * a$, and horizontal vane displacement as $r = a$, at $z = 0$. Then, the constants are given by

$$A_0 = \frac{V_0}{2a^2} \frac{I_0(ka) + I_0(kma)}{m^2 I_0(ka) + I_0(mka)} \tag{2.6}$$

and

$$A_{10} = \frac{V_0}{2} \frac{m^2 - 1}{m^2 I_0(ka) + I_0(mka)} \tag{2.7}$$

Then the complete time-dependent potential is given as

$$\phi(r,\theta,z,t) = \frac{V_0}{2}\left[\chi\left[\frac{r}{a}\right]^2 cos(2\theta) + AI_0(kr)cos(kz)\right] sin(\omega t + \varphi_0) \tag{2.8}$$

where $\chi = \frac{I_0(ka)+I_0(kma)}{m^2 I_0(ka)+I_0(mka)}$ and $A = \frac{m^2-1}{m^2 I_0(ka)+I_0(mka)}$. The potential function in cartesian coordinates is given as

$$\phi(x,y,z,t) = \frac{V_0}{2}\left[\frac{\chi}{a^2}\left[x^2 - y^2\right] + AI_0(kr)cos(kz)\right] sin(\omega t + \varphi_0) \tag{2.9}$$

In principle, the geometry of the electrodes is now specified from the $\pm V_0/2$ equipotential surfaces. The transverse cross sections are approximately hyperbolas. At $z = \beta\lambda/4$, the RFQ has exact quadrupole symmetry, and the tips of the x and y electrodes have a radius equal to $r_0 = a\chi^{-1/2}$. The machining of the electrodes following the exact analytical shape is very difficult due to high peak fields which will lead to sparking and therefore prohibit the reliable operation. So the real shape of the electrodes has to be deviated from the ideal shape to control the peak surface fields, and to ease the machining.

The peak surface field is important, because the probability of electric breakdown increases with increasing surface field. For circular transverse-electrode geometry with no longitudinal modulations, the peak surface electric field does not occur at the electrode tip, but at the point where the electrodes have minimum separation. The field at the vane tip is V_0/r_0 and the peak field is $E_s = \alpha V_0/r_0$, where $\alpha = 1.36$. For modulated poles, the value of α is slightly modified and also depend on the transverse and logitudinal radii of curvature. The spatial dependence of the potential function within a cell is completely determined by 3 parameters χ, $A\, and\, k$, which vary from cell to cell along the RFQ, and must be chosen to provide the desired RFQ performance.

The behavior of particles in the RFQ is determined by the electric field components. The electric field may be obtained from the gradient of the potential function. By differentiating equation 2.9, the components in cartesian coordinates are

$$E_x = -\frac{\chi V_0}{a^2}x - \frac{kAV_0}{2}I_1(kr)\frac{x}{r}cos(kz) \tag{2.10}$$

$$E_y = \frac{\chi V_0}{a^2}y - \frac{kAV_0}{2}I_1(kr)\frac{y}{r}cos(kz) \tag{2.11}$$

$$E_z = \frac{kAV_0}{2}I_0(kr)sin(kz) \tag{2.12}$$

Where time variation of each component is given by $sin(\omega t + \varphi_0)$. The first term in the equations 2.10 & 2.11 describes the quadrupole focusing whose strength depends on the term $\frac{V_0\chi}{a^2}$, and the second term corresponds to the RF defocusing, which occurs when the vanes are modulated. As the modulation increases (i.e., A increase) along the RFQ, the defocusing term increases and the quadrupole strength ($\propto \chi$) decreases since

$$\chi = 1 - AI_0(ka) \tag{2.13}$$

As a result, the modulation has an upper limit, beyond which the Quadrupole focusing strength is less than the RF defocusing strength. To accelerate the ions to higher energies the modulation can be held constant at some practical value. With increasing energy the velocity of the particles increases and therfore the cells get longer and achieving the longitudinal field becomes inefficient leading to high RF power consumption. Therefore an RFQ structure is not suitable for accelerating the particles to very high beam energies.

2.2.1.2 Transverse dynamics

The equation of motion of particles in the RFQ fields are given by

$$\ddot{x} + \frac{q}{m}\left(\frac{\chi V_0}{a^2} + \frac{kAV_0}{2r}I_1(kr)cos(kz)\right)xsin(\omega t + \varphi_0) = 0 \tag{2.14}$$

$$\ddot{y} + \frac{q}{m}\left(-\frac{\chi V_0}{a^2} + \frac{kAV_0}{2r}I_1(kr)cos(kz)\right)ysin(\omega t + \varphi_0) = 0 \tag{2.15}$$

By approximating the modified bessel functions $I_0(kr) \approx 1$ and $I_1(kr) \approx {}^{kr}/_2$, then one obtains the transverse equation of motion to be

$$\ddot{x} + \frac{q}{m}\left(\frac{\chi V_0}{a^2} + \frac{k^2AV_0}{4}cos(kz)\right)xsin(\omega t + \varphi_0) = 0 \tag{2.16}$$

The time dependence of the axial position of a particle is given by $kz = \omega t$, the second term in brackets is proportional to $cos(\omega t)sin(\omega t + \varphi_0) = [sin(\varphi_0) + sin(2\omega t + \varphi_0)]/2$, so the above equation becomes

$$\ddot{x} + \frac{q}{m}\left(\frac{\chi V_0}{a^2}sin(\omega t + \varphi_0) + \frac{k^2AV_0}{8}[sin(\varphi_0) + sin(2\omega t + \varphi_0)]\right)x = 0 \tag{2.17}$$

Assume a simple trial solution

$$x = C[1 + \epsilon sin(\omega t + \varphi_0)]sin(\Omega t) \tag{2.18}$$

where C is constant, and Ω and ϵ are two new parameters, such that $\Omega \ll \omega$ and $\epsilon \ll 1$. By differentiating the above equation twice, and neglecting the smaller terms of order ${}^{\epsilon\Omega}/_{\omega}$ and ${}^{\Omega^2}/_{\omega^2}$, we get

$$\ddot{x} \cong -C\epsilon\omega^2 sin(\Omega t)sin(\omega t + \varphi_0) \tag{2.19}$$

If we have a time varying RF fields in a quadrupole without modulation, then the second term in equation 2.16 is zero and for that case, we get

$$\epsilon \cong \frac{q\chi V_0}{m\omega^2 a^2} \tag{2.20}$$

Now assuming the same value of the ϵ, we look for the smoothed properties of the motion, by substituting the trial soultion in the equation 2.16, and averaging over an RF period. we get

$$\ddot{\bar{x}} + \frac{q}{m}\left(\frac{\chi V_0 \epsilon}{a^2} + \frac{k^2 A V_0}{8} sin(\varphi_0)\right)\bar{x} = 0 \tag{2.21}$$

This result implies that the trajectory for the average motion is the solution of the simple harmonic oscillator equation and, therefore, that the squared frequency is $\Omega^2 = \frac{1}{2}\left[\frac{q\chi V_0}{m\omega^2 a^2}\right]^2 + \frac{qk^2 V_0 A sin(\varphi_0)}{8m}$. The first term is always positive and represents the contribution of the quadrupole focusing, and the second term represents the RF defocussing term. If the quadrupole term is large compared with the RF defocussing term, the transverse motion becomes decoupled from the longitudinal motion, and the oscillation frequency of the average motion of trajectory is same for all the particles. It is customary to refer to the betatron phase-advance per focusing period, defined as $\sigma_{0t} = {}^{\Omega\lambda}/_{c}$. So the phase advance per focusing period is written as

$$\sigma_{0t}^2 \cong \frac{1}{8\pi^2}\left[\frac{q\chi V_0 \lambda^2}{mc^2 a^2}\right]^2 + \frac{\pi^2 q A V_0 sin(\varphi_0)}{2mc^2\beta^2} \tag{2.22}$$

It is found that the stability criteria depend on σ_{0t}. In the smooth approximation, the beam is stable when $\sigma_{0t}^2 > 0$. When $-{}^{\pi}/_{2} \leq \varphi_0 \leq 0$, which is the condition for simultaneous acceleration and longitudinal focusing, the second term, representing the RF defocusing effect, is negative, which reduces the net focusing. The magnitude of the second term vanishes at the peak of the accelarating waveform, when $\varphi_0 = 0$, and is maximum for $\varphi_0 = -{}^{\pi}/_{2}$. If the second term exceeds the first term, σ_{0t}^2 is negative, and the beam is unstable.

Here we have not considered the space charge forces due to beam. If one consider the space charges forces (assuming a uniform distribution) the phase advance per focusing period is written as

$$\sigma_t^2 \cong \frac{1}{8\pi^2}\left[\frac{q\chi V_0 \lambda^2}{mc^2 a^2}\right]^2 + \frac{\pi^2 q A V_0 sin(\varphi_0)}{2mc^2\beta^2} - \frac{3 Z_0 I \lambda^3 (1-f)}{8\pi m_0 c^2 a^2 b \gamma^3} \tag{2.23}$$

2.2.1.3 Longitudinal dynamics

The RFQ electrode geometry and fields are chosen to produce a specific velocity gain for a synchronous particle that will continuously gain energy along the RFQ. When the synchronous phase is chosen to correspond to the time when the field is increasing, particles that arrive earlier than the synchronous particle experience a smaller field, and those arrive latter experience a larger field. This produces the longitudinal restoring force that provides phase-stable acceleration. The osciallating particles consititute a bunch, and every period in the RFQ contains a single bunch.

If W_s is the energy of the synchronous particle, and W is the energy of the non-synchronous particle, then the average rate of change of the relative energy $W - W_s$ is given by

$$\frac{d(W - W_s)}{dz} = qE_0T(I_0(kr)cos(\varphi) - cos(\varphi_s)) \tag{2.24}$$

Where, $E_0 = \frac{2AV_0}{\beta\lambda}$, $T = \frac{\pi}{4}$, $\varphi$is non-synchronous particle phase and $\varphi_s$is phase of synchronous particle. Similarly the equation that describes the average rate of change of phase difference between an arbitrary particle and the synchronous particle, is

$$\frac{d(\varphi - \varphi_s)}{dz} = -\frac{2\pi(W - W_s)}{m_0c^2\beta_s^3\lambda} \tag{2.25}$$

Now considering the small oscillations, where $cos(\varphi) = cos(\varphi_s) - (\varphi - \varphi_s)sin(\varphi_s)$ and $I_0(kr) \approx 1$. Taking the second derivative of equation 2.25, and substituting $cos(\varphi)$, we get

$$\frac{d^2(\varphi - \varphi_s)}{dz^2} = -\frac{2\pi qE_0T}{m_0c^2\beta_s^3\lambda}(-(\varphi - \varphi_s)sin(\varphi_s)) \tag{2.26}$$

when $-\pi < \varphi_s < 0$, one obtains simple harmonic motion at a longitudinal wave number

$$k_l^2 = \frac{\pi^2 qAV_0 sin(-\varphi_s)}{m_0c^2\beta_s^4\lambda^2} \tag{2.27}$$

So the longitudinal phase advance per focusing period is written as

$$\sigma_{0l}^2 = k_l^2\beta^2\lambda^2 \tag{2.28}$$

$$\sigma_{0l}^2 = \frac{\pi^2 qAV_0 sin(-\varphi_s)}{m_0c^2\beta_s^2} \tag{2.29}$$

This is called zero current phase advance, when we consider the full current (i.e., including space charge forces), the phase advance per focusing period is given as

$$\sigma_l^2 \cong \frac{\pi^2 q A V_0 sin(-\varphi_s)}{m_0 c^2 \beta^2} - \frac{3 Z_0 I \lambda^3 f}{4\pi m_0 c^2 a^2 b \gamma^3} \tag{2.30}$$

2.3 Design Strategy

The beam dynamics of the RFQ [17] Linacs have been extensively studied by LANL and a generalized method was proposed, where RFQ was divided intor four sections, namely, Radial matching section (RMS), Shaper (SH), Gentle Buncher (GB) and Accelerator section (AC). Several other design methods have been proposed [18- 24] for minimizing the emittance growth and the resulting beam losses, out of which we have studied two popular design philosophies [25] and compared their advantages and dis-advantages from the beam dynamics, fabrication and tuning point of view. Based on these studies, we have adopted a conventional design procedure for our 400 keV Deuteron as well as 3 MeV proton RFQs.

2.4 Theory of Generalized method

In a generalized method proposed by LANL, the beam dynamics design of RFQ starts at the end of the gentle buncher (GB). Because at the end of this section a transverse bottleneck will occur. The main parameters are chosen in consideration of the GB, and for this reason we begin from here.

2.4.1 Gentle Buncher section (GB)

The gentle buncher (GB) employes the adiabatic bunching process to bunch the beam efficiently. In this section, the spatial bunch length (Z_b) given by equation 2.31 and the transverse and longitudinal zero current phase advances (σ_{0t}, σ_{0l}) described in sections 2.2.1.2 and 2.2.1.3, are kept constant.

$$Z_b = \frac{\beta\lambda\psi}{2\pi} \tag{2.31}$$

These conditions leads to the constant space charge and external forces while bunching and accelerating the beam. Once the parameters of the RFQ like modulations (m), aperture (a_p), synchronous phase (ϕ_s) and the energy at the end of this section are chosen, the variation of the parameters along the section are generated by solving the equations (2.32-2.34) which result from the above conditions.

$$\beta\psi = const., \tag{2.32}$$

$$\frac{AV sin(\phi_s)}{\beta_s^2} = cons., \tag{2.33}$$

$$\frac{V\chi}{a_p^2} = const., \tag{2.34}$$

where ψ and $\frac{a_p}{\sqrt{\chi}}$ are the phase width of the separatrix and average apreture radius (r_0). The beam bunch usually reaches its minimum phase extent at the end of the GB. If r_0 is held constant, the aperture a_p will decrease as modulation (m) increases along the RFQ. For these reasons, the space charge and acceptance limits typically do not occur for the dc beam at the input but, at the end of the GB section. The design of the GB is done strictly following the need of controlling the transverse dynamics, in particular the acceptance at the end of GB.

2.4.2 Shaper section (SH)

The generation of the parameters based on the equation specified in GB section, will leads to an infinitely long structure. In order to achieve high transmission, without an unacceptably long RFQ, one can introduce an initial bunching section, called SHAPER, with values of modulation (m) and ϕ_s that vary linearly along the RFQ, at the expense of some emittance growth. This procedure results in a two-stage buncher, where the relative lengths of these two sections are chosen to achieve the best balance between beam emittance and transmission requirements.

2.4.3 Accelerator Section (AS)

This section will accelerate the bunched beam up to the final energy having virtually no losses. In this section, the value of A,ϕ_s and the focussing factor B are kept constant all along the length.

2.5 Beam dynamics simulations

Initially, the parameters of the RFQ have been generated using our computer program **'Genp.m'** and then the beam dynamics have been studied using codes LIDOS [26] and cross checked with TOUTATIS [27]. Optimized parameters of RFQ are generated after several iterations. The following criteria are kept in mind while designing the 400 keV RFQ

1. Transmission >90 %
2. Length should be $\sim$ 1 m
3. Peak surface field $<$ 33 $^{MV}/_{m}$

The Main RFQ specifications are given in Table 2.1.

Table 2.1: RFQ Input parameters

Parameters	**Value**	**Units**
Particle	D^+	
Input energy	0.05	MeV
Output energy	0.4	MeV
Transverse Norm RMS emittance	0.015	$\pi\, cm - mrad$
Frequency	350	MHz
Current	1	mA
RF power Consumption	≤ 60	kW (1 tetrode)

2.5.1 RFQ parameter generation

The computer program for the generation of RFQ parameters has been written in MATLAB. This program consists of two programs viz. '**formfac.m**' and '**Genp.m**'. The program '**formfac.m**' is used to choose the parameters at the end of the GB section. Once the parameters at the end of GB are chosen the program '**Genp.m**' will generate the RFQ parameters based on the generalized approach discussed in above section. The computer program **formfac.m** is similar to CURLI program of PARMTEQ package, it calculates the acceptance (Acc), Transverse and Longitudinal current limits (curlT and curlL) based on the simple analytical formulae given by wangler [28]. In order to reduce the transverse losses the acceptance of the RFQ should be more than the beam emittance, so one has to choose the parameters like a_p, m and ϕ_s at the end of the GB section very carefully. The variation of acceptance and current limits as a function of synchronous phase and energy at the end of GB are shown in Figures 2.3 & 2.4.

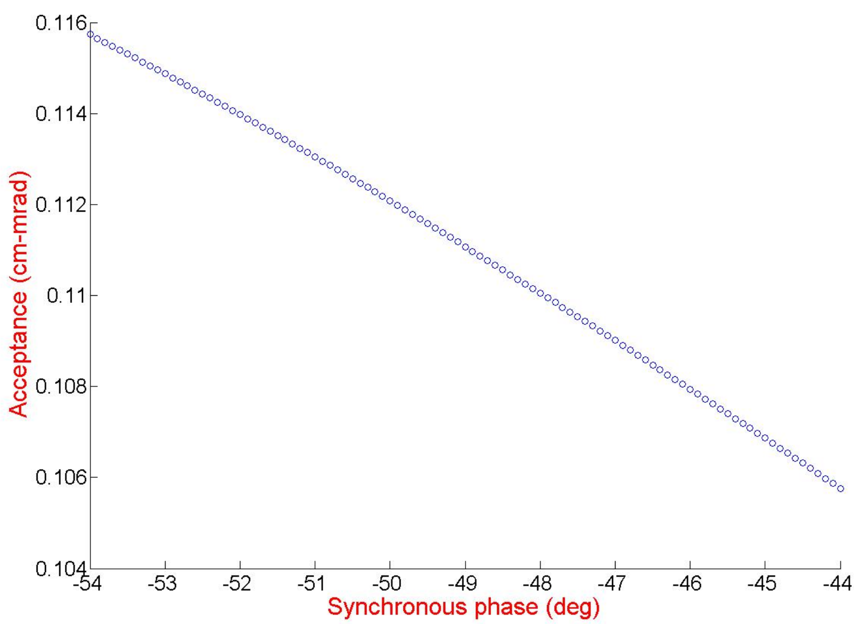

(a) Acceptance

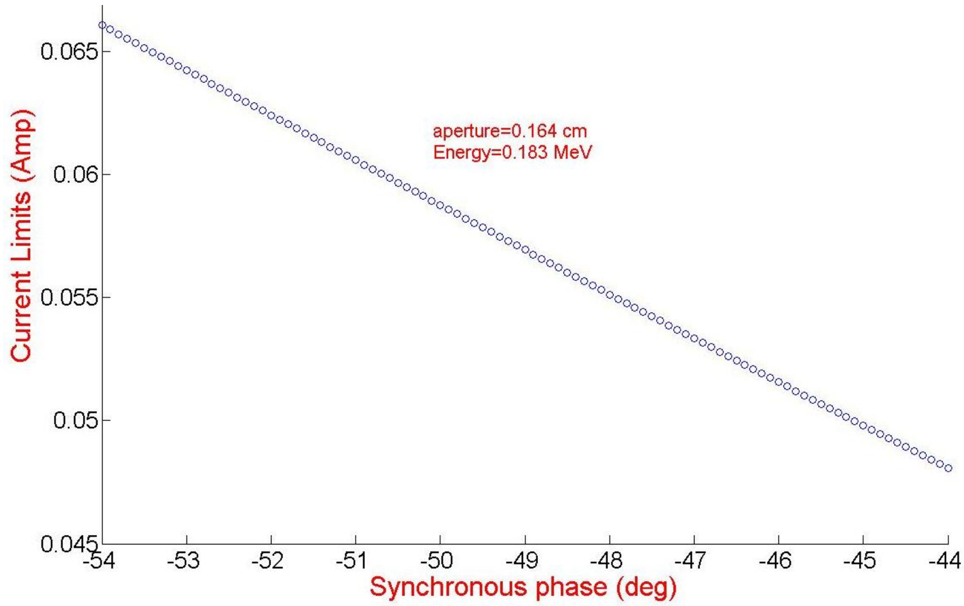

(b) Current Limits

Figure 2.3: Acceptance and Current limits vs Synchronous phase at the end of the GB

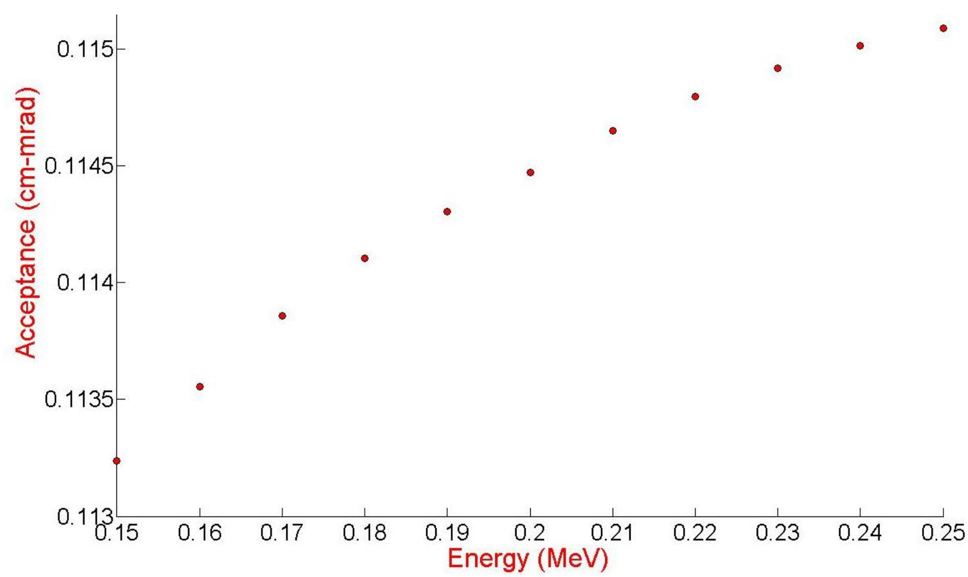

(a) Acceptance

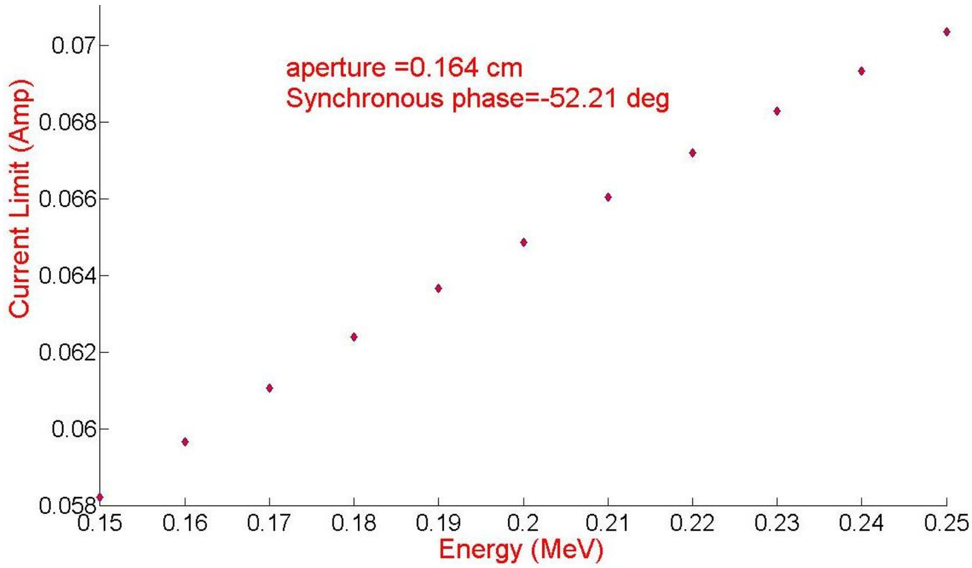

(b) Current Limits

Figure 2.4: Acceptance and Current limits vs Energy at the end of GB

These values are cross checked using the CURLI Program of the PARMTEQ and found to be in good agreement.

2.5.2 Simulation Results

The beam dynamics of the RFQ was done extensively using the computer codes Genp.m, LIDOS [26] and cross checked with TOUTATIS [27]. A large number of Genp.m and LIDOS runs were performed to get the optimized design parameters. The main parameters of the various sections are summarized in Table 2.2. In Figure 2.5, several parameters are plotted as a function of the RFQ length.

Table 2.2: Main parameters of various sections of RFQ

Parameters	At input	After RMS	After SH	After GB	After AS
Energy (MeV)	0.050	0.050	0.115	0.183	0.4
Length (cm)	0.0	2.50	51.7	65.9	100.5
Aperture (mm)	9.575	1.873	1.724	1.640	1.639
Modulation	1.0	1.0	1.1762	1.2847	1.2761
Phase (deg)	0.0	-90	-64.23	-52.21	-43.97
Focusing factor (B)	0.27	4.861	4.861	4.861	4.861
Acceleration efficiency (A)	0.0	0.0	0.102	0.187	0.211
Phase Acceptance	360^0	360^0	356^0	221.7^0	165.8^0

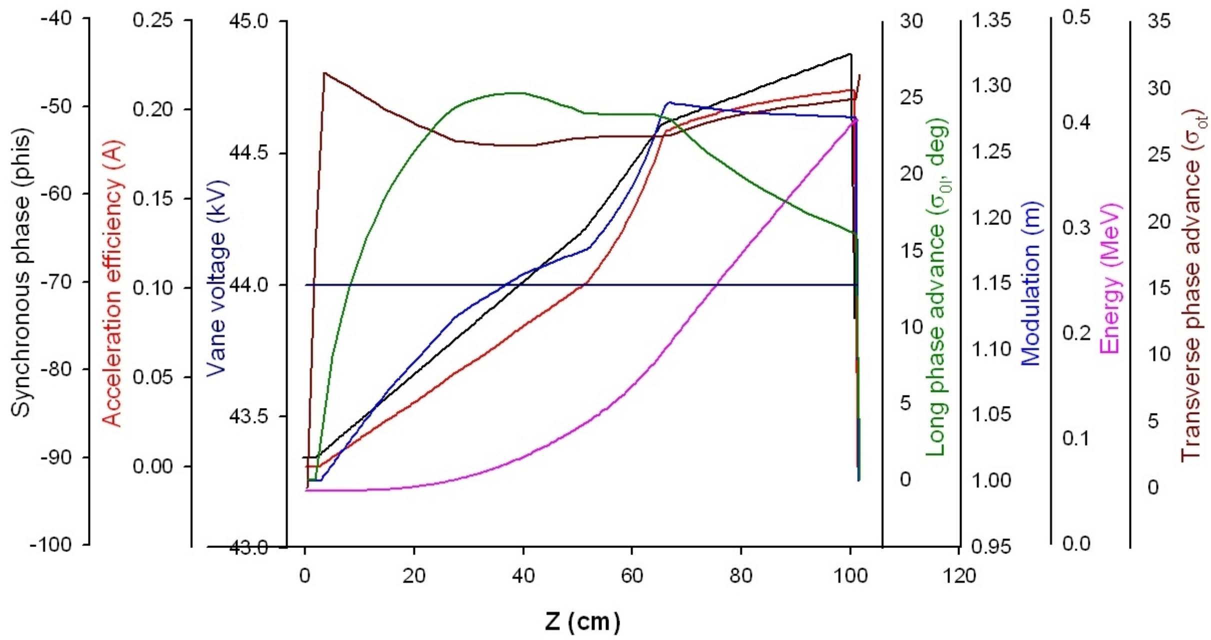

Figure 2.5: Variation of different parameters along the Length of the RFQ

The evolution of the transverse and longitudinal emittance along the length of the RFQ is shown in Figure 2.6.

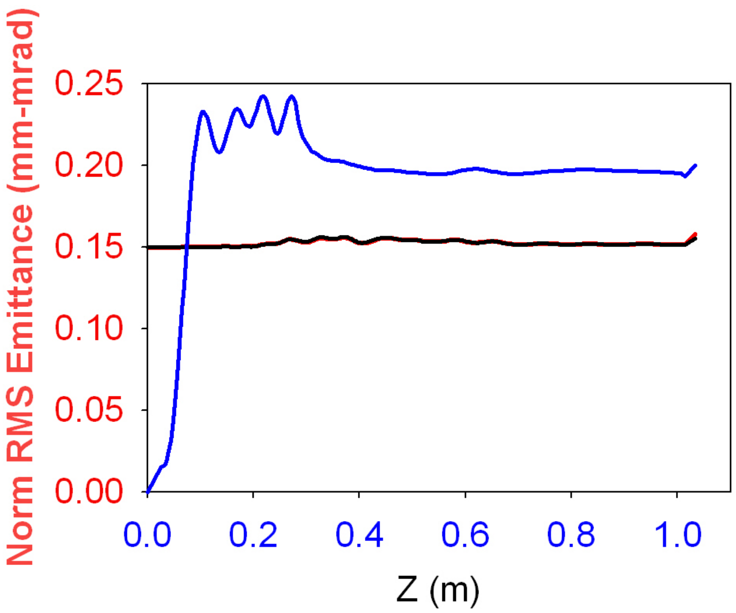

Figure 2.6: Evolution of trasnverse and longitudinal emittances along the RFQ length.

We have studied the effect of input beam distribution on the energy distribution of lost particles and is shown in Figure 2.7. It is clearly seen from the plot that the most of the particles are lost at the end of the GB, where the energy of the beam is ~ 190 keV.

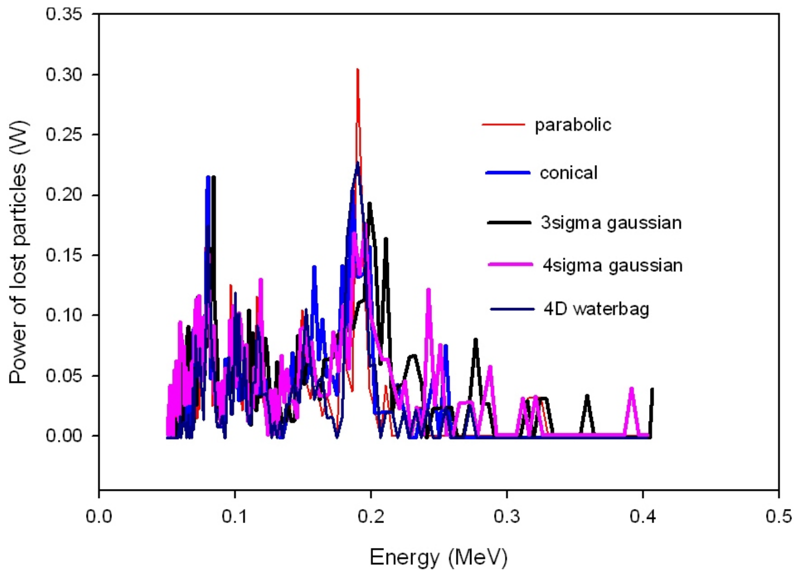

Figure 2.7: Energy distribution of lost particles in RFQ

We studied the transmission as a function of Input beam distribution and the results are shown in Table 2.3.

Table 2.3: Transmission vs input beam distribution

Distribution	Transmission (%)
4D water bag	95
Conical	93
Parabolic	93
3 sigma trun. Gaussian	90
4 sigma trun. Gaussian	89

2.5.3 Error studies and tolerances:

In RFQ design it is crucial to study the effect of beam errors on the beam dynamics. Various effects such as beam misalignment and tilt, variation in the input energy and vane voltage, etc., can degrade the beam dynamics-typically through reduced transmission and increased emittance. Further, it is necessary to study not just the effects of individual errors, but also a combination of errors, which is the more likely scenario. Such a study is essential to get an idea of the errors that can be tolerated, which would in turn place limits on the tolerances that are needed in the fabrication of the RFQ, power supplies, etc. For our study the acceptance criteria was 93 % transmission.

2.5.3.1 Off-axis injection

Figure 2.8 shows the effect of off-axis injection, i.e. if the beam axis and the RFQ axis are misaligned (shifted) with respect to each other. The deuteron beam is still assumed to be coming in parallel to the axis. This misalignment could arise either from an error in the design of the transport line from the ion source to the RFQ, or from a misalignment of the RFQ itself. We can see that in both dimensions the acceptance criterion of 93% transmission is met for misalignments of 0.03 cm or less. This means that the beam-line and the RFQ have to be aligned to better that 300 μm – which is not a very stringent constraint

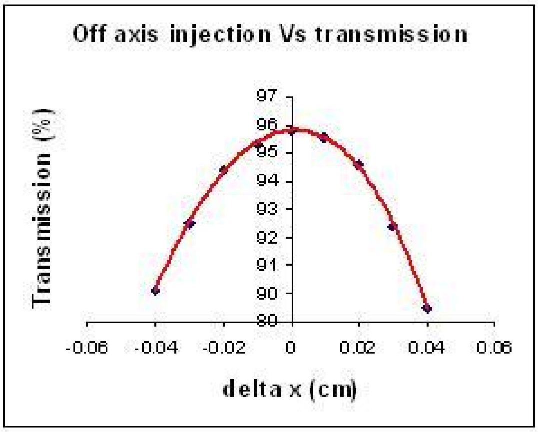

(a) x direction

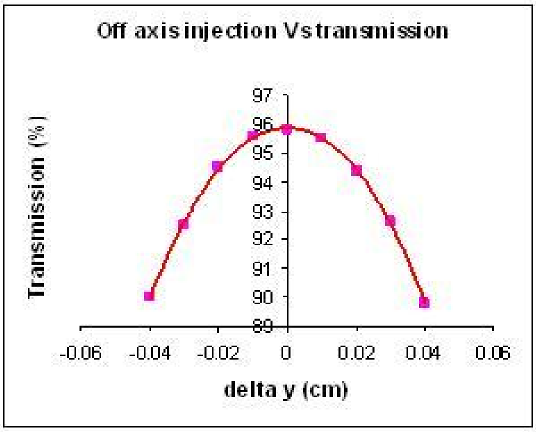

(b) y direction

Figure 2.8: Beam transmission vs off-axis injection

2.5.3.2 Beam tilt

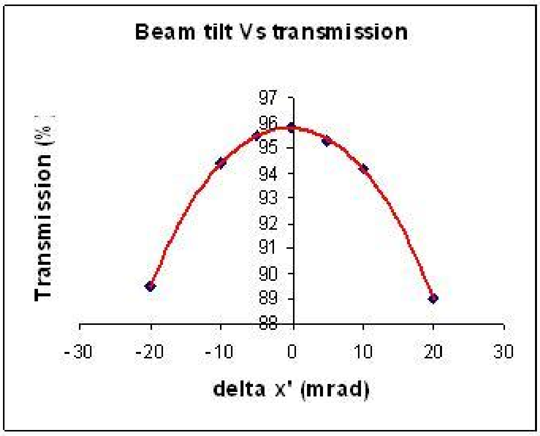

(a) x direction

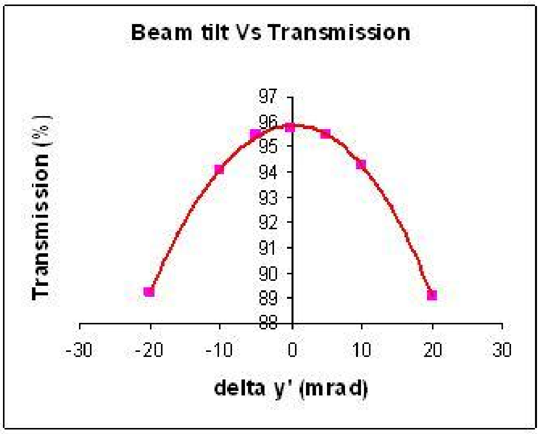

(b) y direction

Figure 2.9: Beam transmission vs Beam tilt

Figure 2.9 show the effect of beam tilt, i.e. the beam coming in along the design axis, but not parallel to it. Again, this could be a consequence either of an error in the design of the transport line, or because the RFQ itself is tilted with respect to the design axis. It can be seen that the acceptance criterion of 93% transmission is met for tilts of 15 mrad or less, which is again not very stringent

2.5.3.3 Energy Deviation and Energy spread

The beam dynamics simulations of the previous section assume that the deuteron beam coming from the ion source is monoenergetic, and all the particles have energy of exactly 50 keV. Obviously, in reality the beam will have an energy spread, and the mean energy of the beam could also deviate from the nominal value of 50 keV.

Figure 2.10a shows the effect of deviations in input energy of the beam from 50 keV. It can be seen that the mean energy of the deuterons emerging from the ion source should be within 3 keV of the nominal value, i.e. the ion source energy must be constant to better than 6%. This places an important constraint on the power-supply of the ion source.

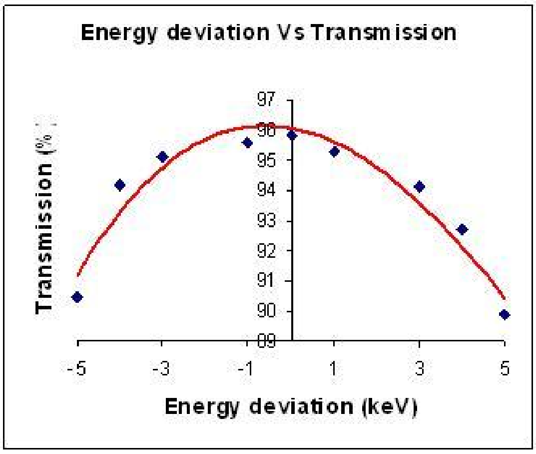

(a) Transmission vs Beam energy deviation

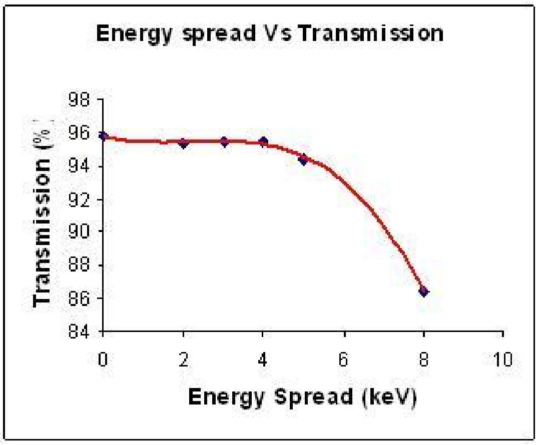

(b) Transmission vs Energy spread

Figure 2.10: Beam transmission vs Energy deviation and energy spread

Figure 2.10b shows the effect of a finite energy-spread in the deuteron beam. It can be seen that an energy-spread of more than around 6 keV, i.e. 12 %, is inadmissible.

Besides the transmission, a finite energy-spread can also degrade (i.e. increase) the emittance of the beam.

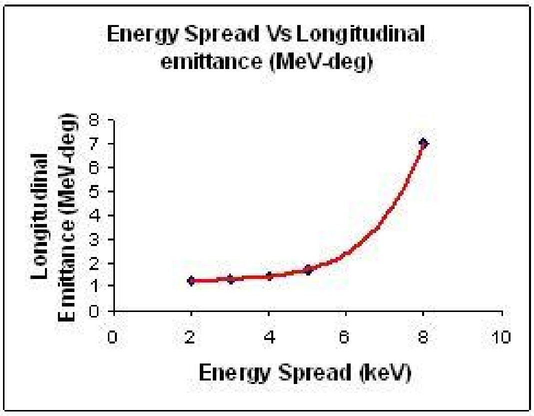

(a) Longitudinal emittance vs Energy spread

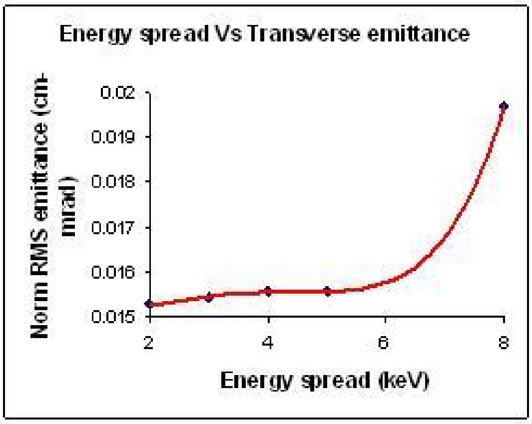

(b) Transverse emittance vs Energy spread

Figure 2.11: Emittances vs energy spread

Figures 2.11 a & b, shows the blow-up of the transverse as well as longitudinal emittance of the beam as a function of increasing energy-spread. It can be seen, for example, that the transverse emittance increases from the nominal value of 0.15π mm-mrad, to 0.16 π mm-mrad, i.e. an increase of about 7%, for an energy-spread of around 6 keV (i.e. 12%), which is acceptable.

2.5.3.4 Current Variation

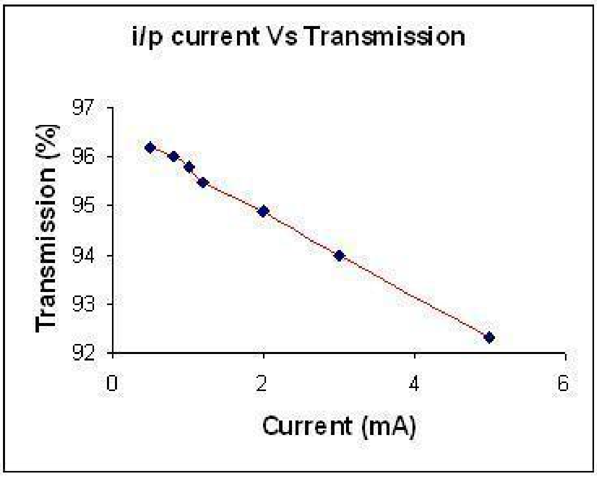

Figure 2.12: Transmission vs Input Current

Since the RFQ has been designed for a current of 1 mA, it is clear that lower currents can be easily accommodated but at the cost of emittance growth. It is of interest however, to ask if the present design can handle higher currents. Figure 2.12 shows that the present design, though optimized for 1 mA, will actually be able to handle a current of somewhat more than that (around 4 mA), even with the acceptance criterion of 93% transmission. This could prove useful in any plans for a future upgrade in the current capability of the RFQ linac. In the above studies it was observed that the emittance growth is less at higher currents.

2.5.3.5 Vane voltage variation and tilt

Besides errors in the parameters associated with the beam, we have also studied errors associated with the vane voltage. Figure 2.13a shows the beam transmission as a function of the fractional deviation of the vane voltage from its nominal value (Vfac) of 44 kV.

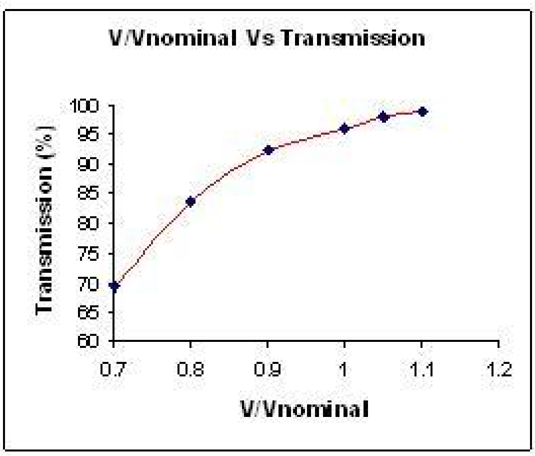

(a) Transmission vs Vane voltage deviation

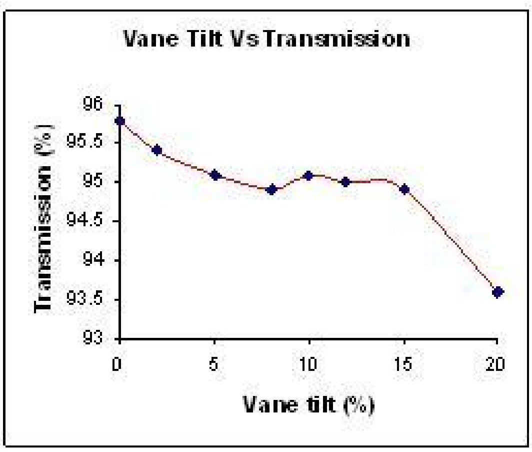

(b) Transmisson vs voltage tilt

Figure 2.13: Transmission vs Vane voltage deviation and tilt

It can be seen that while higher vane voltages can be tolerated, the transmission drops sharply when the vane voltage decreases below the design value. From the plot it is clear that a decrease in vane voltage of more than 10% is unacceptable. Figure 2.13b shows a plot of the beam transmission as a function of the 'tilt' in the vane voltage, i.e. the vane voltage varies longitudinally – the vane is not a perfect equipotential. It can be seen that 'tilts' of up to 20% are acceptable.

2.5.3.6 Input emittance variation

The RFQ is designed for an input normalized rms emittance of 0.015 π cm-mrad. It can efficiently transmit a beam with lower emittance. It is however, important to study the effect of a higher input emittance on the beam transmission through the RFQ.

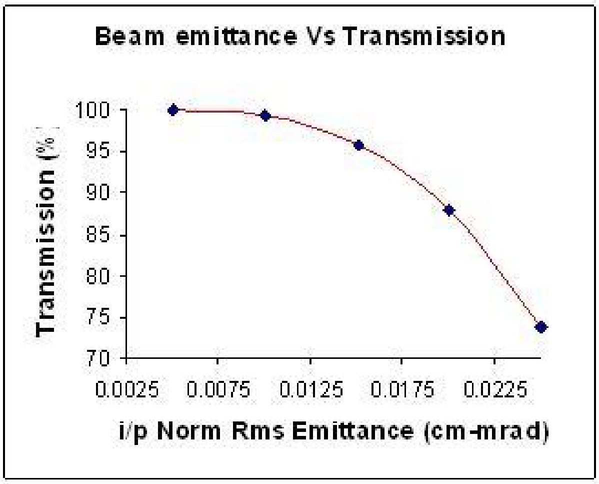

Figure 2.14: Transmission vs Input emittance

Figure 2.14 shows that the transmission drops very rapidly if the emittance exceeds 0.0175 π cm-mrad. This puts a constraint on the ion source to deliver a beam with emittance better than 0.0175 π cm-mrad.

Chapter 3

Electromagnetic simulations

3.1 Introduction:

In this chapter, we will study the RFQ structure, which is reponsible for putting such a large rf voltage on the vane tips near the axis. A large rf voltage can be obtained by driving the resonant circuit at its resonant frequency. The two most frequently used cavity structures of RFQ are the four vane structure [29], based on a wave guide, and the four-rod structure [30], based on lumped inductances and capactiances. Another type of RFQ structure has attracted interest more recently [31-35], which may be called a four-vane with windows RFQ. This type of structure may be described as an intermediate resonator configuration between the four-vane and the four-rod RFQ.

The four-vane cavity consists of 4 vanes symmetrically placed within a cavity as shown in Figure3.1. The cavity is operated in a TE_{210}- like mode, which is obtained from the natural TE_{211} mode, by tuning specially configured end cells to produce a longitudinally uniform field throughout the interior of the cavity.

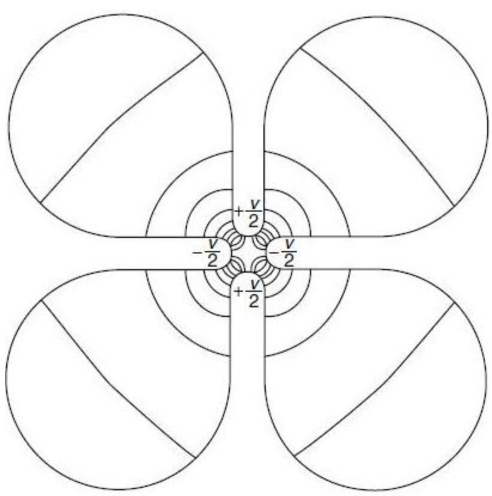

Figure 3.1: Cross section of four-vane RFQ cavity

The transverse electric field is localized near the vane tips, and the magnetic field, which is longitudinal in the interior of the cavity, is localised mostly in four outer quadrants. The four-vane cavity is used in the high-frequency range, above 200 MHz. The effeciency of the four-vane cavity is relatively high, because the vane charging current are distributed very uniformly along the length of the vanes.

Whereas the four-rod structure, shown in Figure 3.2, is used mostly in the lower-frequency range, below about 200 MHz. The rods are charged from a linear array of conducting support plates or inductive stems. In ideal quadrupole geometry, adjacent rods are at opposite potentials, and opposite rods are at the same potential.

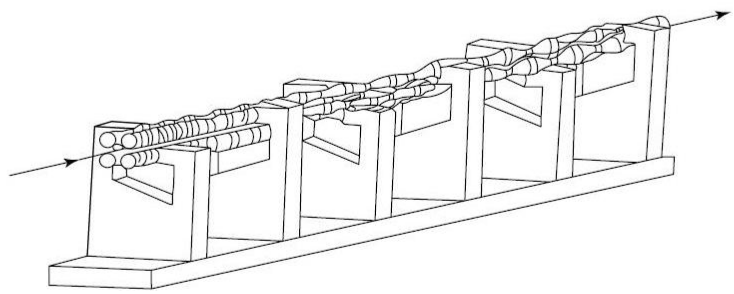

Figure 3.2: Cross section of four-vane RFQ cavity

The electric field is concentrated near the rods, and the magnetic fields are concentrated near the inductive stems. The charging currents flow longitudinally along the base from one stem to the next. The current density on the stems is higher than that of the vanes of the four-vane structure, which tends to reduce the efficiency compared with the four-vane cavity. At higher frequencies, the rods become smaller and can be more difficult to cool than vanes. This can be a disadvantage for high-frequency applications, and is one of the main reason for choosing a four-vane cavity structure for our 400 keV, 350 MHz RFQ. The detailed design of the RFQ requires intensive computer simulations to define the cavity shape as well as the optimal configuration of many of the components like the Tuners, End cells and Dipole stabilizer rods. In this chapter, we present the 2D and 3D electromagnetic simulation results of our 400 keV deuteron RFQ

3.2 Electromagnetic simulations:

The 2D and 3D electromagnetic simulations of the RFQ cavity was done using a computer codes SUPERFISH [36] and CST Microwave studio [37].

3.2.1 2D cavity design

The geometry of the vanes for a given resonant frequency of the RFQ is obtained using SUPERFISH (SF). The ideal vanes shape of the RFQ are hyperbolic. Since the hyperbolic shape vanes are difficult for machining, the vanes are broaden away from axis in steps. The shape of the vane is derived by numerical simulations using RFQFISH. The details of the geometry of the vanes are shown in Figure 3.3

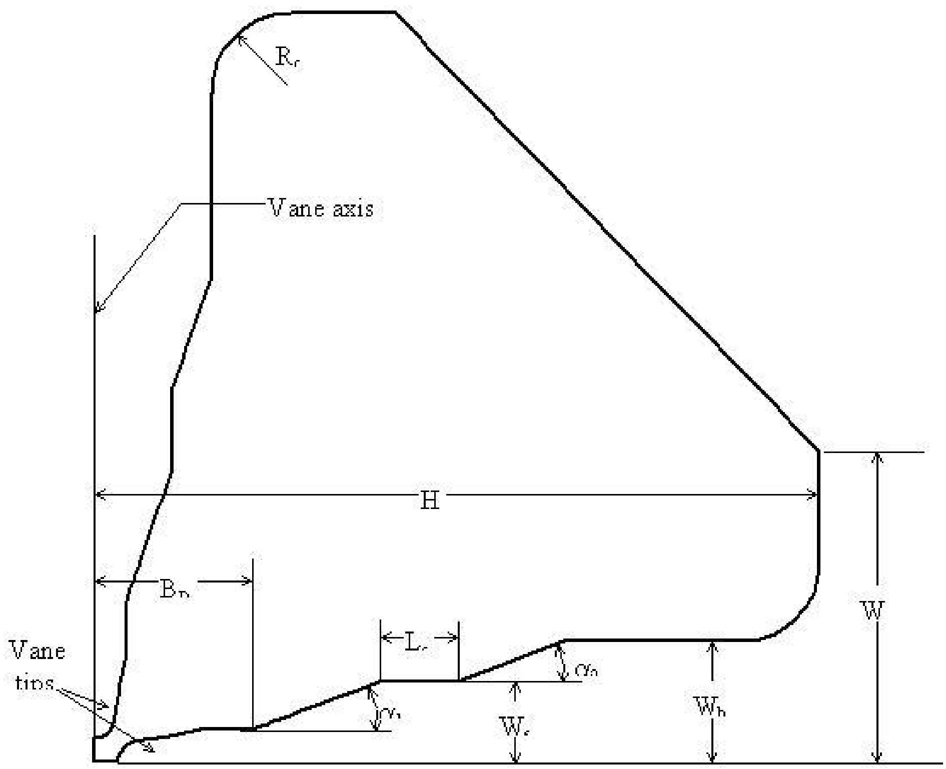

(a) Parameters of one quadrant of RFQ

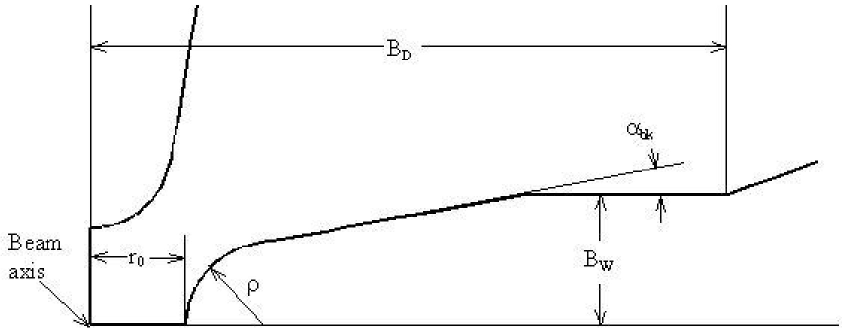

(b) Geometrical details near the RFQ vane tip

Figure 3.3: Geomtery of the vanes of RFQ

The necessary information for generating the geometry as well as to calculate the RF parameters of the RFQ are: (1)Resonant frequency (2) Aperture at exact quadrupole symmetry of the vanes (3) Vane tip radius (4) Vane gap voltage. The various parameters shown in Figure 3.3 are varied to minimize the power dissipation in the RFQ geometry for a given desired resonant frequency. The optimized geometric parameters and corresponding RF parameters of the RFQ are shown in table 3.1.

Table 3.1: Optimized geometric and RF parameters of RFQ

Parameters	Value	Units
Average bore radius (r_0)	0.1873	cm
Vane Voltage (V_g)	44	kV
Radius of Curvature of vane tip (ρ_t)	0.1783	cm
Vane shoulder half width (W_s)	1.0	cm
Vane base half width (W_b)	1.0	cm
Corner Radius (R_c)	1.0	cm
Breakout angle (α_{bk})	30	deg
Blank width (B_w})	0.4	cm
Blank Depth (B_d)	1.5	cm
Vane angle 1 (α_1)	20	deg

Vane angle 2 (α_2)	0	deg
Vane Heigth (H)	8.1125	cm
Resonant frequency	348.5	MHz
Quality factor	6600	
Ratio of $\frac{E_{max}}{E_{kp}}$	1.68	
Total RF power* (1.3*SF)	55.5	kW
Mode Separation	7.7	MHz

**Total power is 1.3 times SUPERFISH simulations*

The variation of the resonant frequency as a function of the three main parameters (a) average bore radius (r_0) (b) Transverse radius of curvature (ρ_t) (c) Corner radius (R_c) was studied, which are as shown in Figure 3.4.

Based on these studies, we have obtained an empirical formula for fractional change in the resonant frequency which is given in equation 3.1.

$$\frac{\triangle f}{f} = 0.375\frac{\triangle r_0}{r_0} - 0.181\frac{\triangle \rho_t}{\rho_t} - 0.114\frac{\triangle R_c}{R_c} \tag{3.1}$$

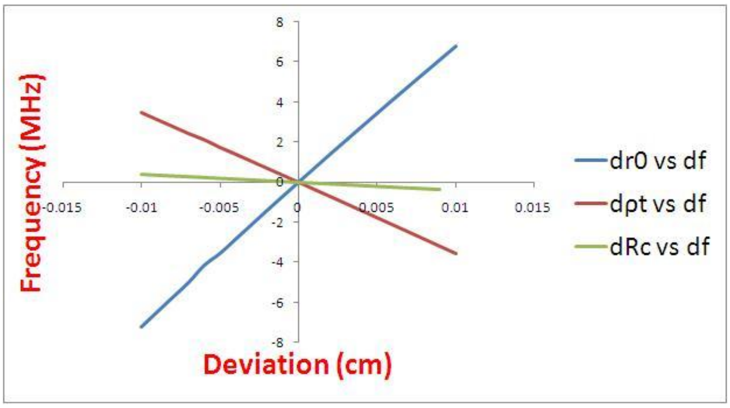

Figure 3.4: Variation of resonant frequency

The optimized cross section and the average power density along the perimeter of 400 keV RFQ are shown in Figures 3.5 (a) & (b)

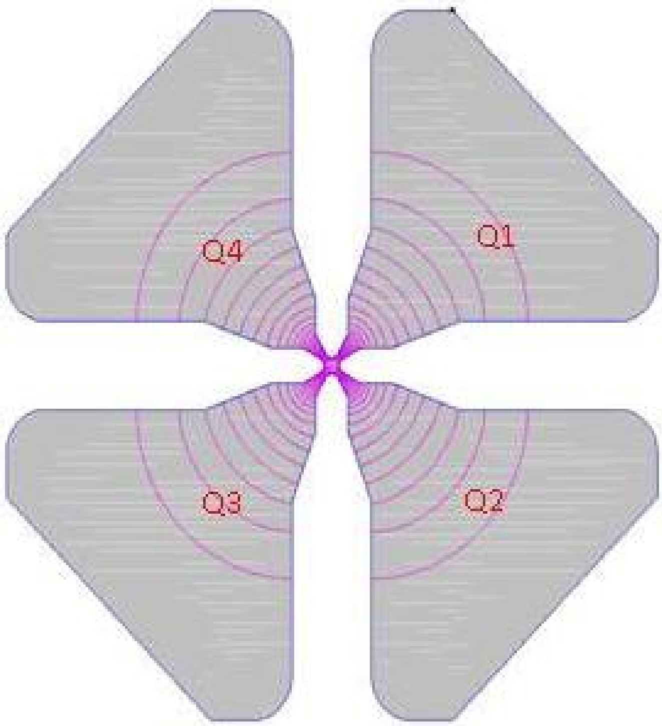

(a) Cross section of the RFQ

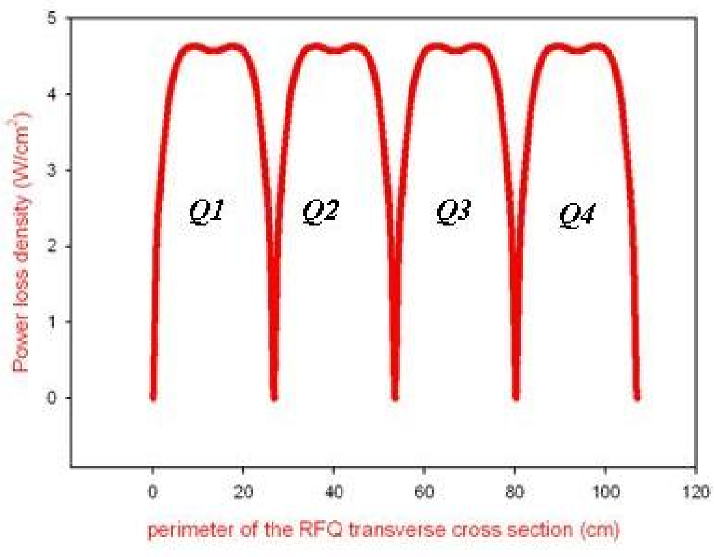

(b) Average power density ($^{W}/_{cm^2}$) along the perimeter of the RFQ

Figure 3.5: Cross section and Power density along the perimeter

3.2.1.1 Vane displacement errors

We have studied the effect of the displacement of opposite vertical vanes of RFQ in +X direction as shown in Figure 3.6, on the resonant frequency as well as the field distribution. This will create the assymetry in the structure and leads to more dipole contribution in the field distribution, which in turn reduces the beam transmission.

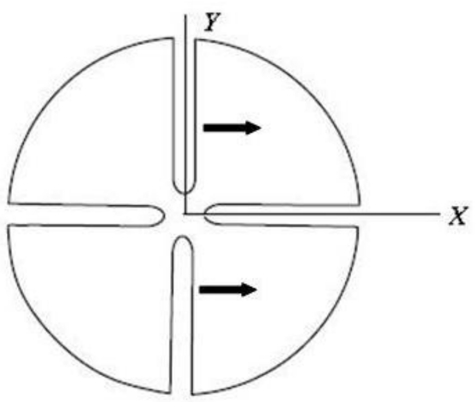

Figure 3.6: Displacement of vertical vanes of RFQ

The variation of resonant frequency and dipole contribution in the fields as a function of vanes displacements are shown in Figures 3.7 and 3.8.

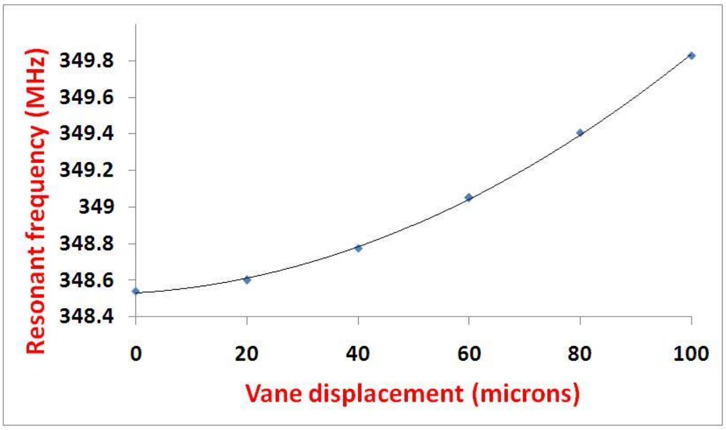

Figure 3.7: Vane displacement vs Resonant frequency of RFQ

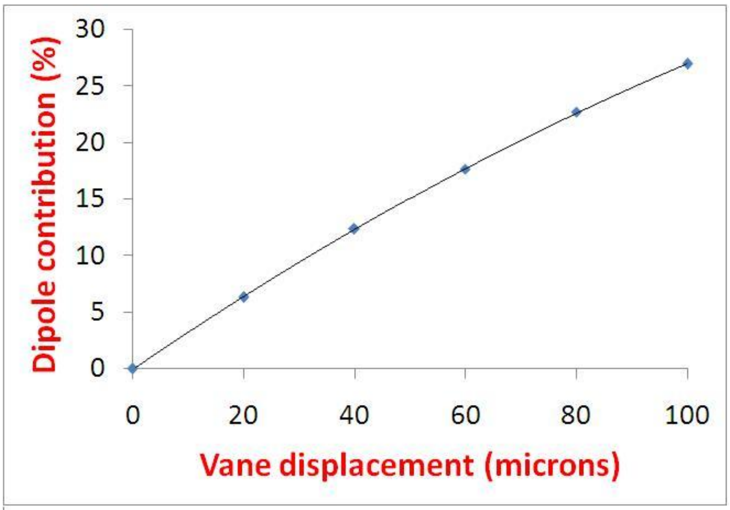

Figure 3.8: Dipole contribution vs Vane displacement

3.2.2 3D cavity design

In order to study the effect of Tuners, Vacuum ports, Beginning cell (BC), End cell (EC) and Dipole stabilizers rods of the RFQ, where there is no axial symmetry a complete 3D electromagnetic simulations are needed. We have used the computer code CST Microwave studio for these studies.

3.2.2.1 Tuners

Tuners are used to adjust the frequency of the RF cavity. The tuners are cylindrical rods which when pushed inside the cavity decrease the magnetic volume of the cavity. This leads to decrease in the inductance of the RF cavity and hence an increase in the resonant frequency. We have planned to use 16 tuners in the 1.03 m long 400 keV RFQ. In the simulations, we have modeled one quadrant of 10 cm long RFQ equipped with one tuner as shown in Figure 3.9. The variation of the resonant frequency with the tuner radius and depth are shown in Figure 3.10. The tuning sensitivity of the tuner is calculated to be $\sim 26.7\, {}^{kHz}/_{mm\, tuner}$ for 1 m long RFQ. So overall tuning range of the tuner is equal to 0.43 MHz/mm with all the 16 tuners

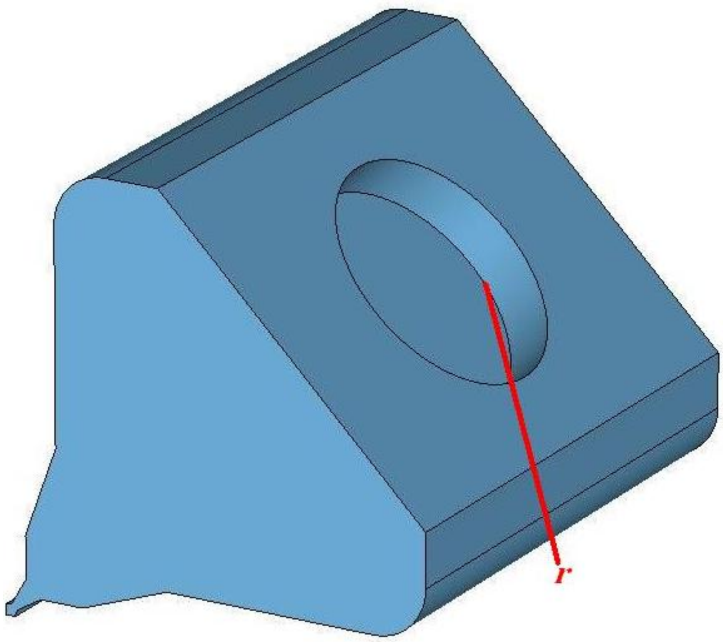

Figure 3.9: Simulated model of tuner

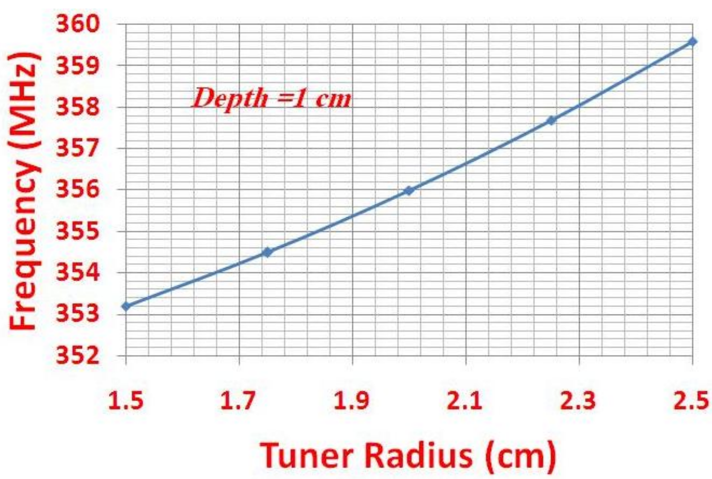

(a) Resonant frequency vs tuner radius

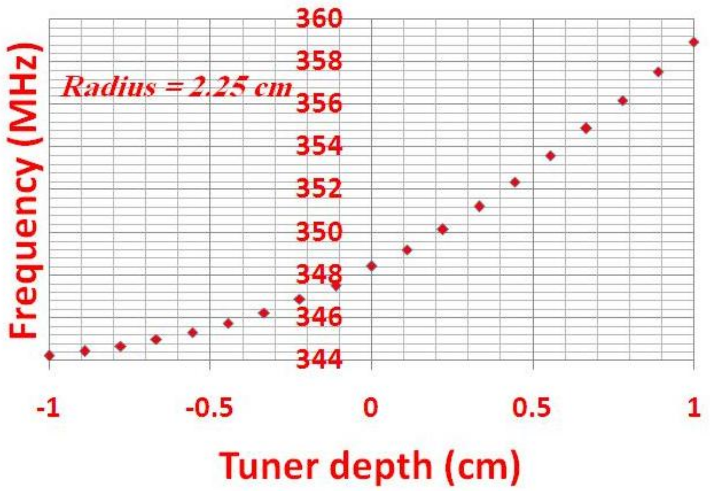

(b) Resonant frequency vs tuner depth

Figure 3.10: Variation of Resonant frequency with tuner radius and depth

When the tuners are inserted into the RFQ cavity the magnetic field lines will bend as shown in Figure 3.11a and their concentration at the tuner edges will increase. As a result the surface loss density will increase at those points, which is shown in Figure 3.11b. The surface loss density calculated by CST is the peak value not the average power loss density. Since, it calculates as R_sH^2 instead of $^{R_s}/_2$.

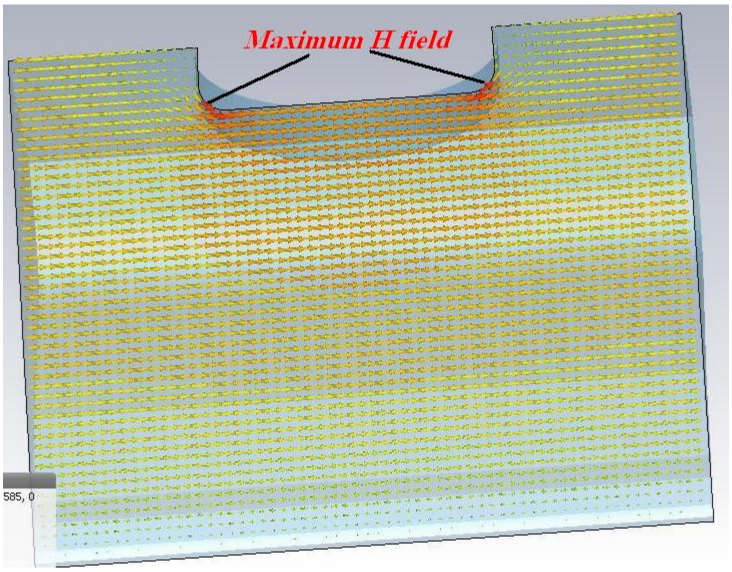

(a) Magnetic field distribution near tuners

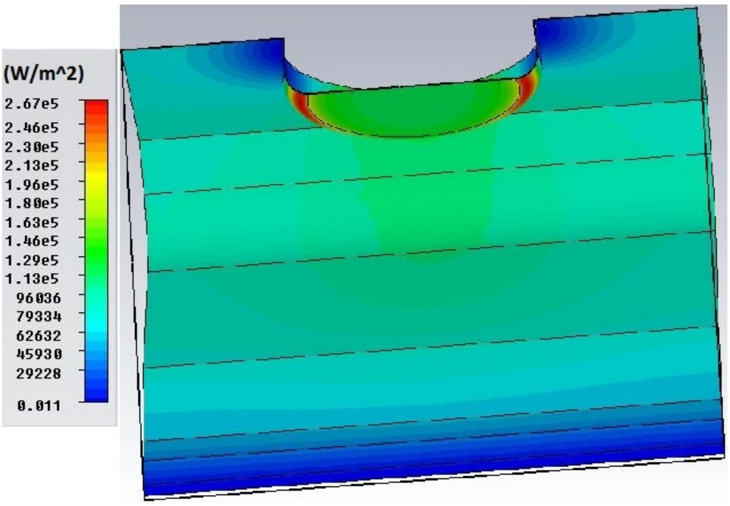

(b) Peak Surface loss density (W/m^2)

Figure 3.11: Magnetic field distribution and surface loss density near the tuners

To reduce the loss density blend edges are given on the corners of the tuners as shown in Figure 3.9. The variation of the peak surface loss density as a function of the blend radius (r) is shown in Figure 3.12.

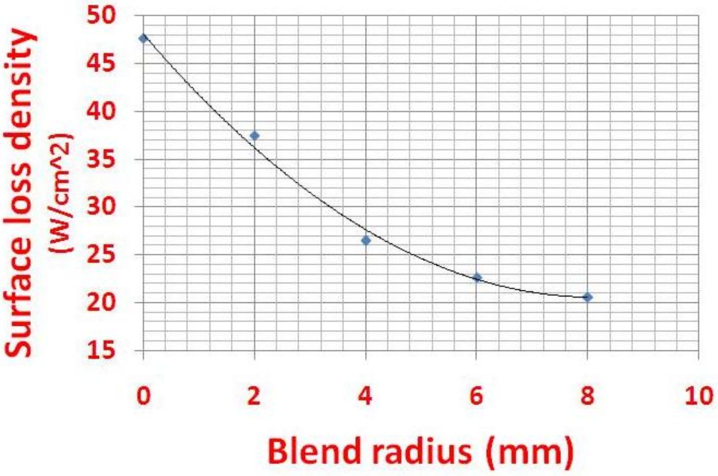

Figure 3.12: Peak Surface loss density vs blend radius

3.2.2.2 Vacuum ports

The operating vacuum of the RFQ will be in the range of 10^{-7}Torr. The RFQ vacuum system has to provide sufficient pumping to maintain the vacuum to a desired level. In order to achieve this vacuum, 8 rectangular pumping ports are provided on the RFQ walls. Each pumping port consisting of 5 slots of dimensions 30 x 14 mm and each slots are separated by 10 mm. In order to reduce the penetration of the fields into vacuum port, we planned to make them in small slots instead of a single large opening. This will also reduce the peak surface loss density as well as resonant frequency deviation.

The effect of the pumping port opening on the resonant frequency have been studied and found that the resonant frequency reduces by 0.6 MHz with all the vacuum ports. A vacuum port modeled in CST is shown in Figure 3.13a and peak surface loss density ($^{W}/_{m^2}$) is as shown in Figure 3.13b.

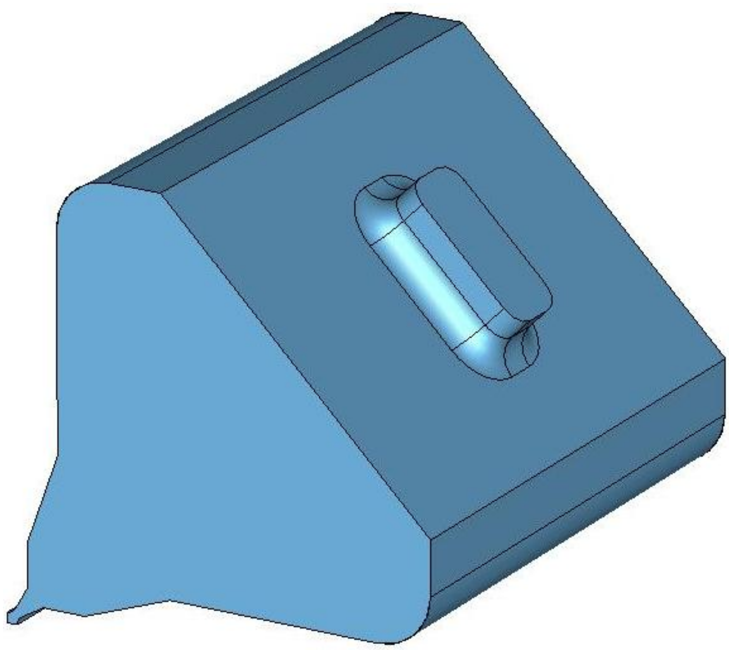

(a) CST model of Vacuum port

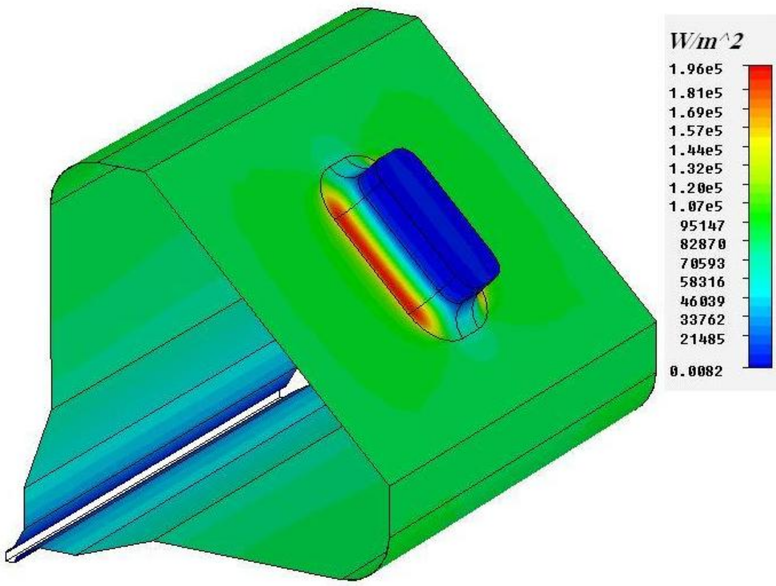

(b) Peak Surface loss density

Figure 3.13: Simulation model of RFQ with one vacuum port slot

.

3.2.2.3 BC and EC designs:

In real RFQ, which is closed at both ends with a conductive walls, the magnetic field H_z has to become zero according to the boundary conditions. It can be achieved by a particular geometry of the electrodes at the beginning and end of the cavity, called end cells. The Figure 3.14, shows that the vanes do not extend up to the end wall and also the undercuts are provided on the vanes.

This allows the magnetic field divide into half and turn around the electrodes and merge with the fields in the adjacent quadrants. In this way, the field H satisfies the boundary condition at the end walls without changing the longitudinal uniformity of the potential between the electrodes.

To maintain the longitudinal uniformity of the potential between the electrodes, the ends cell have to be tuned to the required quadrupolar cross-sectional frequency (f_{Q2d}). In order to reduce the computation time, we have modeled only 10 cm for BC and EC respectively. A resonant cavity made of several elements whose individual resonant frequencies differ slightly with each other, will resonate at a frequency obtained by averaging the single element frequencies, weighted by the amount of energy stored in each element [38-39].

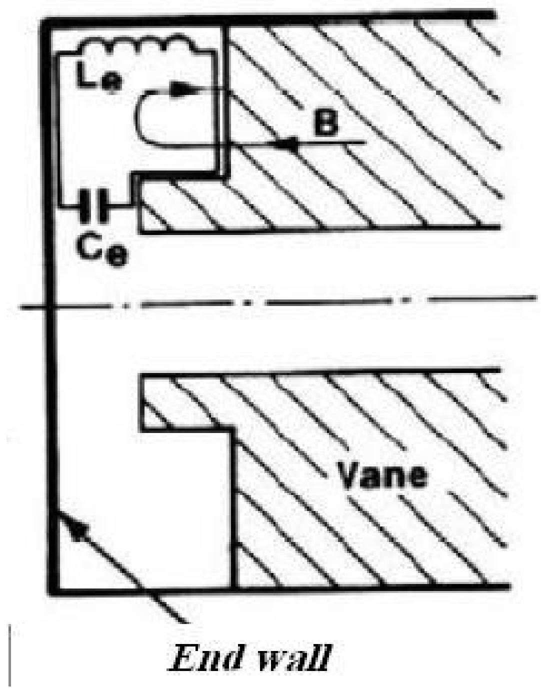

Figure 3.14: Magnetic field at the End cells for quadrupole mode

If the resonant frequencies of the BC, EC and ideal RFQ cavities are f_{BC}, f_{EC} and f_{Q2d} then the frequency of the real RFQ is given by

$$f_{realRFQ} \sim \frac{f_{BC}l_{BC} + f_{Q2d}l_{RFQ} + f_{EC}l_{EC}}{L} \tag{3.2}$$

If BC and EC are tuned exactly to f_{Q2d}, then the RFQ with undercuts will resonate at f_{Q2d}. The schematic and the CST model of the end cell are shown in Figures 3.15 (a) & (b). The end cells are tuned to the desired quadrupole resonant frequency by varying the overhang height 'a', taper height 'b' and taper depth 'c'. The optimized parameters of the BC and EC are shown in Table 3.2.

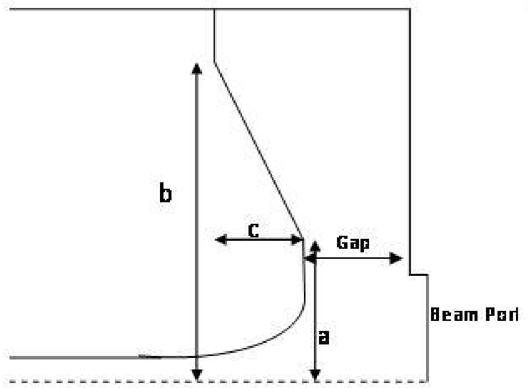

(a) Schematic of End cell

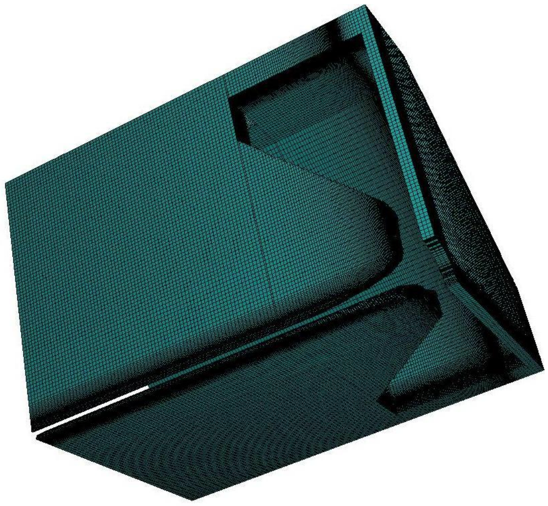

(b) Simulation model of End cell

Figure 3.15: End cell

Table 3.2: Optimized parameters of the End Cells

Parameters	BC	EC	Units
Overhang Height (a)	2.50	2.50	cm
Taper Height (b)	6.50	6.50	cm
Taper depth (c)	3.65	3.45	cm
Gap	0.55	0.55	cm
Beam port radius	1.00	1.00	cm

The power loss density is a major concern for a CW operation of RFQ. The distribution of magnetic field at the end cell is shown in Figure 3.16 (a). As it is seen from the Figure 3.16 (a), the magnetic field is concentrated near the vane under-cuts, which results in increasing the power loss density. Sharp corners have to be eliminated to reduce the losses and for a particular size of blend edges the peak power loss density on the end cells is shown in Figure 3.16 (b). The maximum peaf surface loss density observed from the simulation was $\sim 100\,{}^{W}\!/_{cm^2}$, so a special cooling arrangement has to be provided near the end cuts. If the RFQ operates in a pulsed mode of duty cycle 0.1 % then the average loss density will drastically reduce to $\sim 0.11\,{}^{W}\!/_{cm^2}$, so the cooling is not required. So it is indeed very important to decide in advance whether to operate the RFQ in pulsed or CW mode. Since the 400 keV RFQ was planned to operate in CW mode, a special cooling arrangement has been provided at the end cuts.

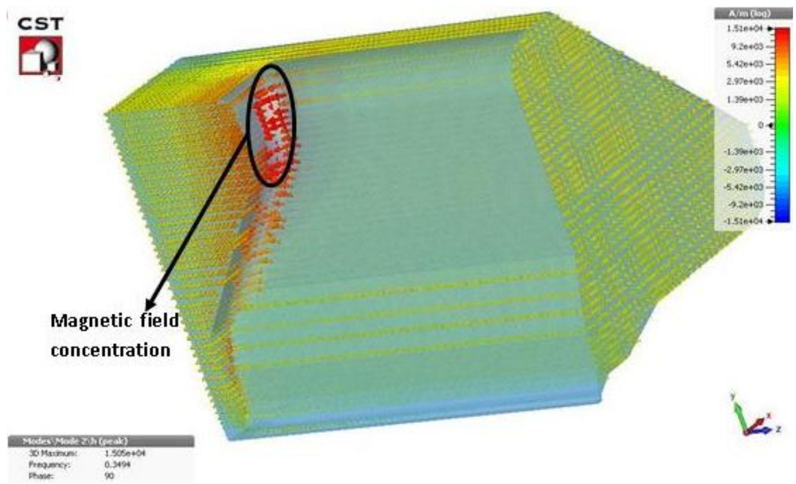

(a) Magnetic field distribution

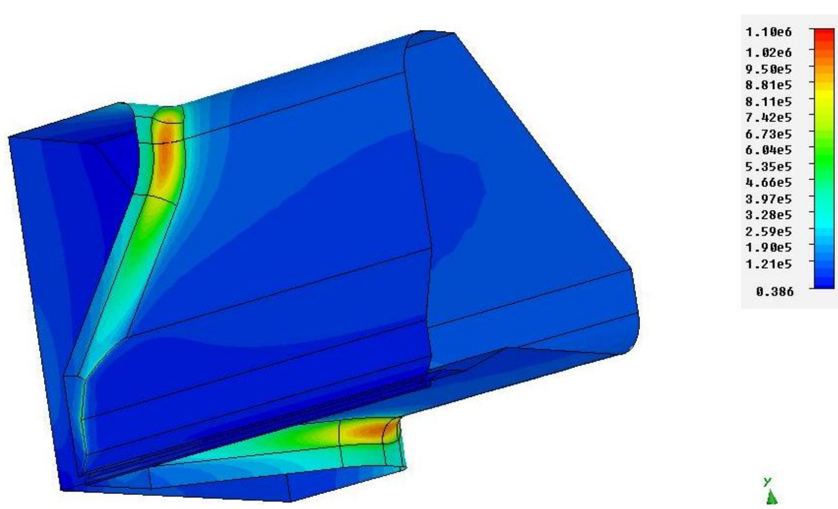

(b)Peak Power loss density (${}^{W}\!/_{m^2}$)

Figure 3.16: Magnetic field distribution and Peak Power loss density (${}^{W}\!/_{m^2}$) at the end cells

3.2.3 Dipole Stabilizer Rods (DSRs):

The vane undercuts are provided at the beginning and end of the RFQ, in order to get the required quadrupole mode. While optimizing the undercuts the unwanted dipole mode frequencies will increase and come closer to the quadrupole mode frequency. As a result, the structure will become sensitive to the perturbations. Several methods [40-42] have been proposed and used to make the RFQ structure insensitive to perturbations. In our 400 keV RFQ, Dipole-mode Stabilizer Rods (DSRs) are used, because of their ease in fabrication.

The DSRs are devices employed in order to reduce a priori the effect of perturbation on the operating mode of a four-vane RFQ caused by neighboring dipole modes by increasing the frequency spacing between the Quadrupole (TE_{210}) and Dipole modes, without affecting the TE_{210} mode frequency [43-44].

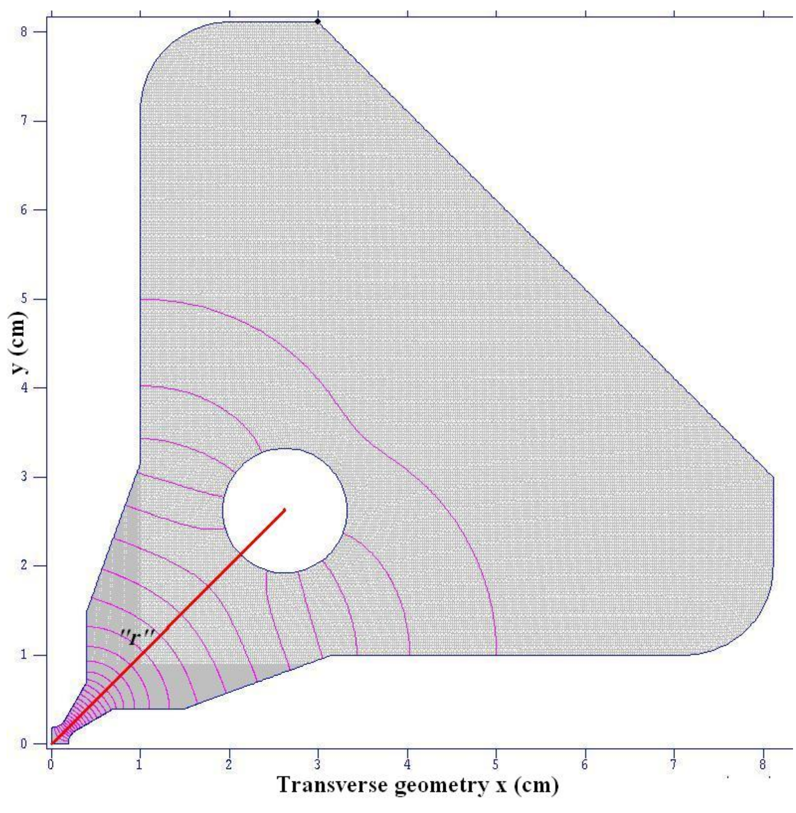

(a) $1/4^{th}$Cross section of RFQ with DSR

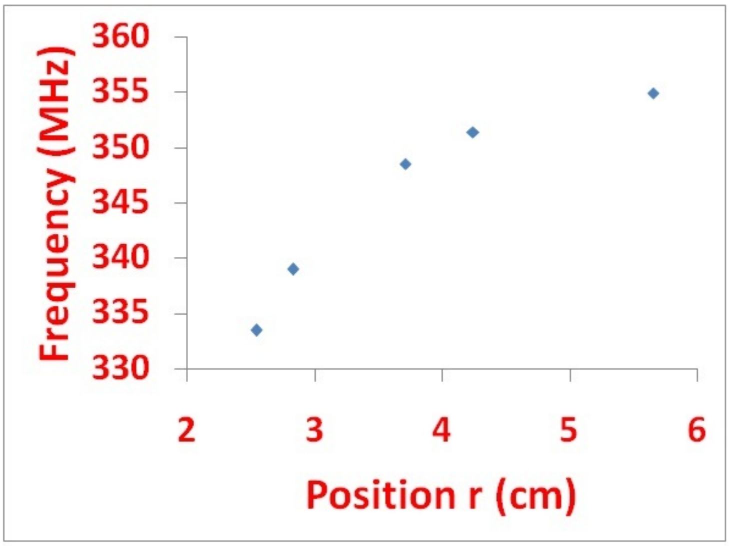

(b) Variation of resonant frequency with position of DSRs

Figure 3.17: Cross section of RFQ and Variation of Resonant frequency with DSRs

The parameters of the DSRs, to be designed include the diameter "D", the position "r" between the centre of the rod to beam axis, and the length of the rods "l". The diameter "D" of the rods should not be too large, otherwise the operating mode will be disturbed. It should not be to small either, considering the mechanical strength and convenience of possible water cooling. For the 400 keV RFQ, D=14 mm is finally adopted.

Since the rods should have only a small effect on the operating mode, the DSRs are placed where the electric and magnetic energy densities are equal. The computer code SUPERFISH is used to find the proper position "r" of the DSRs. The $1/4^{th}$cross section of the RFQ with DSRs is shown in Figure 3.17 (a). The variation of the resonant frequency with position is shown in Figure 3.17 (b).

Once the position "r" and diameter "D" of DSRs are chosen the length of the rods are varied to move the dipole frequencies far away from the operating mode. Without DSRs the separation between dipole and quadrupole modes is only 0.5 MHz. The simulated model of the RFQ equipped with DSRs is shown in Figure 3.18.

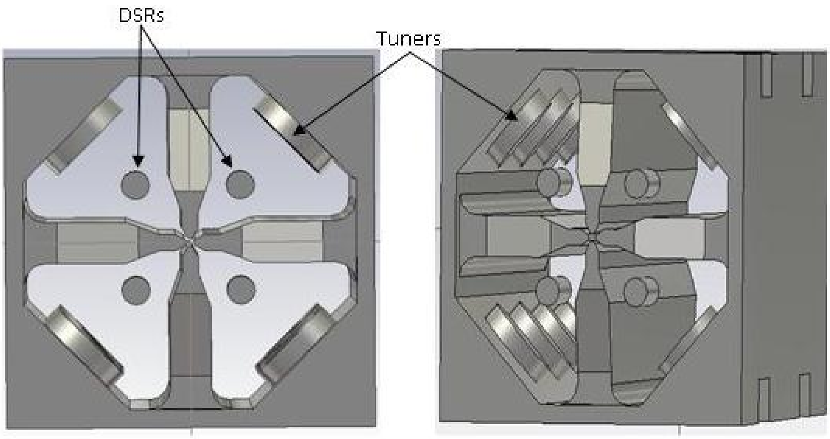

Figure 3.18: Simulated mode of RFQ equipped with DSRs

The variation of the dipole and quadrupole mode frequencies with length of the DSRs of radii 7 mm for our 400 keV RFQ is shown in Figure 3.19. Based on these simulations, we have chosen the length of the DSRs to be $\sim$ 12 cm. The maximum peak surface loss density of 25 $^{W}/_{cm^2}$ was observed on the DSRs which is shown in Figure 3.20.

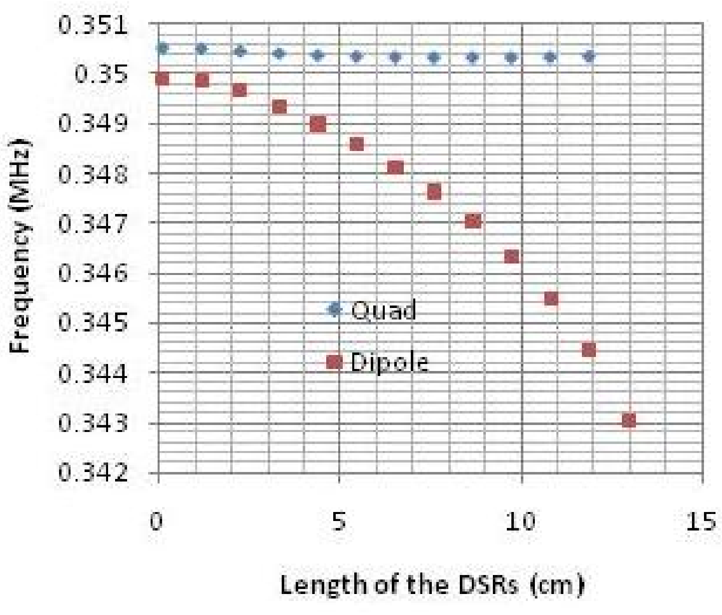

Figure 3.19: Dipole and Quad frequencies Vs DSRs length

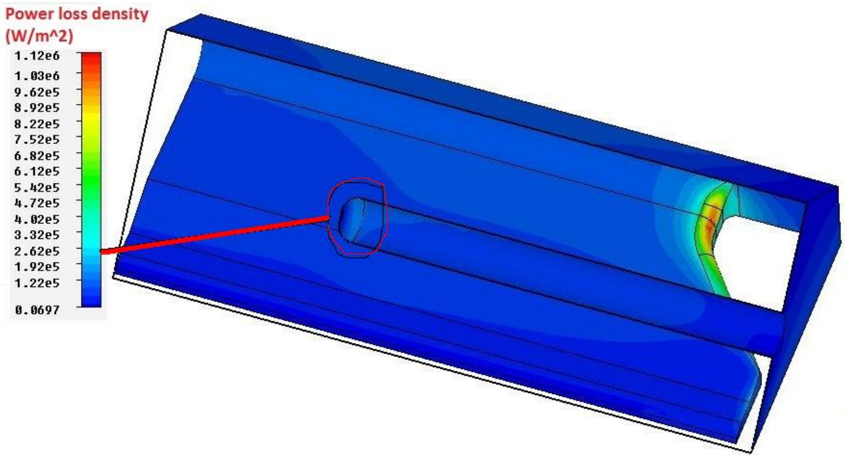

Figure 3.20: Peak Power loss density (W/cm^2)

Chapter 4

Perturbative Analysis of RFQ

4.1 Introduction

An important issue for high intensity RFQs is to keep the beam losses as low as possible, in order to allow reliable and safe maintenance of the machine. Typically, beam dynamics outcome driven by the above constraint results in an inter-vane voltage variation should not exceed a few percent with respect to the design value. So an analytical tool is needed to understand the effect of geometric perturbations on the field distribution of an RFQ. This will also give an indication on the permitted ranges of geometrical errors in the RFQ fabrication. The perturbative analysis of the RFQ have been studied using a transmission line analysis [45-49]. In this chapter, we present the theory of pertubative analysis of four-vane RFQ based on the 5-wire transmission line analysis [50] and present the results of two case studies. Based on the this theory, we have written a tuning program based on the tuning strategy proposed by LNL [51]. We will also discuss the theory of tuning algorithm and the results of a case study.

4.2 Transmission Line Analysis of ideal RFQ

As a starting point, we will consider the case of an ideal RFQ (i.e., without errors). A four vane RFQ resonator is based on a trasfer line quadrupole mode (TE_{21n}), with dispersion relation:

$$\omega^2 = \omega_0^2 + k^2 c^2 \tag{4.1}$$

where $\omega_0$is the quadrupole cut-off frequency, k is the wave number and c is the speed of light. For such mode configuration, the electric (which has only transverse components) and magnetic (have only longitudinal component) fields can be expressed in the following way [52]:

$$\mathbf{E}(\mathbf{x},\mathbf{y},\mathbf{z}) = V(z)\,\mathbf{e}(\mathbf{x},\mathbf{y})$$
$$\mathbf{H}(\mathbf{x},\mathbf{y},\mathbf{z}) = \frac{k_t}{j\omega\mu}\psi(x,y)\,V(z)\,\hat{i_z}$$

where $k_t = \frac{\omega_0}{c}$ and $\psi(x,y)$ is such that $\nabla_t^2\psi + k_t^2\psi = 0$, on the transverse section and $\frac{\partial\psi}{\partial n} = 0$ on the transverse section contour. The longitudinal behaviour of the field is determined by the function $V(z)$ that is the solution of the equation

$$V"(z) + k^2 V(z) = 0 \tag{4.2}$$

Such equation can also be derived from the following equivalen circuit of the RFQ

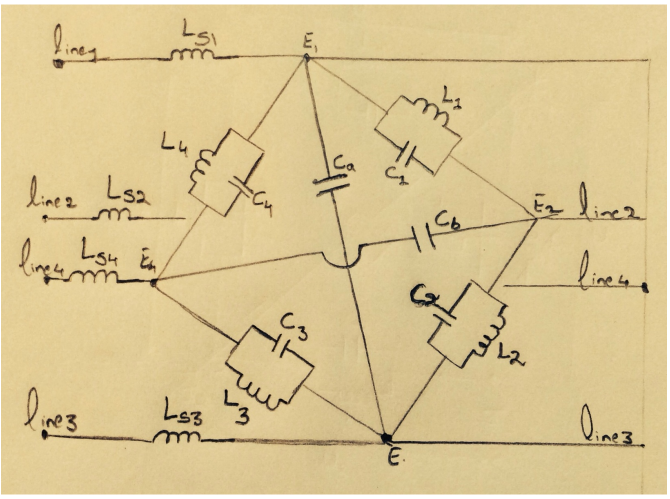

Figure 4.1: RFQ equivalent transmission line

In the above circuit the $L_{si}(i = 1, 2, 3, 4)$ are the inductances per unit length associated with the flow of longitudinal current alongs the vane tips, L_i and C_i are respectively the inductances (integrated in length) associated with the flux of magnetic field through the cross-section of the RFQ and the intra-vane capacitances (per unit length) and C_a and C_b are the capacitances per unit length between opposite vanes. The circuit equations for voltages are given by

$$\frac{dU_1}{dz} = j\omega L_{s1} I_1$$
$$\frac{dU_2}{dz} = j\omega L_{s2} I_1$$
$$\frac{dU_3}{dz} = j\omega L_{s3} I_1$$
$$\frac{dU_4}{dz} = j\omega L_{s4} I_1 \tag{4.3}$$

The circuit equations for currents are derived from Figure 4.2.

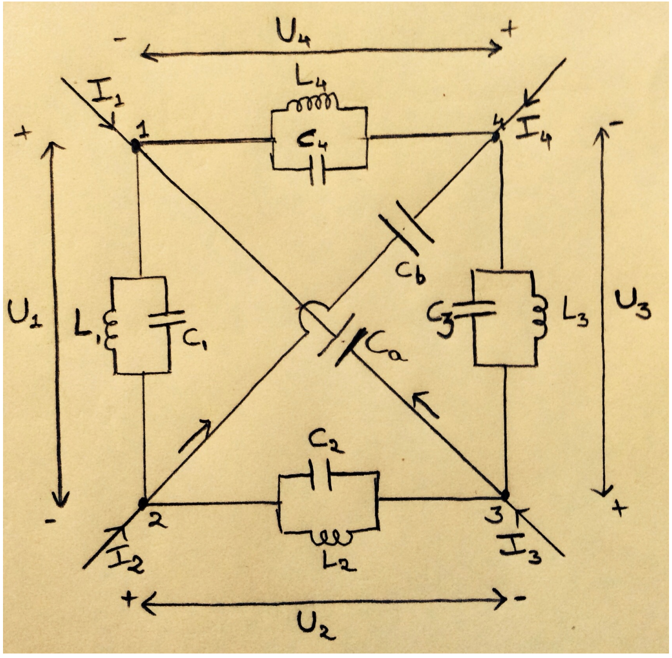

Figure 4.2: Equivalent circuit

By applying Kirchoffs Current Law (KCL) at junction1 as shown in Figure 4.2, we get

$$I_1 = Y_1 U_1 - Y_a U_3 - U_4 (Y_4 + Y_a) \tag{4.4}$$

Where $Y_i = j\omega C_i + \frac{1}{j\omega L_i}$, $i = \{1, 2, 3, 4\}$ and $Y_{a/b} = j\omega C_{a/b}$, Since $C_i's$ are capacitances per unit length and $L_i's$ are inductances integrated over length so the above equation becomes

$$\frac{dI_1}{dz} = Y_1 U_1 - Y_a U_3 - U_4 \left(Y_4 + Y_a\right) \tag{4.5}$$

Similarly for other junctions we get

$$\frac{dI_2}{dz} = Y_2 U_2 - Y_1 U_1 - Y_b \left(U_1 + U_4\right) \tag{4.6}$$

$$\frac{dI_3}{dz} = Y_3 U_3 - Y_2 U_2 - Y_a \left(U_1 + U_2\right) \tag{4.7}$$

$$\frac{dI_4}{dz} = Y_4 U_4 - Y_3 U_3 - Y_b \left(U_3 + U_2\right) \tag{4.8}$$

The above given circuit equations for voltages and currents are given by

$$\frac{d\bar{U}}{dz} = j\omega \underline{L_s} \bar{I} \tag{4.9}$$

$$\frac{d\bar{I}}{dz} = [j\omega \underline{C} + \frac{1}{j\omega}\underline{L}]\bar{U} \tag{4.10}$$

where $\bar{U} = \{U_1, U_2, U_3, U_4\}$ are intervane voltages and $\bar{I} = \{I_1, I_2, I_3, I_4\}$

$$\underline{C} = \begin{pmatrix} C_1 & 0 & -C_a & -C_a - C_4 \\ -C_b - C_1 & C_2 & 0 & -C_b \\ -C_a & -C_a - C_2 & C_3 & 0 \\ 0 & -C_b & -C_b - C_3 & C_4 \end{pmatrix} \underline{L} = \begin{pmatrix} \frac{1}{L_1} & 0 & 0 & -\frac{1}{L_4} \\ -\frac{1}{L_1} & \frac{1}{L_2} & 0 & 0 \\ 0 & -\frac{1}{L_2} & \frac{1}{L_3} & 0 \\ 0 & 0 & -\frac{1}{L_3} & \frac{1}{L_4} \end{pmatrix}$$

and $\underline{L_s} = \begin{pmatrix} L_{s1} & 0 & 0 & 0 \\ 0 & L_{s2} & 0 & 0 \\ 0 & 0 & L_{s3} & 0 \\ 0 & 0 & 0 & L_{s4} \end{pmatrix}$ Now from equations 4.9 & 4.10 we have

$$\frac{d^2\bar{U}}{dz^2} = [-\omega^2 \underline{L_s}\underline{C} + \underline{L_s}\underline{L}]\bar{U} \tag{4.11}$$

By putting $\underline{L_s}\ \underline{C} = \frac{1}{c^2} I_4$ so $\underline{L_s} = \frac{1}{c^2}\underline{C^{-1}}$

$$\frac{d^2\bar{U}}{dz^2} = [-\frac{\omega^2}{c^2} I_4 + \frac{1}{c^2}\underline{C}^{-1}\underline{L}]\bar{U} \tag{4.12}$$

$$\frac{d^2\bar{U}}{dz^2} = [-\frac{\omega^2}{c^2}I_4 + \underline{A}]\bar{U} \tag{4.13}$$

where $\underline{A} = \frac{\omega_0^2}{4c^2}\begin{pmatrix} 1+\frac{2}{1+h} & -1 & \frac{h-1}{1+h} & -1 \\ -1 & 1+\frac{2}{1+h} & -1 & \frac{h-1}{1+h} \\ \frac{h-1}{1+h} & -1 & 1+\frac{2}{1+h} & -1 \\ -1 & \frac{h-1}{1+h} & -1 & 1+\frac{2}{1+h} \end{pmatrix}$

This matrix $\underline{\mathrm{A}}$ can be diagonalized by a matrix $\underline{S} = \begin{pmatrix} \frac{1}{2} & \frac{1}{2} & \frac{1}{\sqrt{2}} & 0 \\ -\frac{1}{2} & \frac{1}{2} & 0 & \frac{1}{\sqrt{2}} \\ \frac{1}{2} & \frac{1}{2} & -\frac{1}{\sqrt{2}} & 0 \\ -\frac{1}{2} & \frac{1}{2} & 0 & -\frac{1}{\sqrt{2}} \end{pmatrix}$. In such a way that $\underline{S}^{-1}\underline{A}\ \underline{S} = \frac{\omega_0^2}{c^2}\begin{pmatrix} 1 & 0 & 0 & 0 \\ 0 & 0 & 0 & 0 \\ 0 & 0 & \frac{1}{1+h} & 0 \\ 0 & 0 & 0 & \frac{1}{1+h} \end{pmatrix}$

$$\frac{d^2(\underline{S}^{-1}\bar{U})}{dz^2} = [-\frac{\omega^2}{c^2}\underline{S}^{-1} + \underline{S}^{-1}\ \underline{A}\ \underline{S}\ \underline{S}^{-1}]\bar{U} \tag{4.14}$$

$$\frac{d^2\widehat{U}}{dz^2} = [-\frac{\omega^2}{c^2} + \underline{S}^{-1}\ \underline{A}\ \underline{S}]\widehat{U} \tag{4.15}$$

where $\underline{S}^{-1}\bar{U} = \widehat{U}$ and $\widehat{U} = \{U_q, U_m, U_{d1}, U_{d2}\}$ where U_q, U_m, U_{d1} *and* U_{d2} are the quadrupole, monopole and two dipole mode fields. Now we have different basis in which U_q, U_m, U_{d1} *and* U_{d2} are orthogonal.

4.2.1 Perturbation term:

In the above case we have assumed $L_i = L$ *and* $C_i = C, C_a = C_b = hC$ where i={1,2,3,4}. If we assume some mechanical errors then the perturbation term in the matrix A is given by

$$\delta[\frac{1}{c^2}\underline{C}^{-1}\underline{L}] = \frac{1}{c^2}[\underline{C}^{-1}\delta\underline{L} - \underline{C}^{-1}\delta\underline{C}\ \underline{C}^{-1}\underline{L}] \tag{4.16}$$

where $\delta\underline{L} = \begin{pmatrix} -\frac{\delta L_1}{L^2} & 0 & 0 & \frac{\delta L_4}{L^2} \\ \frac{\delta L_1}{L^2} & -\frac{\delta L_2}{L^2} & 0 & 0 \\ 0 & \frac{\delta L_2}{L^2} & -\frac{\delta L_3}{L^2} & 0 \\ 0 & 0 & \frac{\delta L_3}{L^2} & -\frac{\delta L_4}{L^2} \end{pmatrix}$ and

$$\delta\underline{C} = \begin{pmatrix} \delta C_1 & 0 & -\delta C_a & -\delta C_a - \delta C_4 \\ -\delta C_b - \delta C_1 & \delta C_2 & 0 & -\delta C_b \\ -\delta C_a & -\delta C_a - \delta C_2 & \delta C_3 & 0 \\ 0 & -\delta C_a & -\delta C_b - \delta C_3 & \delta C_4 \end{pmatrix}$$

The perturbative term in the new basis is given by

$$\delta k^2 = -\frac{\omega_0^2}{4c^2} \begin{pmatrix} \frac{\delta L_1+\delta L_2+\delta L_3+\delta L_4}{L} & \frac{\delta L_1-\delta L_2+\delta L_3-\delta L_4}{L} & \frac{\sqrt{2}(\delta L_1-\delta L_3)}{L} & \frac{\sqrt{2}(\delta L_4-\delta L_2)}{L} \\ 0 & 0 & 0 & 0 \\ \frac{\sqrt{2}(\delta L_1-\delta L_3)}{(1+h)\,L} & \frac{\sqrt{2}(\delta L_1-\delta L_3)}{(1+h)\,L} & \frac{2(\delta L_1+\delta L_3)}{(1+h)\,L} & 0 \\ \frac{\sqrt{2}(\delta L_4-\delta L_2)}{(1+h)\,L} & \frac{\sqrt{2}(\delta L_2-\delta L_4)}{(1+h)\,L} & 0 & \frac{2(\delta L_2+\delta L_4)}{(1+h)\,L} \end{pmatrix}$$
$$- \frac{\omega_0^2}{4c^2} \begin{pmatrix} \frac{\delta C_1+\delta C_2+\delta C_3+\delta C_4}{C} & 0 & \frac{\sqrt{2}(\delta C_1-\delta C_3)}{(1+h)\,C} & \frac{\sqrt{2}(\delta C_4-\delta C_2)}{(1+h)\,C} \\ 0 & 0 & 0 & 0 \\ \frac{\sqrt{2}(\delta C_1-\delta C_3)}{(1+h)\,C} & 0 & \frac{2(\delta C_1+\delta C_3+\delta C_a+\delta C_b)}{(1+h)\,C} & \frac{2(\delta C_a-\delta C_b)}{(1+h)\,C} \\ \frac{\sqrt{2}(\delta C_4-\delta C_2)}{(1+h)\,C} & 0 & \frac{2(\delta C_a-\delta C_b)}{(1+h)\,C} & \frac{2(\delta C_2+\delta C_4+\delta C_a+\delta C_b)}{(1+h)\,C} \end{pmatrix}$$

According to time independent perturbation theory the change in the eigen value of lowest quadrupole mode is given by

$$\omega_0^{p2} = \omega_0^{u2} + c^2 \langle \widehat{U}_{q0} \mid \delta k^2 \mid \widehat{U}_{q0} \rangle \tag{4.17}$$

where p and u stands for perturbed and unperturbed eigen values. so assuming $\Delta\omega_0^2 = \omega_0^{p2} - \omega_0^{u2} = 2\delta\omega_0\omega_0$ the change in eigen value of the lowest quadrupole mode because of perturbation is given by

$$\Delta\omega_0 = \frac{c^2}{2\omega_0} \langle \widehat{U}_{q0} \mid \delta k^2 \mid \widehat{U}_{q0} \rangle \tag{4.18}$$

since $\widehat{U}_{q0} = \begin{pmatrix} 1 \\ 0 \\ 0 \\ 0 \end{pmatrix}$, so the change in the resonance frequency of the lowest quadrupole mode is given by

$$\Delta\omega_0 = -\frac{\omega_0}{8}\left(\frac{\delta C_{qq}}{C} + \frac{\delta L_{qq}}{L}\right) \tag{4.19}$$

where $\delta C_{qq} = \delta C_1 + \delta C_2 + \delta C_3 + \delta C_4$ and $\delta L_{qq} = \delta L_1 + \delta L_2 + \delta L_3 + \delta L_4$.

Therefore it is possible to write the explicitly the expression for the perturbed voltage of the RFQ as

$$\underline{\widehat{U}} = \underline{\widehat{U}}_{q0} + \underline{\widehat{\delta U}} \tag{4.20}$$

$$\underline{\widehat{U}} = \phi_{q0}\widehat{e}_q + \sum_{n=1}^{\infty} a_{qn}\phi_{qn}\widehat{e}_q + \sum_{n=0}^{\infty} a_{d1n}\phi_{d2n}\widehat{e}_{d1} + \sum_{n=0}^{\infty} a_{d2n}\phi_{d2n}\widehat{e}_{d2} \tag{4.21}$$

where $a_{qn} = c^2 \frac{\langle \widehat{U}_{qn}|\delta k^2|\widehat{U}_{q0}\rangle}{\omega_0^2 - \omega_{qn}^2}$ similarly $a_{d1n} = c^2 \frac{\langle \widehat{U}_{d1n}|\delta k^2|\widehat{U}_{q0}\rangle}{\omega_0^2 - \omega_{d1n}^2}$ and $a_{d2n} = c^2 \frac{\langle \widehat{U}_{d2n}|\delta k^2|\widehat{U}_{q0}\rangle}{\omega_0^2 - \omega_{d2n}^2}$ which is given as

$$a_{qn} = -\frac{\omega_0^2}{4(\omega_0^2 - \omega_{qn}^2)} \int_0^l \varphi_{q0}\varphi_{qn}\left(\frac{\delta C_{QQ}}{C} + \frac{\delta L_{QQ}}{L}\right)dz \tag{4.22}$$

$$a_{d1n} = -\frac{\sqrt{2}\omega_0^2}{4(1+h)(\omega_0^2 - \omega_{qn}^2)} \int_0^l \varphi_{q0}\varphi_{dn1}\left(\frac{\delta C_{Qd1}}{C} + \frac{\delta L_{Qd1}}{L}\right)dz \tag{4.23}$$

$$a_{d2n} = -\frac{\sqrt{2}\omega_0^2}{4(1+h)(\omega_0^2 - \omega_{qn}^2)} \int_0^l \varphi_{q0}\varphi_{dn2}\left(\frac{\delta C_{Qd2}}{C} + \frac{\delta L_{Qd2}}{L}\right)dz \tag{4.24}$$

where $\delta C_{QQ} = \delta C_1 + \delta C_2 + \delta C_3 + \delta C_4$ and similarly $\delta L_{QQ} = \delta L_1 + \delta L_2 + \delta L_3 + \delta L_4$, $\delta L_{Qd1} = \delta L_1 - \delta L_3$,$\delta C_{Qd1} = \delta C_1 - \delta C_3$ and similarly $\delta C_{Qd2} = \delta C_4 - \delta C_2$, $\delta L_{Qd2} = \delta L_4 - \delta L_1$

4.2.2 Case study 1:

In order to validate the pertubative theory of four-vane RFQ, we have done a case study, where one tuner of dia 4.5 cm was inserted in one quadrant of a 1 m long RFQ. The perturbation because of the tuner insertion can be calculated in two different ways

1. Assuming pertubation term is at single point (i.e., delta function error).

2. Assuming the perturbation term is distributed over the dia of the tuner.

4.2.2.1 Using delta function error:

Let us assume that tuner was inserted at a position $z = z_0$ in 1^{st} quadrant of RFQ, which leads to a change of $\delta\omega_0$ in the lowest quadrupole mode frequency. The inductance of the 1st quadrant has been changed by some amount δL_1, by assuming this perturbation to be the delta function error (i.e, it is located at a single position z). The fractional change in the eigen vector of the lowest quadrupole mode is calculated as below.

$$\delta\omega_0 = (\frac{c^2}{2\omega_0})(\frac{-\omega_0^2}{4lc^2})\int_0^l \frac{\delta L_1}{L}\delta(z - z_0)dz \tag{4.25}$$

$$\delta\omega_0 = (\frac{\omega_0}{8l})(\frac{\delta L_1}{L}) \tag{4.26}$$

where $\int_0^l \delta(z - z_0)dz = 1$. Here we assumed only the 1^{st} quadrant has been perturbed. So $\delta L_{qq} = \delta L_1$. Since we know by inserting the tuner the inductance of the quadrant decrease as a result the frequency increases. So as $L \downarrow \omega(frequency) \uparrow$. so in above equation as $\delta\omega_0$ is +ve then $\frac{\delta L_1}{L}$ is −ve. So the above equation is given by

$$\frac{\delta L_1}{L} = -\frac{8l\delta\omega_0}{\omega_0} \tag{4.27}$$

So the higher order quadrupole mode contribution in the perturbed voltage of lowest quadrupole mode is given by

$$a_{qn} = \frac{c^2}{\omega_0^2 - \omega_{qn}^2}\langle\underline{\widehat{U}}_{qn}|\delta k^2|\underline{\widehat{U}}_{q0}\rangle = -16(\frac{l}{\lambda})^2(\frac{\delta\omega_0}{\omega_0})\sum_{m=1}^{\infty}\frac{Cos(\frac{m\pi z_0}{l})}{m^2} \tag{4.28}$$

similarly the dipole contribution is given by

$$a_{qdn1} = \frac{c^2}{\omega_0^2 - \omega_{d1n}^2}\langle\underline{\widehat{U}}_{qd1n}|\delta k^2|\underline{\widehat{U}}_{q0}\rangle$$

$$= \frac{c^2}{\omega_0^2 - \omega_{d1n}^2} \frac{\sqrt{2}\omega_0^2}{4(1+h)c^2} \int_0^l \frac{\delta L_1 - \delta L_3}{L} \delta(z - z_0) Cos(\frac{m\pi z}{l}) dz$$

$$= 4\sqrt{2}(\frac{\delta\omega_0}{\omega_0}) \sum_{m=1}^{\infty} \frac{Cos(\frac{m\pi z_0}{l})}{(h - (1+h)(\frac{m\lambda}{2l})^2)} \tag{4.29}$$

Similarly for $a_{qdn0} = \frac{2\sqrt{2}}{h} \frac{\delta\omega_0}{\omega_0}$

4.2.2.2 Distributed Inductance:

Let us assume by introducing the tuner of radius **r** at centre of the RFQ in first quadrant, the inductance of the first quadrant has been changed by δL_1. which can be calculated by using the change in the area of the vacuum portion of the RFQ. The change in the frequency of TE_{210} mode is given by

$$\Delta\omega_0 = \frac{c^2}{2\omega_0} \frac{-\omega_0^2}{4c^2} \frac{1}{l} \int_{\frac{l}{2}-r}^{\frac{l}{2}+r} \frac{\delta L_{qq}}{L} dz$$

$$\Delta\omega_0 = \frac{\omega_0 \delta L_{qq}}{8L} [(\frac{l}{2} + r) - (\frac{l}{2} - r)]$$

$$\Delta\omega_0 = \frac{\omega_0 \delta L_{qq}}{4L} \frac{r}{l} \tag{4.30}$$

If we insert the tuner into the RFQ the inductance decreases as a result the frequency increases. The perturbed wave function is given as in equation 14. Whereas the coefficients are given by

$$\begin{aligned} a_{qn} =& \frac{c^2}{(\omega_0^2 - \omega_{qn}^2)} \frac{-\omega_0^2}{4c^2} \frac{\sqrt{2}}{l} \int_0^l \frac{\delta L_{qq}}{L} cos(\frac{n\pi z}{l}) dz \\ =& \sqrt{2}(\frac{l}{\lambda})^2 \frac{\delta L_{qq}}{L} \sum_{m=1}^{\infty} \frac{[sin(\frac{m\pi}{2} + \frac{m\pi r}{l}) - sin(\frac{m\pi}{2} - \frac{m\pi r}{l})]}{n^3\pi} \end{aligned} \tag{4.31}$$

$$\begin{aligned} a_{dn1} =& \frac{\sqrt{2}\omega_0^2}{4(1+h)(\omega_0^2 - \omega_{dn1}^2)} \frac{\sqrt{2}}{l} \int_0^l \frac{\delta L_{qd1}}{L} cos(\frac{n\pi z}{l}) dz \\ =& \frac{1}{2} \frac{\delta L_{qd1}}{L} \sum_{n=1}^{\infty} \frac{[sin(\frac{n\pi}{2} + \frac{n\pi r}{l}) - sin(\frac{n\pi}{2} - \frac{n\pi r}{l})]}{[h - (1+h)(\frac{n\lambda}{2l})^2]} \end{aligned} \tag{4.32}$$

$$
\begin{aligned}
a_{dn0} =& \frac{\sqrt{2}\omega_0^2}{4(1+h)(\omega_0^2-\omega_{d0}^2)} \frac{1}{l} \int_{\frac{l}{2}-r}^{\frac{l}{2}+r} \frac{\delta L_{qd1}}{L} dz \\
=& \frac{1}{\sqrt{2}h} \frac{\delta L_{qd1}}{L} \frac{r}{l}
\end{aligned}
\tag{4.33}
$$

From SUPERFISH, transverse cross sectional area of one quadrant of the 400 keV RFQ (vacuum) is 39.185 cm^2. From this,one can calculate the inductance of the RFQ, which is given by

$$
\begin{aligned}
L =& \frac{\mu_0 A}{l} \\
L =& 4.92411 * 10^{-9} Henries
\end{aligned}
\tag{4.34}
$$

where l is the length of the RFQ. From here one can calculate the capacitance of the RFQ from $C = \frac{1}{\omega_0^2 L}$. By introducing the tuner one can calculate the change in the area of RFQ vacuum portion from which one can calculate the change in inductance of the RFQ.

4.2.2.3 Results:

The simulated model of the RFQ is shown in Figure 4.3. Here in this analysis we have not considered the end cells.

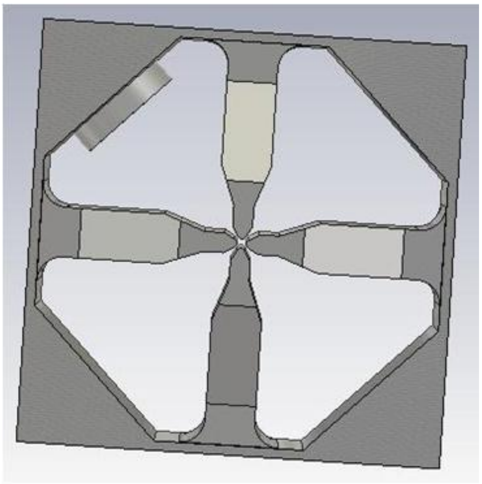

Figure 4.3: CST model of the RFQ

The tuner sensitivity was calculated to be $\sim$ 23 kHz/mm. The resonant frequency of the ideal RFQ was 348.5 MHz and by inserting the tuner by 2.7778 mm, the frequency of the RFQ was changed by $\sim$ 64 kHz. The contribution of higher quadrupole and dipole modes in the perturbed lowest quadrupole mode as calculated by the above analytical results and are compared with the field distribution obtained from the CST Microwave simulations. The field distributions are shown in Figures 4.4a and 4.4b.

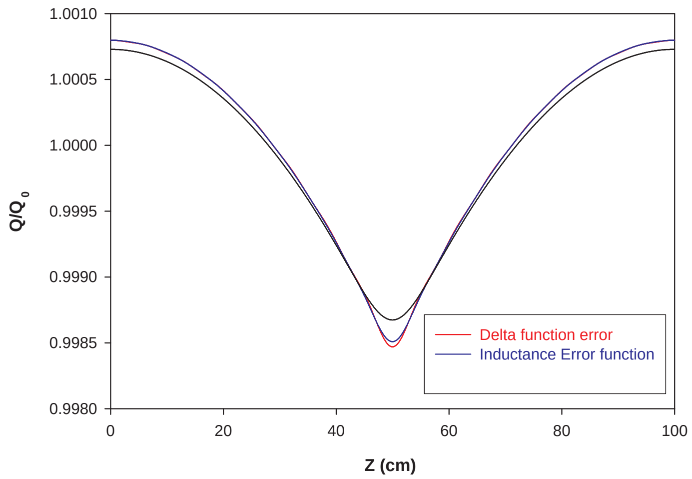

(a) Q mode

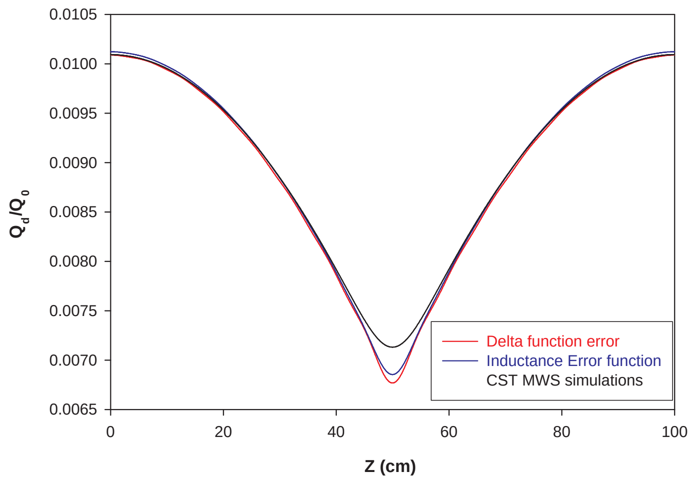

(b) D mode

Figure 4.4: Quadrupole and dipole mode distributions

By knowing these contributions one can calculate the field distributions in all the 4 quadrants by using the below equations

$$\begin{pmatrix} U_1 \\ U_2 \\ U_3 \\ U_4 \end{pmatrix} = \begin{pmatrix} \frac{1}{2} & \frac{1}{2} & \frac{1}{\sqrt{2}} & 0 \\ -\frac{1}{2} & \frac{1}{2} & 0 & \frac{1}{\sqrt{2}} \\ \frac{1}{2} & \frac{1}{2} & -\frac{1}{\sqrt{2}} & 0 \\ -\frac{1}{2} & \frac{1}{2} & 0 & -\frac{1}{\sqrt{2}} \end{pmatrix} \begin{pmatrix} U_q \\ U_m \\ U_{d1} \\ U_{d2} \end{pmatrix} \tag{4.35}$$

Now from the above equations we get

$$\begin{aligned} U_1 =& \frac{U_q + U_m}{2} + \frac{U_{d1}}{\sqrt{2}} \\ U_2 =& \frac{-U_q + U_m}{2} + \frac{U_{d2}}{\sqrt{2}} \\ U_3 =& \frac{U_q + U_m}{2} - \frac{U_{d1}}{\sqrt{2}} \\ U_4 =& \frac{-U_q + U_m}{2} - \frac{U_{d2}}{\sqrt{2}} \end{aligned} \tag{4.36}$$

The field pattern in each quadrants have been compared with the CST MW simulations and are given in Figures 4.5 4.5 (a) and (b)

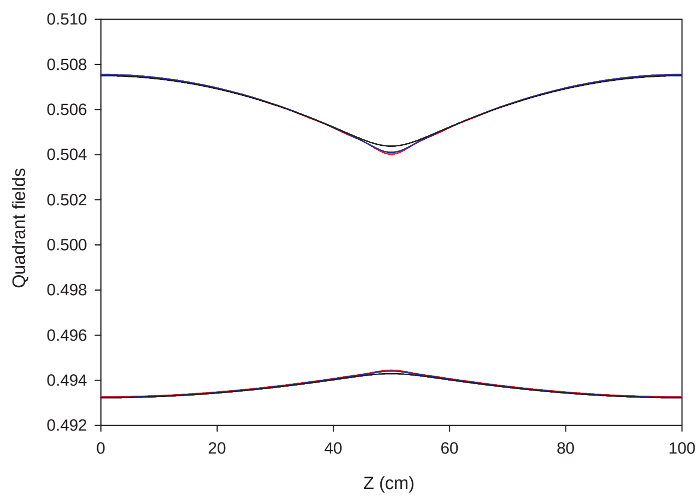

(a) Fields in 1st and 3rd quadrants of RFQ

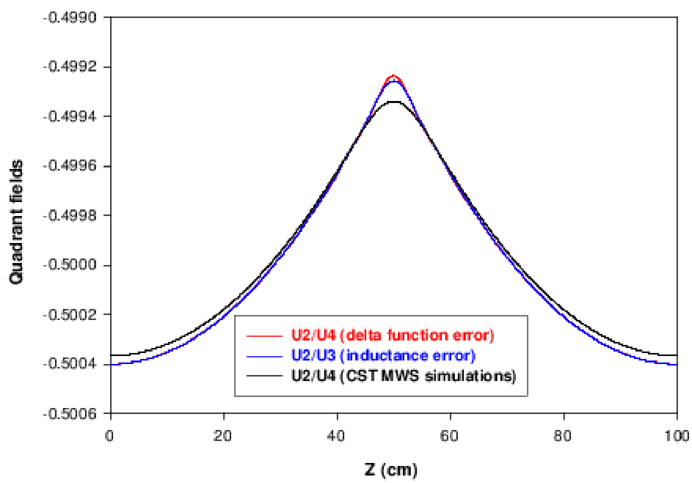

(b) Fields in 2nd and 4th quadrants

Figure 4.5: Field distribution in Quadrants of RFQ

4.3 Case study 2:

In this case study, we have inserted 16 tuners (4 per quadrant) by a depth of 1cm each and also provided the vacuum ports similar to our actual 400 keV RFQ. The pertubation term (i.e., inductance variation) because of the tuners and vacuum ports have been calculated using the computer code SUPERFISH and are used to obtain the variation of the field along the length of the RFQ. We have also simulated the similar structure using the CST Microwave studio and compared field distribution with the analytical calculations and found to be in good agreement with each other, whose results are shown in Figure4.6.

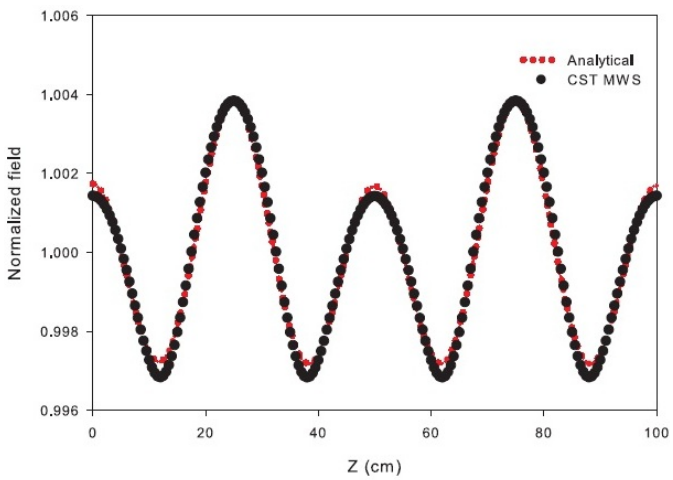

Figure 4.6: Q Field distribution

4.4 *Tuning Strategy:*

Since the perturbed field distribution in an RFQ is given as

$$\underline{\widehat{U}} = \phi_{q0}\widehat{e}_q + \sum_{n=1}^{\infty} a_{qn}\phi_{qn}\widehat{e}_q + \sum_{n=0}^{\infty} a_{d1n}\phi_{d2n}\widehat{e}_{d1} + \sum_{n=0}^{\infty} a_{d2n}\phi_{d2n}\widehat{e}_{d2} \tag{4.37}$$

In this analysis, we assume that initially the field distribution is because of the capacitive errors. From the analysis we will calculate how much inductive errors should be introduced in order to compensate the capacitive errors.

From measurements, we get $\underline{\widehat{U}}$. From above equation we can calculate a_{qn},a_{d1n} and a_{d2n}. which are given as

$$a_{qn} = \int_0^l \Delta\underline{\widehat{U}}\phi_{qn}dz \tag{4.38}$$

$$a_{d1n} = \int_0^l \Delta\underline{\widehat{U}}_{d1n}\phi_{d1n}dz \tag{4.39}$$

$$a_{d2n} = \int_0^l \Delta\underline{\widehat{U}}_{d2n}\phi_{d2n}dz \tag{4.40}$$

From perturbative analysis, we have

$$a_{qn} = -\frac{\omega_0^2}{4(\omega_0^2 - \omega_{qn}^2)} \int_0^l \varphi_{q0}\varphi_{qn}(\frac{\delta C_{QQ}}{C} + \frac{\delta L_{QQ}}{L})dz \tag{4.41}$$

Since ϕ_{qn} are basis vectors, So any function can be represented as a algebraic sum of these basis vectors. so the capacitance errors can be expressed as

$$\frac{\delta C_{QQ}}{C} = \sum_{m=1}^{Nq} b_{qm}\phi_{qn} \tag{4.42}$$

$$\frac{\delta C_{Qd1}}{C} = \sum_{m=0}^{Nd1} b_{d1m}\phi_{d1n} \tag{4.43}$$

similarly,

$$\frac{\delta C_{Qd1}}{C} = \sum_{m=0}^{Nd1} b_{d1m}\phi_{d1n} \tag{4.44}$$

Substituting these above expressions in equations 15,16 & 17, we get

$$\begin{aligned} a_{qn} &= -\sum_{m=1}^{Nq}\left(\frac{\omega_0^2}{4(\omega_0^2 - \omega_{qn}^2)}\int_0^l \varphi_{q0}\varphi_{qn}\varphi_{qm}dz\right)b_{qn} \\ a_{d1n} &= -\sum_{m=0}^{Nd1}\left(\frac{\sqrt{2}\omega_0^2}{4(1+h)(\omega_0^2 - \omega_{d1n}^2)}\int_0^l \varphi_{q0}\varphi_{d1n}\varphi_{d1m}dz\right)b_{d1n} \\ a_{d2n} &= -\sum_{m=0}^{Nd2}\left(\frac{\sqrt{2}\omega_0^2}{4(1+h)(\omega_0^2 - \omega_{d2n}^2)}\int_0^l \varphi_{q0}\varphi_{d2n}\varphi_{d2m}dz\right)b_{d2n} \end{aligned} \tag{4.45}$$

if these $a'_{qn}s$ $a'_{d1n}s$ and $a_{d2n's}$ are written as

$$\begin{aligned} a_{qn} &= -\sum_{m=1}^{Nq} C_q^{nm} b_{qn} \\ a_{d1n} &= -\sum_{m=0}^{Nd1} C_{d1}^{nm} b_{d1n} \\ a_{d2n} &= -\sum_{m=0}^{Nd2} C_{d2}^{nm} b_{d2n} \end{aligned} \tag{4.46}$$

Then

$$\begin{aligned}
C_{qn}^{nm} &= \frac{\omega_0^2}{4(\omega_0^2-\omega_{qn}^2)}\int_0^l \varphi_{q0}\varphi_{qn}\varphi_{qm}dz \\
C_{d1}^{nm} &= \frac{\sqrt{2}\omega_0^2}{4(1+h)(\omega_0^2-\omega_{d1n}^2)}\int_0^l \varphi_{q0}\varphi_{d1n}\varphi_{d1m}dz \\
C_{d2}^{nm} &= \frac{\sqrt{2}\omega_0^2}{4(1+h)(\omega_0^2-\omega_{d2n}^2)}\int_0^l \varphi_{q0}\varphi_{d2n}\varphi_{d2m}dz
\end{aligned} \tag{4.47}$$

these capacitance matrix elements can be easily calculated. The **a** vectors are calculated from the field measurements and from capacitance matrix, we can calculate b_{qn},b_{d1n} and b_{d2n} vectors.

Now in order to compensate the capacitance errors the inductances have to changed to get the required field pattern, so we have

$$\begin{aligned}
\frac{\delta L_{QQ}}{L} &= -\frac{\delta C_{QQ}}{C} \\
\frac{\delta L_{Qm}}{L} &= 0 \\
\frac{\delta L_{Qd1}}{L} &= -\frac{\delta C_{Qd1}}{C} \\
\frac{\delta L_{Qd2}}{L} &= -\frac{\delta C_{Qd2}}{C}
\end{aligned} \tag{4.48}$$

Since

$$\begin{aligned}
\frac{\delta L_{QQ}}{L} &= \frac{\delta L_1+\delta L_2+\delta L_3+\delta L_4}{L} \\
\frac{\delta L_{Qm}}{L} &= \frac{\delta L_1-\delta L_2+\delta L_3-\delta L_4}{L} \\
\frac{\delta L_{Qd1}}{L} &= \frac{\delta L_1-\delta L_3}{L} \\
\frac{\delta L_{Qd2}}{L} &= \frac{\delta L_4-\delta L_2}{L}
\end{aligned} \tag{4.49}$$

From equations 41 and 42 we can get

$$
\begin{aligned}
\frac{\delta L_1}{L} &= \frac{-\delta C_{QQ}}{4C} - \frac{\delta C_{Qd1}}{2C} \\
\frac{\delta L_2}{L} &= \frac{-\delta C_{QQ}}{4C} + \frac{\delta C_{Qd2}}{2C} \\
\frac{\delta L_3}{L} &= \frac{-\delta C_{QQ}}{4C} + \frac{\delta C_{Qd1}}{2C} \\
\frac{\delta L_4}{L} &= \frac{-\delta C_{QQ}}{4C} - \frac{\delta C_{Qd2}}{2C}
\end{aligned}
\tag{4.50}
$$

From here we will come to know the inductance as a continuous functions of position. But these variations of inductances are realized only by using discrete tuners. In particular, if the functions

$$
P_t(z) = \begin{cases} \frac{1}{\sqrt{2a}}, \; for \; z_t - a < z < z_t + a \\ 0, \;\; otherwise \end{cases} \tag{4.51}
$$

Now it is possible to project the inductance from equation 43 on this subset of functions thus obtaining the inductance variation by

$$
\frac{\delta L_{ti}}{L} = \int_0^l \frac{\delta L_i}{L} P_t(z) dz P_t(z) \tag{4.52}
$$

where, i stands for the quadrant number. Since the inductance variation is linked to the tuner depth by

$$
\frac{\delta L_{ti}}{L} = \chi \, \delta h_t \tag{4.53}
$$

Now from the above equation we can get the depth of all the tuners h_t in order to get the required field flatness.

4.5 T*uning Program:*

Based on this theory, we have written a computer program in fortran to get the tuner depths for our 400 keV RFQ. In order to validate the program, we have done a case study where we have simulated the 1 m long 400 keV RFQ with all 16 tuners inserted to a depth of 1 cm and got the quadrupole field variation along the 4 quadrants. This field distribution has served as an input to our program and calculated the depth of tuners to be removed to get the required field flatness. The output of our program is shown in Figure 4.7.

```
*****************************************************************************
*                              WELCOME TO                                *
*                                                                             *
*   Tuning algorithm for 400 keV Radio Frequency Quadrupole accelerator (RFQ)    *
*                        Gives the required tuners depth          *
*                                                                             *
*                             Developed by                                    *
*                                                                             *
*                        S.V.L.S. Rao and Kondayya Gundra
*                   (svlsr@barc.gov.in  and naiduk@barc.gov.in)
*                                                                             *
*                   Ion accelerator Development Division, BARC        *
*                        Theoretical Physics Division, BARC              *
*                             Mumbai, INDIA                                   *
*****************************************************************************
=================================================================================
)ate : 13/08/2012                              Time : 16:33:23.250
=================================================================================
 1        -9.94841
 2        -9.95520
 3        -9.96995
 4        -9.99596
 5        -9.94841
 6        -9.95520
 7        -9.96995
 8        -9.99596
 9        -9.94841
10        -9.95520
11        -9.96995
12        -9.99596
13        -9.94841
14        -9.95520
15        -9.96995
16        -9.99596
=================================================================================
```

Figure 4.7: Tuner depths

Chapter 5

RF Characterization of RFQ

5.1 Introduction:

In the previous chapters, work on the beam and cavity dynamics of RFQ has been presented. Based on the those simulations, a 400 keV RFQ made of Oxygen Free High Conductivity (OFHC) copper have been machined and vacuum brazed indigenously at BATL, Trivandrum. The brazing of the RFQ has been done in two stages. In the first stage, all the 4 vanes are brazed (i.e., copper to copper) and in second stage the ports and end flanges are brazed (i.e., copper to SS). The filler material used for brazing were Palcusil 5 (68% Ag+27% Cu+5% Pd) for first stage and Cusil (28% Cu+72% Ag) for second stage brazing. The RFQ after 1st and 2nd braze was shown in Figures 5.1 & 5.2. The complete RF charcterization has been done, which involves the measurements of resonant frequency, Quality factor (Q_0) and field distribution inside the RFQ cavity. In this chapter, we present some basics of RF parameters measurements, theory of field distrbution studies, low power tuning and beam commissioning results.

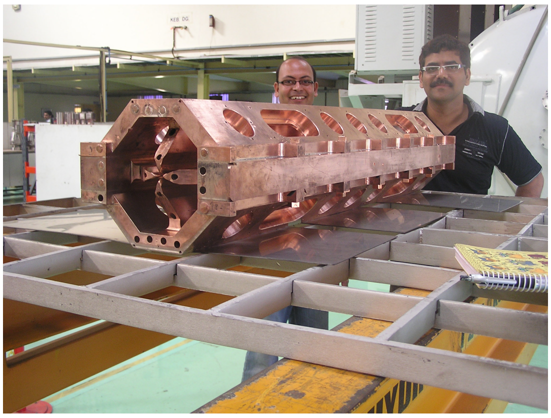

Figure 5.1: 400 keV RFQ after 1st braze

Figure 5.2: RFQ after 2nd braze

5.2 Basics of RF-structures

This section briefly describes the theory of RF parameters [53] measurements that are important in accelerators.

5.2.1 Intrinsic or Unloaded Quality Factor (Q_0)

Since the operation of the resonators is very similar to that of the lumped-element resonators of circuit theory, so the resonators can be represented as either parallel or series LCR circuits. The efficiency of the LCR circuit is given by quality factor which is defined as

$$Q_0 = 2\,\pi\,\frac{Energy\,stored}{Energy\,lost\,per\,cycle} \tag{5.1}$$

$$Q_0 = 2\,\pi\frac{U}{\tau P} \tag{5.2}$$

$$Q_0 = \frac{\omega_0 U}{P} \tag{5.3}$$

Where U is the energy stored, P is the average rate of energy loss, τ is the period of oscillation and ω_0 is the natural resonant frequency.

5.2.1.1 Closed, free-running cavity

In a closed cavity, the power loss will be equal to the rate of change of the stored energy,

$$P = -\frac{dU}{dt} \tag{5.4}$$

and from equation (5.3) $P = \frac{\omega_0 U}{Q}$, by substituting this in equation (5.4) we get

$$\frac{dU}{dt} = -\frac{\omega_0 U}{Q_0}$$

so the decay of the stored energy will be $U = U_0 e^{-t/\tau_w}$, where $\tau_w = \frac{Q_0}{\omega_0}$ is a time constant, which is defined as the time taken to reduce the stored energy by $1/e$ times of initial energy. Since the stored energy is proportional to E^2(field), The field will decay as

$$E(t) = E_0 e^{-\frac{t}{2\tau_w}} e^{i\omega t} \tag{5.5}$$

The homogeneous differential equation for a damped harmonic osciallator is given by

$$\frac{d^2E}{dt^2} + p\frac{dE}{dt} + \omega_0^2 E = 0 \tag{5.6}$$

where ω_0 is the resonant frequency when damping factor $p = 0$. Assuming a trial solution $E = E_0 e^{\lambda t}$and substituting in equation (5.6) we get

$$\lambda^2 + p\lambda + \omega_0^2 = 0 \tag{5.7}$$

the roots of equation (5.7) are given as

$$\lambda = -\frac{p}{2} \pm i\sqrt{\omega_0^2 - (p/2)^2} = -\frac{p}{2} \pm i\omega_0 \tag{5.8}$$

For $\omega_0^2 > (\frac{p}{2})^2$, the solution will be harmonic with an exponential envelope. Thus the decay of the field will be given by

$$E = E_0 e^{-(p/2)} e^{i\omega_0 t} \tag{5.9}$$

By comparing it with equation (5.5), we can get the damping factor as $p = \frac{\omega_0}{Q_0}$

5.2.1.2 Cavity with external excitation

Now consider a closed cavity excited with an external excitation force $C\, e^{i\omega t}$, the inhomogeneous damped oscillator equation given as

$$\frac{d^2E}{dt^2} + p\frac{dE}{dt} + \omega_0^2 E = C\, e^{i\omega t} \tag{5.10}$$

Assuming a trial solution $E = A\, e^{i\omega t}$ and substituting in (5.10) we get

$$A = \frac{C}{(\omega_0^2 - \omega^2) + i\omega p} = \frac{C}{(\omega_0^2 - \omega^2) + i\frac{\omega\omega_0}{Q}} \tag{5.11}$$

From the equation (5.11) it is seen that, as $\omega \to 0$ then $A \to \frac{C}{\omega_0^2}$ and as $\omega \to \infty$ then $A \to 0$. When the external frequency is close to the natural frequency (ω_0) then,

$$\omega_0^2 - \omega^2 = (\omega_0 - \omega)(\omega_0 + \omega) \approx 2\omega_0 \triangle\omega$$

$$A = \frac{C}{2\omega_0\triangle\omega + i\frac{\omega_0^2}{Q_0}} \tag{5.12}$$

Thus $\mid A \mid$is maximum when $\triangle\omega$ is zero, that is when the external frequency equals the resonant frequency of the cavity. In this case

$$A = \frac{CQ_0}{i\omega_0^2} = -i\frac{CQ_0}{\omega_0^2}$$

The $-i$ term in the above equation implies that there is a phase difference of $-\pi/2$ between the cavity fields and external excitation. Considering the equation (5.11), the square of the amplitude of the fields inside the cavity is given as

$$A^2 = \frac{C^2}{((\omega_0^2 - \omega^2)^2 + (\frac{\omega\omega_0}{Q_0})^2} \tag{5.13}$$

If the external frequency (ω) is near to the resonant frequency of the cavity (ω_0), then

$$A^2 = \frac{C^2}{(2\omega_0\triangle\omega)^2 + \frac{\omega_0^4}{Q_0^2}} \tag{5.14}$$

$$\frac{A^2}{C^2} = \frac{1}{4\omega_0^2(\triangle\omega^2 + \frac{\omega_0^2}{4Q_0^2})} \tag{5.15}$$

The quality of the resonator is characterized by the narrowness of its resonance. Let $\triangle\omega_H$ be the full width at the half height of $\mid \frac{A^2}{C^2} \mid$versus ω curve, so that

$$\mid \frac{A^2}{C^2} \mid = \frac{A_{max}^2}{2}$$

where $A_{max}^2 = \frac{Q_0^2}{\omega_0^4}$, then by equation (5.15), we get

$$\frac{Q_0^2}{2\omega_0^4} = \frac{1}{4\omega_0^2[\frac{\triangle\omega_H^2}{4} + \frac{\omega_0^2}{4Q^2}]} \tag{5.16}$$

By solving the equation (5.16), we get

$$Q_0 = \frac{\omega_0}{\triangle\omega_H} = \frac{f}{\triangle f} \tag{5.17}$$

Considering the equation (5.11) the phase angle between A and C is given by

$$A = \frac{C}{(\omega_0^2 - \omega^2)^2 + (\frac{\omega\omega_0}{Q_0})^2}\,[(\omega_0^2 - \omega^2) - i\frac{\omega\omega_0}{Q_0}] \tag{5.18}$$

the phase angle is given by

$$tan(\varphi) = -\frac{\omega\omega_0}{Q_0(\omega_0^2 - \omega^2)} \tag{5.19}$$

Thus equation (5.19) shows that when

$$\omega = 0, \varphi = 0$$
$$\omega = \infty, \varphi = -\pi$$
$$\omega = \omega_0, \varphi = -\frac{\pi}{2}$$

Now the equation (5.19) can also written as

$$cot(\varphi) = -\frac{Q_0}{\omega_0}\left[\frac{\omega_0^2 - \omega^2}{\omega}\right] \tag{5.20}$$

By differentiating the above equation wrt to frequency we get

$$-\frac{d\varphi}{d\omega}\,cosec^2(\varphi) = \frac{Q_0}{\omega_0}\left(1 + \frac{\omega_0^2}{\omega^2}\right)$$

This implies

$$-\frac{d\varphi}{d\omega} = sin^2(\varphi)\,\frac{Q_0}{\omega_0}\left(1 + \frac{\omega_0^2}{\omega^2}\right)$$

The slope of the phase near the resonant frequency is given by

$$\frac{d\varphi}{d\omega}\mid_{\omega=\omega_0}= -\frac{2Q_0}{\omega_0} \tag{5.21}$$

so from above equation, we can write $\frac{\triangle\varphi}{2Q_0} = -\frac{\triangle f}{f}$. The typical plots of $\frac{A^2}{C^2}(\frac{Q_0}{\omega_0^2})^2$ and phase (φ) vs frequency (ω) are given in Figure 5.3.

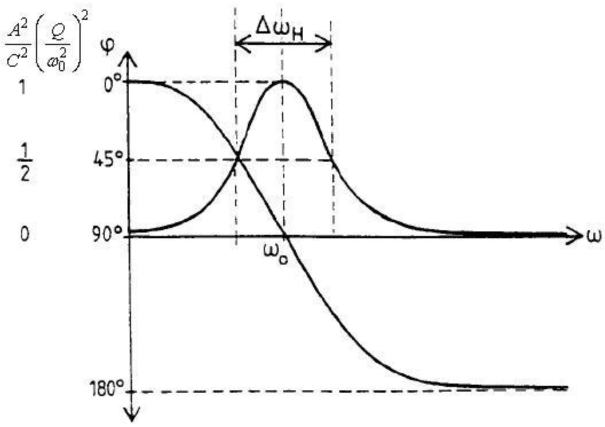

Figure 5.3: $\frac{A^2}{C^2}(\frac{Q_0}{\omega_0^2})^2$ and phase (φ) vs Frequency (ω)

5.2.2 Measurement of Resonant frequency

The Transmission method illustrated in Figure 5.4 is the simplest phenomeological measurement of resonant frequency as well as the Quality factor.

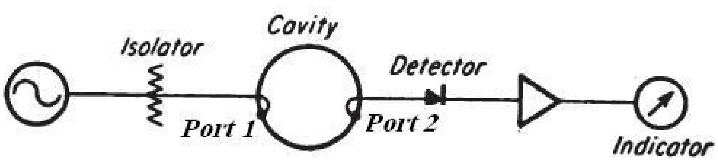

Figure 5.4: Transmission method for measuring the resonant frequency and Q value

The transmission coefficient (S_{21}) parameter [54] is defined as the ratio of reflected voltage at port 2 (V_2^-) to an incident wave of voltage at port 1 (V_1^+), when the incident waves on all ports except the 1st port are set to zero.

$$S_{21} = \frac{V_2^-}{V_1^+} |_{V_2^+=0}$$

In the microwave frequencies the voltages and current are inferred from power and phase of wave traveling in a given direction. So the transmission coefficient measured in terms of "dB" is given as

$$S_{21} = 10\, log \left(\frac{P_2^-}{P_1^+} \right) \; dB \tag{5.22}$$

Since the powers are related directly to the square of the fields amplitude ($P_2 \propto A^2$, $P_1 \propto C^2$), which implies $S_{21} \propto \frac{A^2}{C^2}$, so the variation of the S_{21} with frequency is same as shown in Figure 5.3. The frequency at which S_{21} is maximum is the resonant frequency of the structure.

5.2.3 Measurement of Quality factor

When the RF power is coupled to a resonator structure and varying the frequency around the resonance frequency, the resonance curve can be obtained as shown in Figure 5.4. The variation of square of amplitude of the fields as a function of frequency is given by equation 5.15. By calculating the difference in the frequencies where the square of amplitude of the fields becomes $\frac{A_{max}^2}{2}$, which in logarithmic scale as given by equation (5.22) corresponds to -3 dB. After measuring the full width at half maximum ($\triangle\omega_H$), the quality factor is calculated using the equation 5.17. Here it is to be noted that the value of Q calculated from above formula is intrinisic or unloaded quality factor, if the effects of the coupling loops are neglected (i.e., coupling coefficient ($\beta \ll 1$)). If β is not negligible, then the above method gives the value of loaded Q. The relation of loaded Q and Q_0 [55] is given by equation (5.23).

$$Q = \frac{Q_0}{1 + \beta_1 + \beta_2} \tag{5.23}$$

Where β_1, β_2 are the coupling coefficients of port 1 and port 2.

5.2.4 Field Measurements

The field measurements in the RF cavities are done using the perturbation methods. If the perturbation is introduced in the cavity geometry, either from the displacement of the cavity walls or from the introduction of some object, the resonant frequency will generally change and one will be interested in calculating this change. When the parameter variation because of introduction of some object inside the cavity is slow when compared to the period of oscillation. Such changes are said to be adiabatic [56]. Thus, when the parameters of the cavity are varying adiabatically, the resonant frequency is proportional to the energy of the cavity (i.e., $\frac{U}{\omega_0} = const\ or\ \frac{\triangle\omega_0}{\omega_0} = \frac{\triangle U}{U}$). This result, is known as the Boltzmann-Ehrenfest theorem [57-60]. The variation of resonant frequency, when a small volume $\triangle V$ is removed from the cavity of volume V is given by slater perturbation theory [61], which is as shown in the equation below.

$$\frac{\triangle\omega_0}{\omega} = \frac{\int_{\triangle V}\left(\mu_0 H^2 - \varepsilon_0 E^2\right)dV}{\int_V\left(\mu_0 H^2 + \varepsilon_0 E^2\right)dV} = \frac{\triangle U_m - \triangle U_e}{U} \tag{5.24}$$

Where U is the total stored energy, $\triangle U_m$ and $\triangle U_e$ are time average of the stored magnetic and electric energy removed as a result of reduced volume [53] . This theorem provides the basis for field measurements in cavities [62]. If a small spherical bead of volume $\triangle V$, is inserted into the cavity, the shift in the resonant frequency is given as a function of the unperturbed field amplitudes E and H, which are assumed to be constant over the bead, by

$$\frac{\triangle\omega_0}{\omega} = -\frac{3\triangle V}{4U}\left[\frac{\varepsilon_r - 1}{\varepsilon_r + 2}\varepsilon_0 E^2 + \frac{\mu_r - 1}{\mu_r + 2}\mu_0 H^2\right] \tag{5.25}$$

For a spherical dielectric bead, whose $\mu_r = 1$, then

$$\frac{\triangle\omega_0}{\omega} = -\frac{3\triangle V}{4U}\frac{\varepsilon_r - 1}{\varepsilon_r + 2}\varepsilon_0 E^2 \tag{5.26}$$

Thus, if the shift in the resonant frequency is measured, and the stored energy is known from measurement of the Q and the power dissipation, the magnitude of the electric field can be calculated. To measure the RF electric and/or magnetic field distributions a standard bead-perturbation technique was used.

5.3 RF Measurements

In principle, there are infinite number of modes in a resonating cavity. Now, one has to identify the required mode for acceleration of the particles. In our 400 keV RFQ, the unwanted dipolar modes (TE_{110}) frequencies are very close to the required quadrupole (TE_{210}) mode. So initially, it is important to identify the required quadrupole mode frequency.

5.3.1 Mode identification

In a RFQ at a particular position (z), the magnetic field distribution in four quadrants for quadrupole and dipole modes are as shown in Figure 5.5.

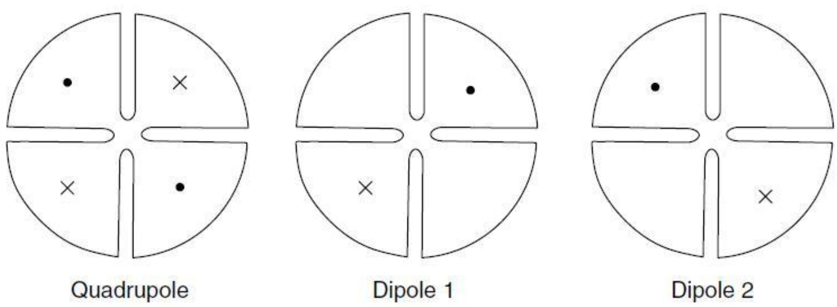

Figure 5.5: Magnetic field distribution for Quadrupole and dipole modes

For quadrupole mode, the magnetic fields in opposite quadrants are in same directions (i.e., in phase), where as for dipole modes they are in opposite direction (i.e., out of phase). So one can selectively excite either quadrupole or dipole mode, if RF power is fed simultaneously in opposite quarants in phase or out-of phase. We have used this information for identification of modes. The schematic of the apparatus is shown in Figure 5.6. We have used a 3 dB power splitter (PS) and the electrical length of the cables in the two arms of the PS same in order to have the same phase. If the loops in the quadrants are kept as shown in the Figure 5.7, we can selectively excite the quadrupole or dipole modes and the results are shown in Figure 5.8

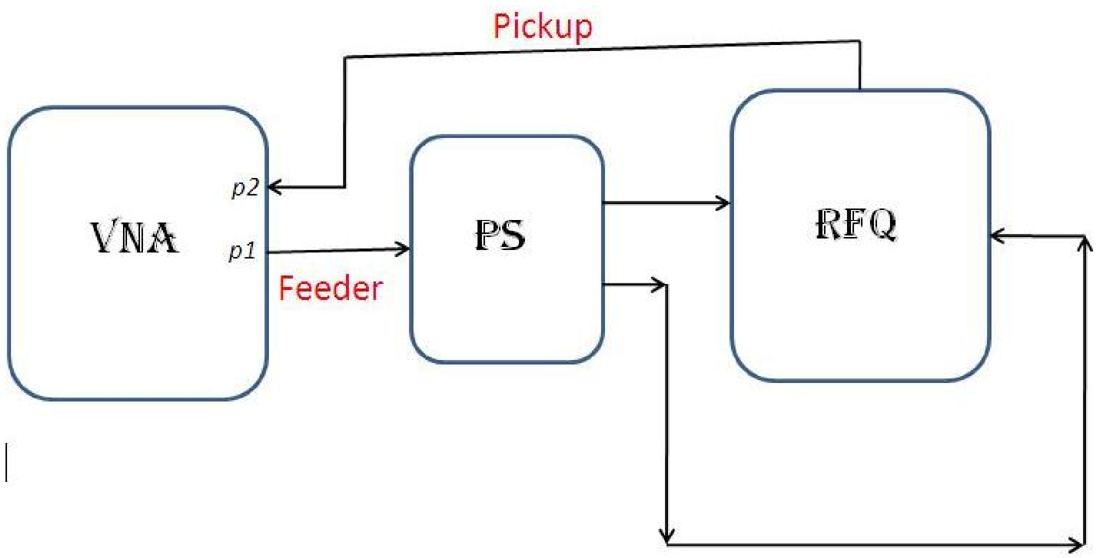

Figure 5.6: Schematic of the apparatus for mode identification

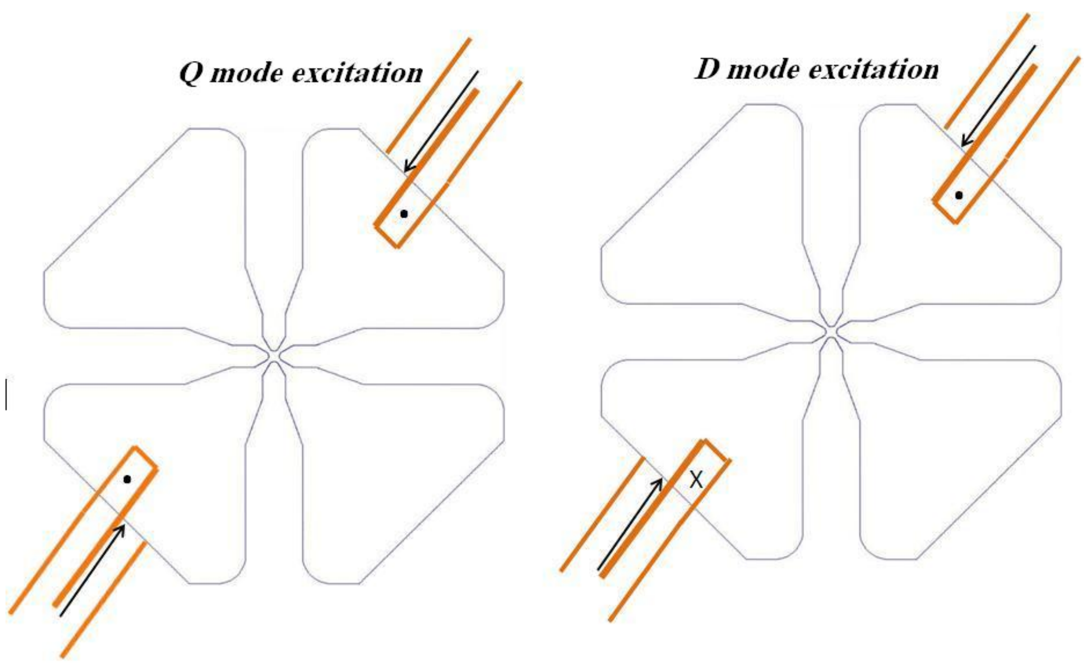

Figure 5.7: Loop orientations for mode excitations

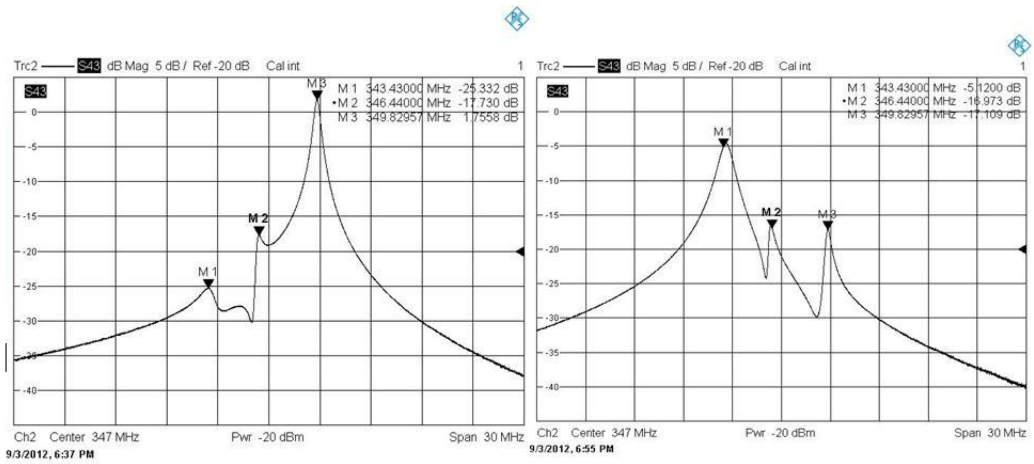

Figure 5.8: Excitation of quadrupole and dipole modes

5.3.2 Q factor measurement

We have used the transmission method discussed in section 5.2.3, for measuring the Q_0. In order to measure Q_0, the coupling coefficient ($\beta_1\, and\, \beta_2$) are made very small when compared to one, by rotating the loops. The measurement of Q_0 is shown in Figure 5.9. It was observed to be 73 % of simulated value.

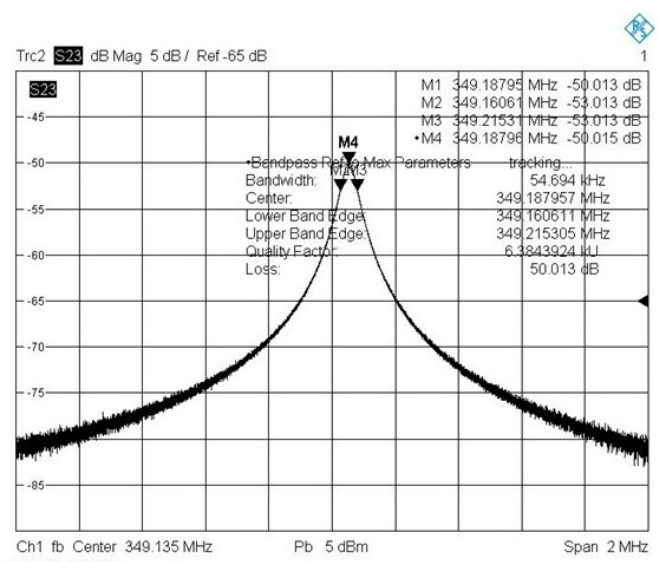

Figure 5.9: Quality factor measurement

5.3.3 Field distribution

We have used a standard bead pull technique for measuring the fields inside the cavity. The 400 keV RFQ along with bead pull measurement setup was shown in Figure 5.10. We have measured the S_{21} phase and from this phase shift ($\triangle\varphi$) one can calculate the frequency shift ($\triangle\omega$) by using the equation 5.21. By using the equation 5.25, we have calculated the field distribution.

Figure 5.10: Bead pull measurement setup

Initially, we have done the magnetic measurements using the metallic bead made of brass of dia 6 mm for the flush tuner conditions. The quadrupole resonant frequency was observed to be 348.32 MHz. The measured fields in all the four quadrants and calculated quadrupole and dipole contributions were shown in Figures 5.11 and 5.12. We have observed the fields in the quadrants 2 and 3 are less when compared to other two quadrants. By inserting the tuners in the 2nd and 3rd quadrants, we observed some improvement in the field levels in these quadrants, which are shown in Figures 5.13 & 5.14.

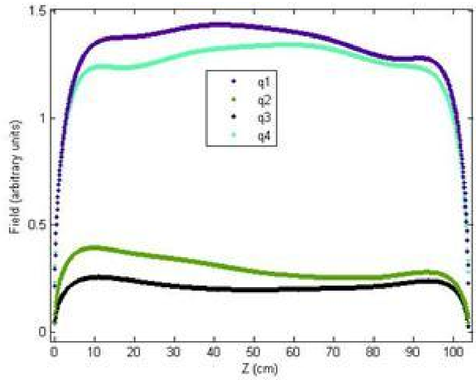

Figure 5.11: Fields in four quadrants

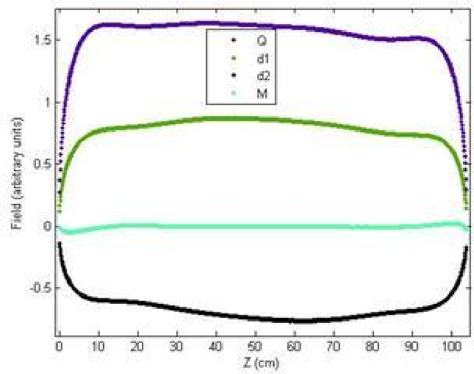

Figure 5.12: Quad and Dipole contributions

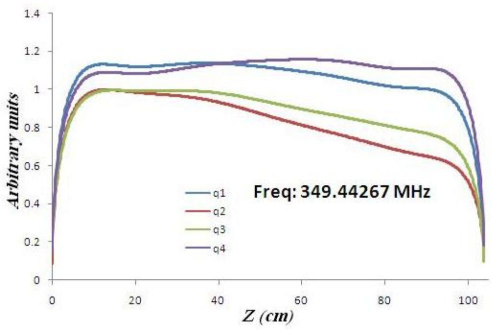

Figure 5.13: Fields in four quadrants

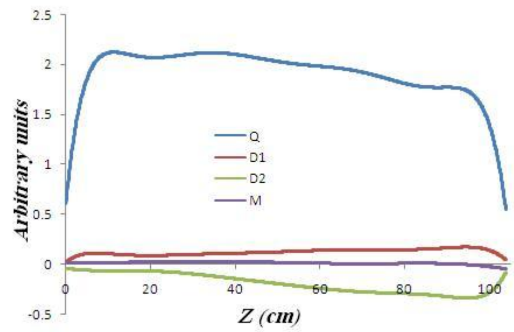

Figure 5.14: Quad and Dipole contributions

By using the tuning program, after 7 iterations, the quadrupole field levels were tuned within $\pm$ 5 % (dQ/Q0) and dipole contribution $<$ 4 % (d1/Q0, d2/Q0). The final field distribution was shown in Figure 5.15. During this tuning procedure the flat field was achieved for a resonant frequency of 352.48 MHz. In order to tune the cavity to 350 MHz, all the tuners are moved outward in order to give a frequency shift of 0.16 MHz per tuner. The depth of all tuners required to get the field flatness is given in Figure 5.16.

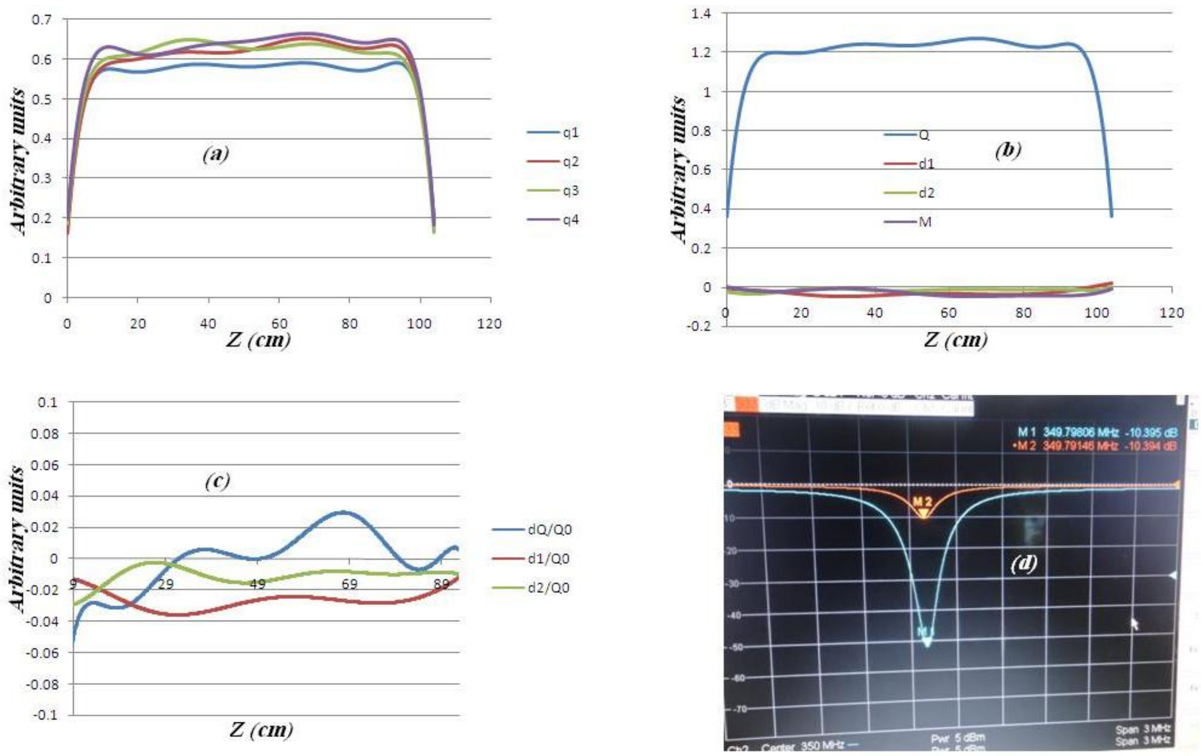

Figure 5.15: a) Field distribution in all the 4 quadrants (b) Quadrupole and dipole mode contributions in field (c) Deviation of field with average quadrupole field (d) s11, s22 reflection measurements

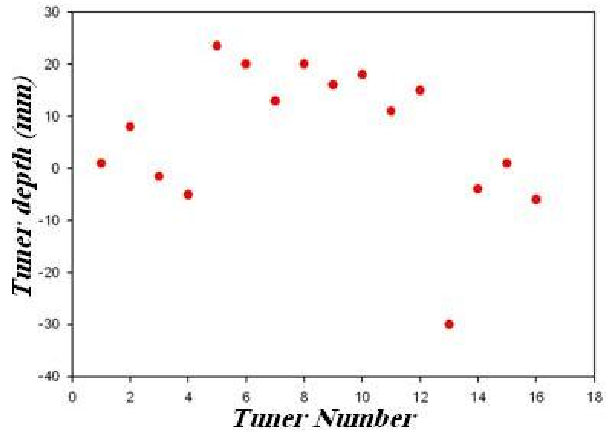

Figure 5.16: Tuners depth for all the tuners (+ve depth implies that they are inserted into the cavity, -ve implies they are retrieved back from cavity

After final tuning of the RFQ, the resonant frequencies are measured to be 349.8, 343.5 and 346.4 MHz respectively. The field measurements for all these mode have been done using bead pull setup and are shown in Figures 5.17 - 5.19. From these measurements, it is clearly seen that the resonant frequencies 346.4 and 343.5 MHz corresponds to 1-3 and 2-4 dipole modes.

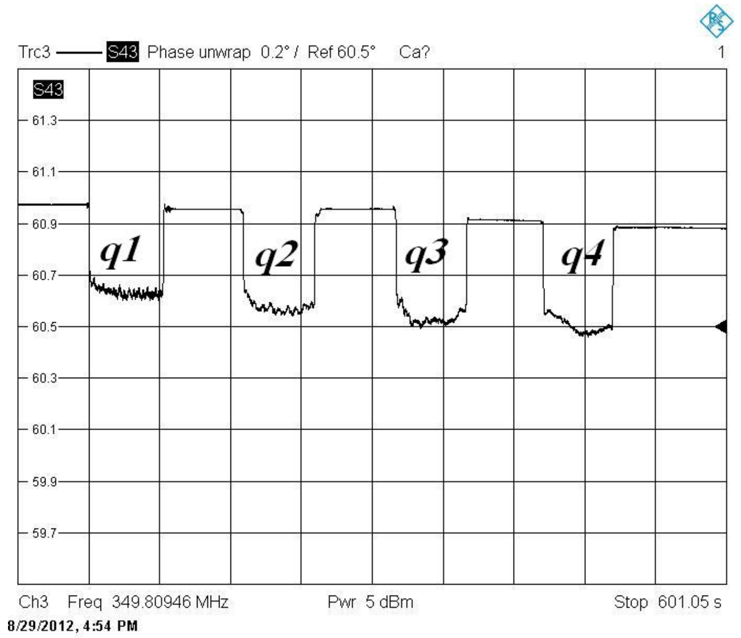

Figure 5.17: Quadrupole mode bead pull measurements

Based on the tuner depths measured after final tuning, high power slug tuners have been fabricated which are shown in Figure 5.20. After the cold testing, the thorough vacuum leak checking was done and found a minor leaks on the wall of the RFQ. In order to fix those leaks, the high temperature soldering on the RFQ walls was done. After this, the slug tuners were fixed on the RFQ and measured the resonant frequency using the reflection measurement which was shown in Figure 5.21. It was observed that all the resonant frequencies are shifted, in particular the quadrupole frequency was shifted to 349.13 MHz from 349.8 MHz.

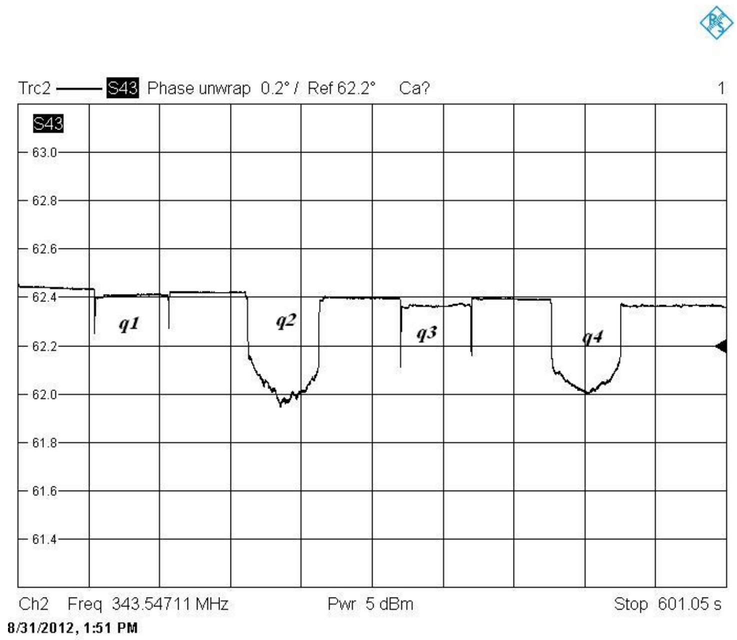

Figure 5.18: 2-4 dipole

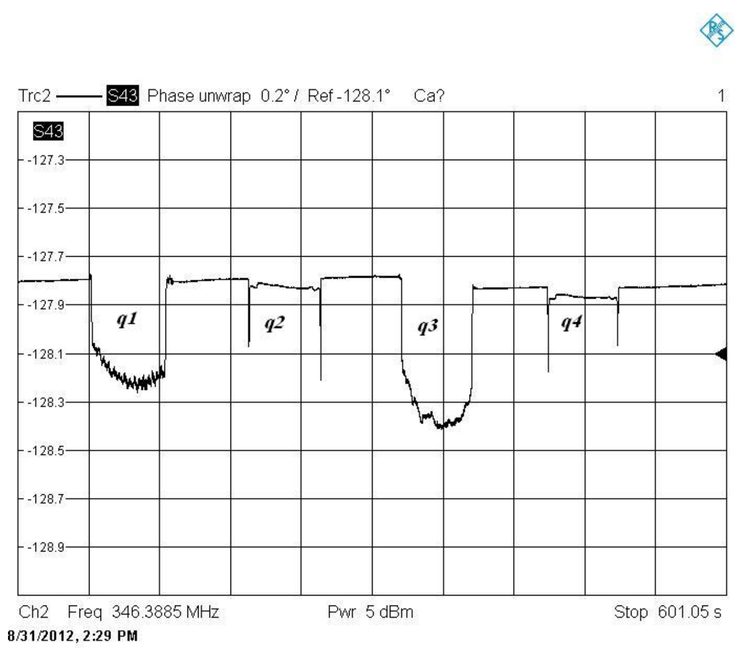

Figure 5.19: 1-3 dipole

Figure 5.20: Fixed tuners

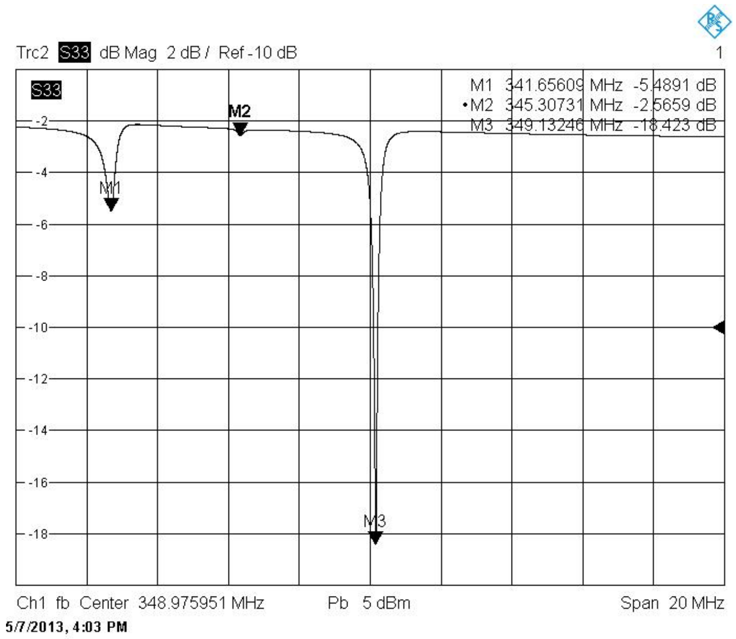

Figure 5.21: Final frequency measurement

5.3.4 Beam Acceleration

We have done simulations to accelerate the proton (H^+) beam through this 400 keV Deuteron (D^+) RFQ and found that the RF power required is 15 kW whereas for deuteron we need 60 kW. So initial beam acceleration trials were done using H^+beam.

5.3.4.1 Proton beam Acceleration

In order to accelerate the proton beam, the intervane voltage and the input energy of the beam have been changed to 22 kV and 25 keV respectively. We conditioned the RFQ in a pulsed mode with a duty factor of 0.5 % (5 ms pulse width and 1 Hz rep rate). The beam line consisting of the ion source, LEBT line, RFQ and bending magnet is shown in Figure 5.22.

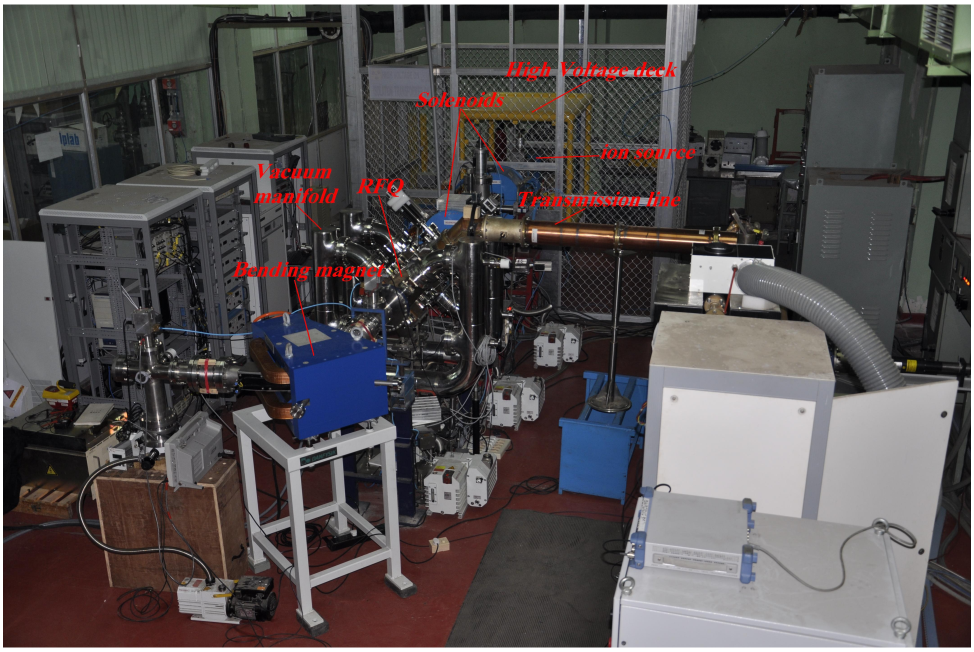

Figure 5.22: RFQ beam line

The proton beam of input energy 25 keV was injected and accelerated to 200 keV with a transmission of 70 %. The output current was measured using a faraday cup and its signal was taken on an oscilloscope which is shown in Figure 5.23. The output beam energy was measured using the 90^0 bending magnet (BM) and the result, shown in Figure

5.24, was in good agreement with simulations. After setting the magnetic field of the BM corresponding to 200 keV beam energy, the input beam energy have been varied from 20-30 keV and measured the output beam current after the bending magnet, which was shown in Figure 5.25. We have also studied, the variation of output beam current with input RF power and observed a maximum transmission at around 14.5 kW (Figure 5.26).

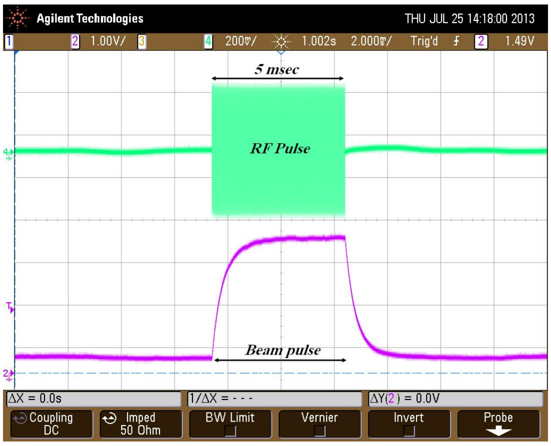

Figure 5.23: RF & Faraday cup signal

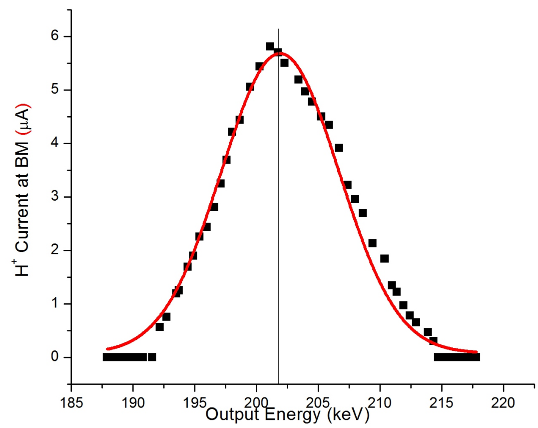

Figure 5.24: Output energy distribution

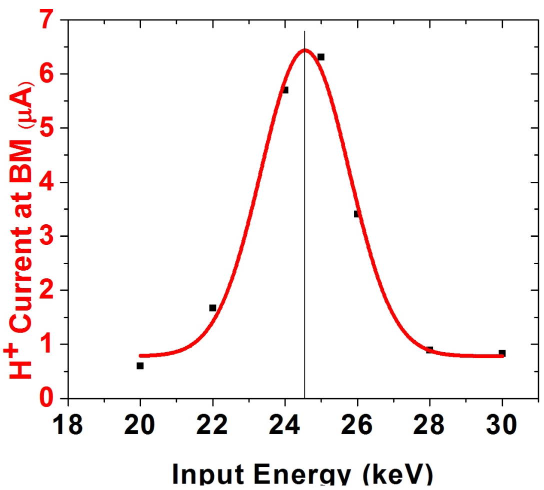

Figure 5.25: Output current vs input beam energy

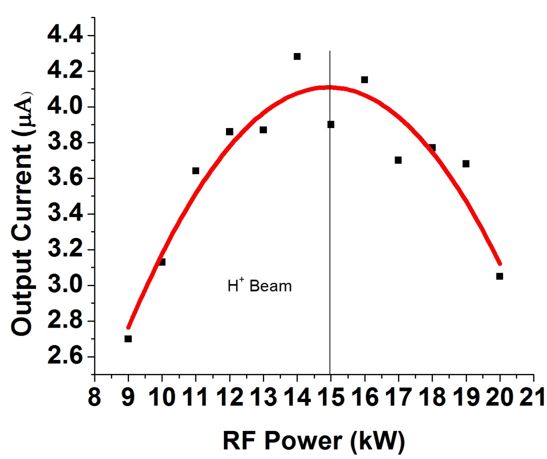

Figure 5.26: Transmission vs RF power

5.3.5 D^+ Beam acceleration

During the H^+ beam acceleration the RFQ was conditioned upto the peak power of 20 kW. Since D^+ beam needs around 60 kW of RF power, the RFQ was operated in a pulsed mode of 0.1 % duty cycle (i.e., 1 msec pulse width at 1 Hz repitition), in order to avoid the damage to the RF Coupler. It took almost two days of continuous operation to reach the peak power of 60 kW at a duty cycle of 0.1 %. Once the RFQ was conditioned, the D^+ beam of current 18 μA was injected at 50 keV and accelerated to 400 keV with a transmission of 94.5 %. The RF and the Faraday cup signals on the oscilloscope were shown in Figure 5.27. The output energy spread of the accelerated beam was measured to be $\pm$ 12 keV and is as shown in Figure 5.28.

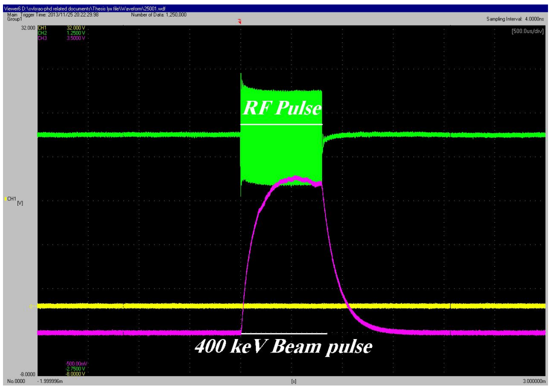

Figure 5.27: RF & Faraday cup signals

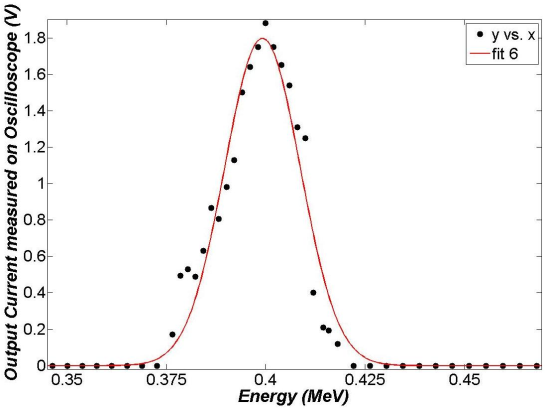

Figure 5.28: Output energy spread

Chapter 6

Design studies of LEHIPA RFQ

6.1 Introduction

As a part of our on going project LEHIPA for development of 20 MeV, 30 mA proton linac, the design studies of the 3 MeV RFQ were also done. The LEHIPA accelerator mainly consists of a 50 keV ECR ion source, a 3 MeV RFQ and a 20 MeV drift tube linac (DTL). The LEBT and MEBT are used to match the beam from ion source to RFQ and from RFQ to DTL respectively. The layout of LEHIPA is shown in Figure 1.5. The design of 3 MeV RFQ has been done, based on the conventional design procedure. The following criteria are kept in mind while designing the 3 MeV RFQ

1. Transmission $>$ 90 %
2. Length should be $\sim\ 4\,m$
3. Peak surface field $<$ 33 MV/m

The Main RFQ input parameters are given in Table 6.1. Here in this chapter, we present some of the beam and cavity dynamics simulation results of 3 MeV proton RFQ.

Table 6.1: RFQ Input parameters

Parameters	**Value**	**Units**
Particle	H^+	
I/O energy	0.05/3.00	MeV
Transverse Norm RMS emittance	0.02	$\pi\, cm - mrad$
Frequency	352.2	MHz
Current	30	mA
Total RF power	$\leq$ 500	kW

6.2 Simulation Results

We have studied two popular design stratergies as discussed in [25] and adopted similar deuteron RFQ design procedure (conventional) for our 3 MeV RFQ, because of its ease in fabrication and also in RF tuning. Based on the experience gained from our 400 keV RFQ, we have modified our RFQ design to keep the total RF power required to be less than 500 kW, after considering 50 % safety factor. Based on this criteria, the vane voltage of the RFQ was chosen to be 68 kV, and modified other parameters like modulations (m), synchronous phase (φ_s) and focusing strength (B) to keep the overall length of RFQ to be $\sim 4\,m$.

6.2.1 Beam dynamics

The beam dynamics of the RFQ was studied extensively using LIDOS [27] and cross checked with TOUTATIS [28]. The main output parameters of the RFQ are shown in Table 6.2.

Table 6.2: RFQ output parameters

Parameters	**Value**	**Units**
Particle	H^+	
Frequency	352.21	MHz
Vane voltage	68	kV
Modulation	1-1.81	
Focusing Strength (B)	5.6	MHz
Average bore radius (r_0)	0.3063	cm
Trasnverse radius of curvature (ρ_t)	0.3063	cm
Synchronous phase (φ_s)	-90/-30	deg
Output RMS emittance	0.021	$\pi\ cm - mrad$
Accelerated/Transmission	95.8/97.0	%
Length	4	m

The amount of power deposited on the vanes due to beam loss is of major concern in the CW high current RFQs, which is shown in Figure 6.1. The energy of the deposited particle should be $< 2.1\ MeV$, in order to avoid the activation of the structure. It is clearly seen from Figure 6.1, that the beam losses are concentrated near the end of GB section, where the beam energy is only 0.56 MeV and above 2 MeV there are negligible losses. The variation of various parameters like emittance, zero current phase advance (σ_{0t}, σ_{0l})and the variation of Kilpatric field along the RFQ length are shown in Figures 6.2-6.4.

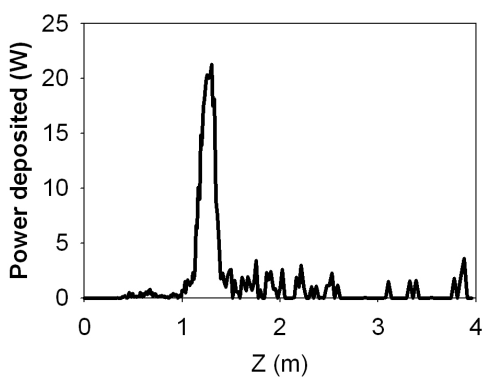

Figure 6.1: Deposited power (W) due to beam loss along the RFQ length

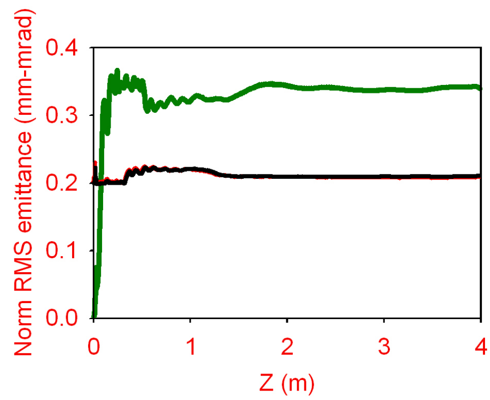

Figure 6.2: Evolution of emittances along RFQ

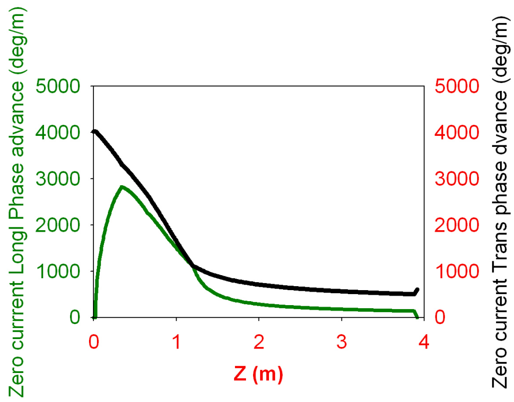

Figure 6.3: Variation of zero-current phase advances

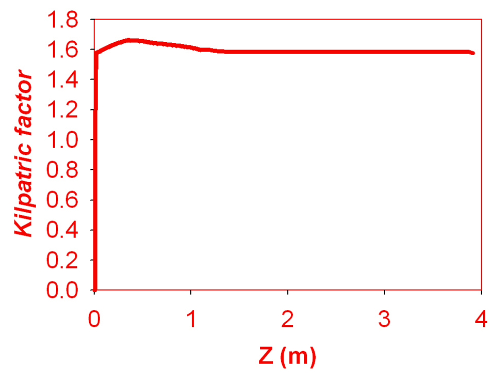

Figure 6.4: Variation of Kilpatric field

We have studied the effect of vane voltage error on the accelerated particles. Figure 6.5, shows the accelerated particles as a function of the fractional deviation of the vane voltage from its nominal value (V_{nom}) of 68 kV. It is clearly seen from the plot that a decrease in vane voltage of more than 5 % of the nominal value is unacceptable.

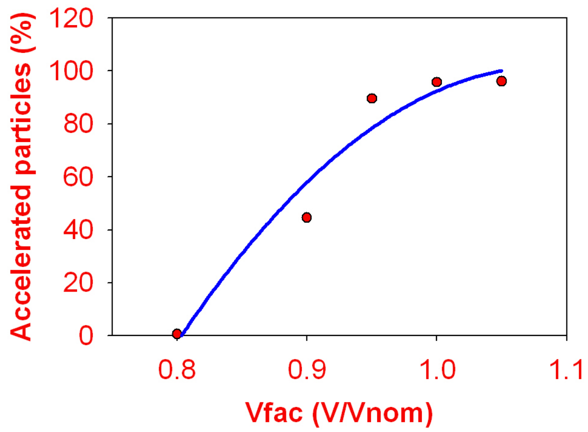

Figure 6.5: Variation of Accelerated particles with Voltage

6.2.2 Cavity dynamics

The 2D and 3D electromagnetic simulations of the RFQ cavity was done using a computer codes SUPERFISH (SF) [36] and CST Microwave studio (MWS) [37].

6.2.2.1 2D design

The geometry of the vanes for a given resonant frequency of the RFQ is obtained in 2D design using the SF. The optimization of various parameters as discussed in chapter 3, was done to reduce the power dissipation. The optimized geometric parameters of the RFQ are given in Table 6.3.

Table 6.3: Optimized geometric parameters of RFQ

Parameters	Value	Units
Average bore radius (r_0)	0.3063	cm
Vane Voltage (V_g)	68	kV

Radius of Curvature of vane tip (ρ_t)	0.3063	cm
Vane shoulder half width (W_s)	1.0	cm
Vane base half width (W_b)	1.0	cm
Corner Radius (R_c)	1.0	cm
Breakout angle (α_{bk})	0	deg
Blank width (B_w})	0.3063	cm
Blank Depth (B_d)	1.5	cm
Vane angle 1 (α_1)	16	deg
Vane angle 2 (α_2)	0	deg
Vane Heigth (H)	8.8635	cm

The main RF parameters like capacitances and inductances($C_i,\ L_i$), where $\{i = 1 - 4\}$ and C_a, C_b needed for perturbative analysis, as discussed in Chapter 4, for ideal RFQ structure are calculated from SF and are given in Table 6.4.

Table 6.4: RF parameters of RFQ

Parameters	Value	Units
Quadrupole mode	350.11	MHz
Capacitances (C_i)	32.61	$^{pF}/_{m}$
Inductances (L_i)	6.33	$nH\,m$
Dipole mode	340.07	MHz
Capacitance (C_a)	1.9549	$^{pF}/_{m}$
Dissipated power ($1.37 * SF$)	353.4	kW

The Quality factor measured for our 400 keV RFQ is 73 % of simulated value. This corresponds to 37 % increase in the dissipated power when compared to simulations. So we have considered a safety factor of 1.37 for dissipated power.

6.2.2.2 3D design

In order to study the effects of asymmetric features, like Beginning cell (BC), End cell (EC) and Coupling cell (CC) a complete 3D electromagnetic simulations are needed. Initially, we have calculated the cut-off frequency of the RFQ using Micro wave studio [37] and compared with SUPERFISH [36] simulations. For this, one quadrant of the RFQ of length 5 cm was modeled in MWS. The simulation was done with magnetic boundary condition at both the ends of the section. The comparison of the 2D and 3D simulation results are shown in Table 6.5.

Table 6.5: Comparison of RF parameters of RFQ

Parameters	SF	MWS	Units
Quadrupole mode (f_0)	350.11	350.10	MHz
Quality factor (Q_0)	10294	10306	
Max. Power density	6.402	6.45	$\frac{W}{cm^2}$
Max. Electric field (E_p)	30.43	30.79	MV/m
Max. Magnetic field (H_{max})	5123	5135	A/m
Power Lost	805.5	805.9	W

6.2.2.3 Tuners

Computer simulations using MWS were done to study the frequency variation that can be tuned with the tuners. The effect of tuners on the vane voltage profile was also studied. Figure 6.6, shows a 50 cm MWS model of one quadrant of RFQ cavity with a tuner.

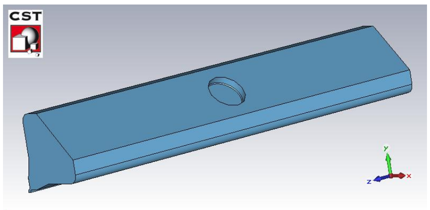

Figure 6.6: 50 cm long MWS model of RFQ with tuner

The variation of tuner frequency with the depth of the tuner is shown in Figure 6.7. From this plot, the tuner sensitivity is calculated to be $\sim 21 \frac{kHz}{mm\, tuner}$ for 1 m long RFQ, when the tuner is inserted in the RFQ. The variation of vane voltage along the length of the RFQ, when the tuner was inserted to a depth of 1 cm is also calculated from the magnetic field using the formula

$$V(z) = \omega_0 \mu_0 \int \int H_z(x, y) dx dy \tag{6.1}$$

The vane voltage is varied by only ± 0.6 %, which is shown in Figure 6.8.

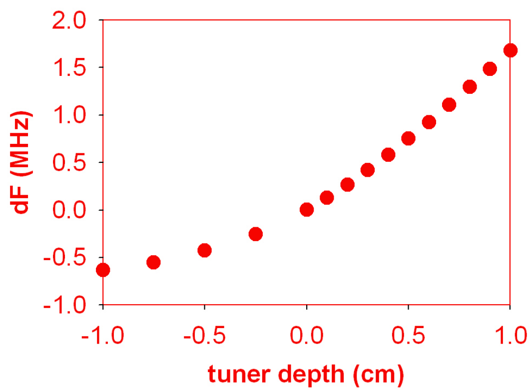

Figure 6.7: Variation of frequency with tuner depth

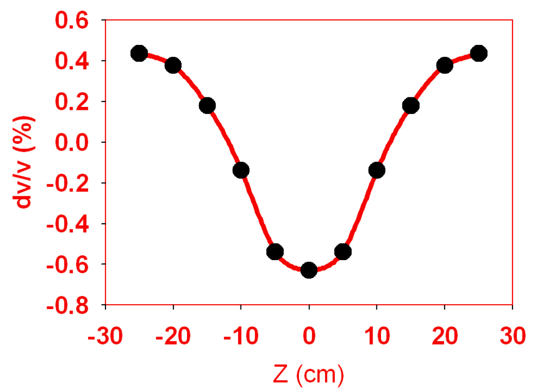

Figure 6.8: Vane voltage variation along the RFQ when tuner was inserted at z=0

We have planned to have total 64 tuners in this 4 m long RFQ. So in order to bring the resonant frequency of the RFQ to 352.21 MHz, all the 64 tuners have to be inserted by 6.25 mm each.

6.2.2.4 Beginning and end cells

In order to have the flat field profile along the RFQ, undercuts have to be provided at the both ends of the RFQ. The depths of the undercuts have to be optimized to get the same resonant frequency as the ideal RFQ cavity. The model of the undercuts is shown in Figure 6.9.The optimized parameters of the undercuts are given Table 6.6. The peak surface loss density on the undercuts is shown in Figure 6.10. The surface loss density calculated by MWS is twice the average loss as discussed in chapter 3. Power loss density is large because of sharp corners, by providing the blend edges the peak surface loss density can be reduced to $\sim 100\ \frac{W}{cm^2}$.

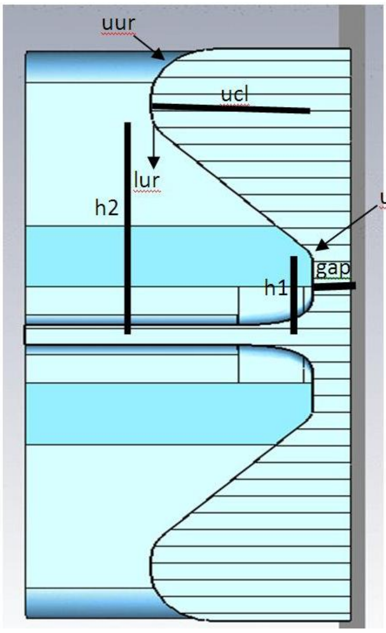

Figure 6.9: MWS mode of under cuts

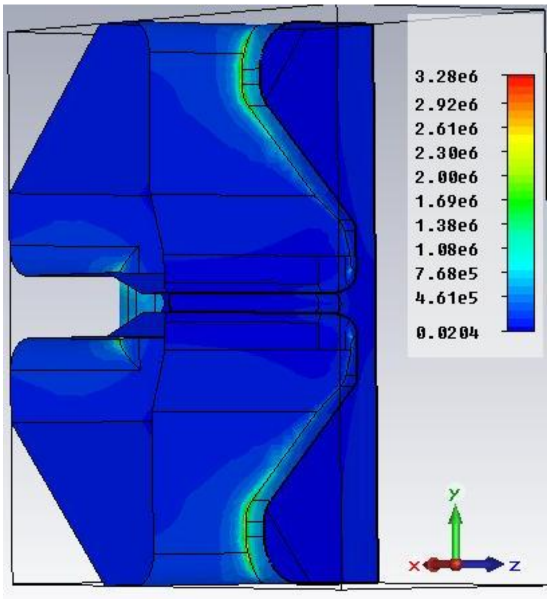

Figure 6.10: Peak Surface loss density $(\frac{W}{m^2})$

Table 6.6: Optimized parameters of BC and EC

Parameters	BC	EC	Units
End gap	0.90	0.75	cm
Overhang height (h1)	2.5	2.5	cm
Undercut length (ucl)	3.778	3.691	cm
Height (h2)	6.5	6.5	cm
Undercut tip radius (utr)	0.5	0.5	cm
Lower undercut radius (lur)	1.0	1.0	cm
Upper undercut radius (uur)	1.5	1.5	cm

6.2.2.5 Coupling cell (CC):

A single segment of 4 m long RFQ will be very unstable because the longitudinal higher-order modes (HOMs) are very close in frequency from the accelerating mode. The cavity was therefore split into two 2-m long segments, and followed the LEDA resonant coupling technique [42, 63]. The principle is to make the structure insensitive to the perturbations, which is similar to the $\pi/2$ structure in couled cavity Linacs (CCL), in which the inferior and superior modes are equally spaced in frequency from the operating mode. To design the CC gap [64], the 4-m long RFQ with a symmetry exactly at the centre of the CC gap was modelled. The schematic of the coupling cell is shown in Figure 6.11.

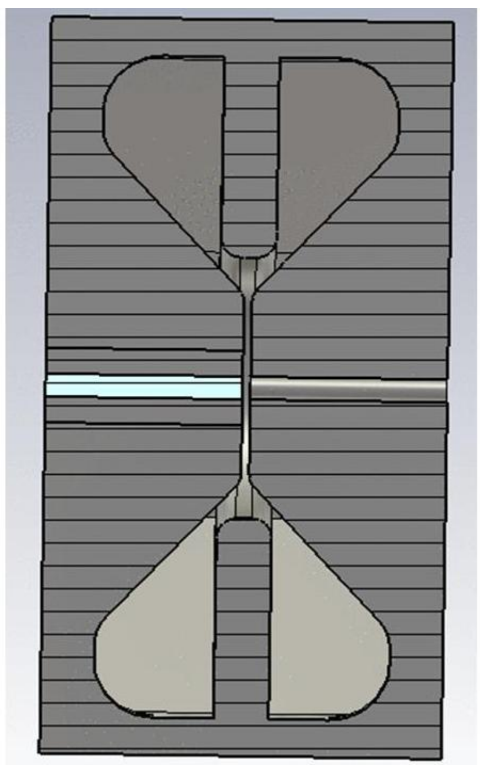

Figure 6.11: Simulation model of CC

The variation of the mode frequencies with gap is shown in Figure 6.12. It was observed that the inferior and superior modes are separated equally from the operating mode for a gap of 1.2 mm.

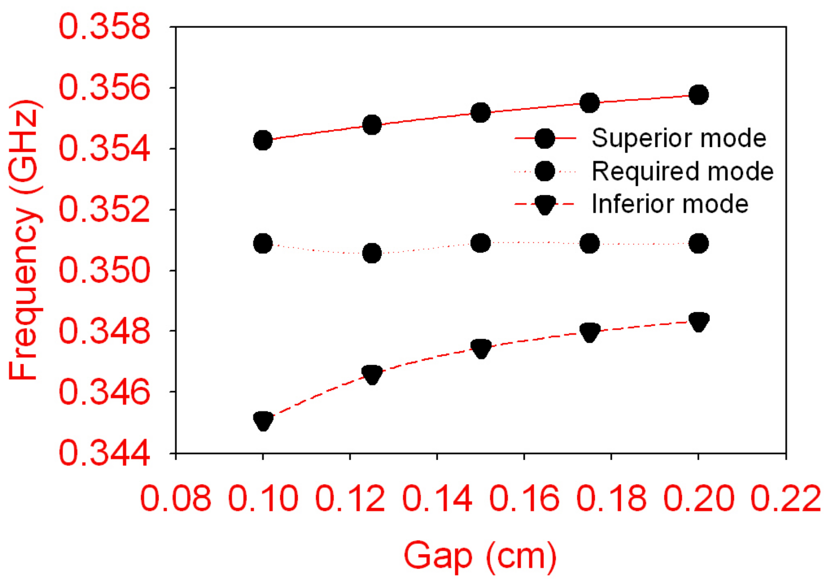

Figure 6.12: Variation of mode frequencies with gap

The cell parameters have therefore been optimized with a gap value of 1.2 mm and are shown in Table 6.7.

Table 6.7: Optimized parameters of CC

Parameters	CC	Units
Gap between vanes	1.2	mm
Overhang height (h1)	2.0	cm
Undercut length (ucl)	3.934	cm
Height (h2)	6.5	cm
Undercut tip radius (utr)	0.5	cm
Lower undercut radius (lur)	1.0	cm
Upper undercut radius (uur)	1.5	cm
Coupling plate thickness	1.4	cm
Coupling plate radius	3.0	cm

These coupling gaps have a significant effect on the beam dynamics and are studied using the computer code TOUTATIS. It was observed from the simulations that the power of lost particles has increased at the coupling gap position and is shown in Figure 6.13.

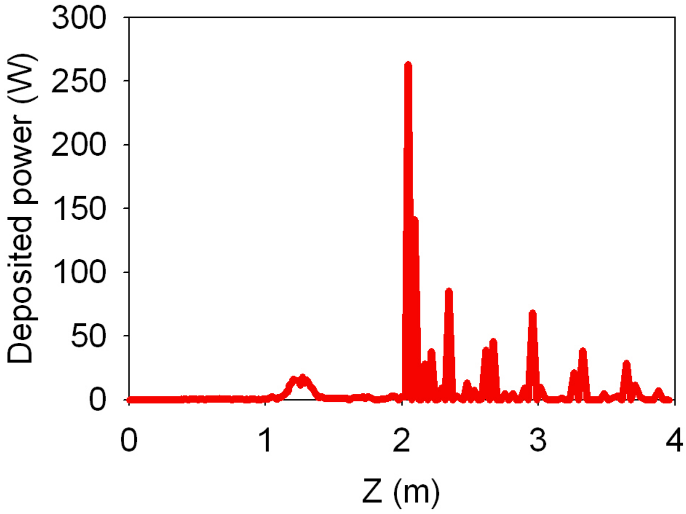

Figure 6.13: Deposited power along RFQ with Coupling gaps

Chapter 7

Summary and Future work

7.1 Summary

The work in this thesis comprises of design and development of the 400 keV Deuteron RFQ and design studies of a 3 MeV proton RFQ for LEHIPA at BARC.

Two popular design strategies are studied, and adopted the conventional method proposed by LANL [17] for both the RFQs. The main criteria was to maximize the transmission through the RFQ with minimum emittance growth and with less RF power. The 400 keV deuteron RFQ operates at a resonant frequency of 350 MHz, and needs an intervane voltage of 44 kV to accelerate the beam to final energy of 400 keV over a vane length of 1.03 m for a power loss of $\sim$ 55.5 kW (including 30 % safety factor). However, the provision for two RF sources of 60 kW each has been made, in order to manage the excess unexpected power loss. The effects of mechanical errors on the field distribution, are studied using a perturbative analysis based on 5- wire transmission line theory proposed by LNL [50]. A tuning program has been developed for this RFQ based on the algorithm given by LNL [51]. Based on these simulations, a 400 keV RFQ made of OFHC copper have been machined and vacuum brazed indigenously at BATL, Trivandrum. The complete RF characterization of this RFQ has been done. The quality factor (Q_0) has been measured and observed to be 73 % of the simulated value. This corresponds to a safety factor of 37 % for power loss, which is less than our estimated RF losses. The field distribution in the RFQ has been measured using the bead pull setup. With the help of tuners and after 7 iterations, the quadrupole field levels were tuned within $\pm$5% (dQ/Q0) and dipole contribution $<$ 4 % (d1/Q0, d2/Q0).

In order to do the beam acceleration trials through this 400 keV RFQ a beam line was setup. This mainly consists of a RF ion source, a LEBT system and a 400 keV RFQ. We have accelerated H^+, $H_2^+ \, and \, D^+$ beams from this RFQ. In order to accelerate the H^+ beam through this RFQ, the input beam energy and the intervane voltage has to be halved when compared to $H_2^+ \, and \, D^+$ beams. Since the intervane voltage is halved the RF power needed is only $1/4^{th}$ of the power needed for D^+ beam, which corresponds to ~15 kW. So initially, the proton beam was accelerated through the RFQ and obtained a transmission of ~ 70 % at a duty cycle of 0.5 % (5 msec pulse width and 1 Hz repetition). After successful acceleration of H^+ beam, the RFQ was conditioned to 60 kW peak power at a duty cycle of 0.1 % (1 msec pulse width and 1 Hz repetition) and then injected H_2^+ and D^+ beams. The transmission has been measured to be 80 % forH_2^+ and 94 % for D^+. They were in good agreement with the simulations

A 3 MeV, 30 mA RFQ has been designed for the LEHIPA project, which will be used as a front-end injector for 1 GeV accelerator for Indian ADS programme. The LEHIPA, 20 MeV proton accelerator mainly consists of a 50 keV ECR ion source, a 3 MeV RFQ and a 20 MeV DTL. This RFQ needs an intervane voltage of 68 kV to accelerate the beam to final energy of 3 MeV over a length of 4 m. The total RF power required is 453 kW with a safety factor of 37 % on the dissipated power. The effect of various types of errors on beam transmission and beam quality has been studied.

7.2 Scope of future work

The LEHIPA RFQ has been designed as reported in this thesis. Based on this design, the various components are under fabrication. The LEHIPA RFQ is a 4 m long structure, which we planned to make in 4 sections of 1 m each and couple them via a coupling cell. The behaviour of the beam at these couplings cells is a matter of concern because the power of the lost particles have increased as shown in Figure 6.13. So, the next step is to understand this effect and try to minimize the losses. We have developed a tuning program for our 400 keV RFQ, which is relatively simple structure as compared to 3 MeV RFQ. This tuning program has not taken into consideration the coupling cell. A more generalized tuning program has to be developed which can into account all the components of RFQ.

Design of high intensity linacs is complex and there are lot of grey areas, where theoretical understanding is required (for example beam halos [65]). The beam halos are identified as one of the dominant loss mechanisms in high intensity linacs. The reason for beam halos is not fully understood, but one of the most probable resons for halo formation is non-linear space charge forces acting on the mismatched beams [66]. These are initiated at low energy section of high intensity accelerators and results in beam loss at high energies. Understanding the behaviour of mismatched high current beams in the low energy part of the accelerator is essential, if one wants to build a high intensity accelerators. Since all the high current accelerators that are proposed, have chosen an RFQ as a initial accelerating structure, one has to design this part very carefully. This will improve the overall performance of high current linacs.

Bibliography

1. J D Cockroft and E T S Walton, Nature 129 (1932) 242.
2. R J Van de Graaff, K T Compton and L C Van Atta, Phys. Rev. 43 (1933) 149
3. R J Van de Graaff, Nucl. Instrum. Method. 8 (1960) 195.
4. G Ising, Ark. Mat. Fys. 18 (No. 30) (1924) 1.
5. R Wideroe, Arch. Electrotech, 21 (1928) 387.
6. D H Sloan and W M Coate, Phys. Rev. 46 (1934) 539.
7. L W Alvarez, Phys. Rev. 70 (1946) 799.
8. E O Lawerence and Edlefsen N E., (1930) Science 72, 376.
9. H. Nifenecker, O Maplan and S David, Accelerator-driven subcritical reactors, Institute of Physics, Series in Fundamental and applied nuclear physics, June 1, 2003.
10. National Spallation Neutron Source, NSNS/CDR-2/VI, May 1997.
11. J Vervier (GANIL): EURISOL, Preliminary design study of the next-generation European ISOL radioactive nuclear beam facility, Contract Number HPRI-1999-CT-50001
12. I M Kapchinskii and V A Tepliakov, Prib. Tekh. Eksp. 2, 19 (1970)
13. Conceptual Design Report of 400 keV D^+ RFQ for PURNIMA Sub-Critical Facility, Shweta Roy, T Basak, Rajni Pande, S V L S Rao, M Aslam, P Jain, P Singh, P K Neam, S Kailas and V C Sahni, BARC/2005/I/005.
14. P Singh, Status of the LEHIPA Project at BARC, InPAC-2006, Nov 1-4, 2006, BARC, Mumbai, p. 50.

15. L. Zikovsky, Neutron Activation Analysis, Course 6.2, Chulalongkorn University, http://nuceng.ca/canteachvba/nL.%20zikovsky.htm

16. S S Kapoor, Road map for development of accelerator driven sub-critical reactor systems, BARC/2001/R/004.

17. K R Crandall, R H Stokes and T P Wangler, RF Quadrupole beam dynamics design studies, Proceedings of 1979 Linear Accelerator Conference (Brookhaven National Laboratory, Upton, Ny, 1980), BNL-51134, p. 205; LANL Manual of RFq design codes (Los Alamos National Laboratory Report LA-UR-96-1836 (revised February 12, 1997).

18. John Staples, Reducing RFQ Output Emittance by External Bunching, Particle Accelerators, 1994, Vol. 47, pp. 191-199.

19. Shane Koscielniak, Reducing Longitudinal Emittance Growth in RFQ Accelerators, 17th International Linac Conference -LINAC 94, Tsukuba, August 21-36.

20. X Q Yan et al, Nucl. Instrum. Methods in Phys. Res A 554, 132 (2005)

21. X Q Yan et al, Nucl. Instrum. Methods in Phys. Res A 577, 402 (2007)

22. Chuan Zhang et al, Nucl. Instrum. Methods, in Phys. Res. A 586. 153 (2008)

23. R A Jameson et al, Scaling and optimization in high-intensity linear accelerators, LA-CP-91-272, Los Alasmos National Laboratory, July 1991 (Introduction of LINACS design code)

24. R A Jameson, An approach to fundamental study of beam loss minimization, edited by Y K Batygin, AIP Conference proceedings 480, Space Charge Dominated Beam Physics for Heavy Ion Fusion, Saitama, Japan, 1998

25. S V L S Rao and P Singh, Design studies of a high-current radiofrequency quadrupole for accelerator-driven systems programme, Pramana -J. Physics, Vol. 74, No. 2, pp. 247-259 (2010).

26. LIDOS, A Computer Code for Beam Dynamics of RFQ Linac, Version 1.1

27. TOUTATIS, A Computer Code for Beam Dynamics of RFQ Linac, Version 1.3

28. T P Wangler, Space-Charge Limits in Linear Accelerator, LA-8388.

29. John W Staples, RFQ's-AN INTRODUCTION', LBL-29472, 1990.

30. A Schempp, Radio-Frequency Quadrupoles, CERN Accelerator School, CERN 92-03, Vol II, p. 522

31. Delayen, et al., Design and Modeling of Superconducting RFQ Structures, Proc. of the 1992 Linear Accel. Conf., Aug.24-28, 1992, Ottawa, Ontario, Canada, pp. 692-694.

32. Shepard, et al., Design for a Superconducting Niobium RFQ structure, Proc. of the 1992 Linear Accel. Conf., Aug. 24-28, 1992, Ottawa, Ontario, Canada, pp 441-443.

33. Donald A., Swenson, Wayne, Cornelius and Young, P.E., Segmented Vane Radio-Frequency Quadrupole Linear Accelerator, United States Patent 5, 430, 359, filed Nov. 2, 1992, Date of Patent July 4, 1995.

34. Andreev V A and Parisi G, 900 Apart Stem RFQ Structure for Wide Range of Frequencies, Proc. of 1993 Part. Accel. Conf., Washington DC, May 13-18, pp. 3124-3126.

35. Ostroumov P N and Kolomiets A A, Design of 57.5 MHz CW RFQ for medium energy heavy ion superconducting linac, Phys. Rev. Spec. Top. Accel. Beams 5, 060101 (2002).

36. J H Billen and L M Young, Poisson, Superfish, LA-UR-96-1834, LANL

37. CST Microwave studio, Simulation tool for the electromagnetic analysis and design, CST, Germany

38. J C Slater, Microwave electronics (Van Nostrand, New York, 1950) p. 81

39. M Vretenar, RF Cavities design codes and their application to the design of RFQs, CERN/PS 90-11 (RF-HI)

40. H R Schneider, H Lancaster, Improved Field Stability in RFQ structures with Vane-Coupling Rings, IEEE Trans. Nucl. Sci NS-30(4) (1983) 3007.

41. A Ueno et al., New Field Stabilization Method of a Four-Vane Type RFQ, Nuclear Instruments and Methods in Physics Research A300 (1991) 15-24.

42. L M Young, Segmented Resonantly Coupled Radio-Frequency Quadrupole, PAC'93, May 17-20.

43. F Grespan et al., Dipole stabilizers for a four-vane high current RFQ: Theoretical analysis and experimental results on a real-scale mode, NIMA, Volume 582, Issue 2, Pages 303-317.

44. CAI Jin-Chi et al., Design of undercuts and dipole stabilizer rods for the CPHS RFQ accelerator, CPC (HEP & NP), 2012, 36(5): 464-468.

45. T P Wangler, Principles of RF Linear Accelerators, (Wiley, New York, 1998)

46. R M Hutcheon, An Equivalent circuit model of the general 3-Dimensional RFQ, IEEE Transactions on Nuclear Science, Vol. NS-30, No. 4, August 1983

47. M Vretenar, RFQ field stabilization, CERN/PS 87-56 (LI) 1987

48. A Palmieri et al., Perturbation Analysis of Coupled RFQ's, TRASCo RF note 03/02.

49. Alain France et al., Theoretical Analysis of a Real-life RFQ using 4-Wire line model and the theory of differential operators, Proceedings of EPAC 2002, Paris, France.

50. A Palmieri et al., Perturbation Analysis of a four-vane RFQ, Proceedings of IPAC'10, Kyoto, Japan.

51. A Palmieri et al., The IFMIF RFQ real-scale Aluminium Model: RF Measurements and Tuning, Proceedings of IPAC'10, Kyoto, Japan.

52. G Franceschetti, Campi Electromagnetici (in Italian).

53. Klein H., CERN Accelerator School on RF Engineering for Particle Accelerators, CERN 92-03, Vol. 1, 1992, p. 112-118.

54. David M Pozar, Microwave Engineering, 2nd ed., John Wiley & Sons.

55. Edward L Ginzton, Microwave measurements., McGRAW-HILL book company, 1957, p. 403-405

56. Landau L D and Lifshitz E M., Statistical Physics, 2nd ed., Pergamon Press, 1970, p. 38.

57. Boltzmann L., Vorlesungen uber Mechanik II, J.A. Barth, Leipzig,1903, p. 48.

58. Ehrenfest P., Ann. Phys. 36, 91 (1911).

59. Ehrenfest P., Proc. Amsterdam Acad. 16, 591 (1914).

60. Maclean W R., Q. Appl. Math. 2, 329 (1945)

61. Slater J C., Microwave Electronics, D. Van Nostrand Company, New York, 1950, pp. 80-81.

62. Maier L C., Jr. and Slater J C., J. Appl. Phys. 23(No.1), 68-83 (1952).

63. J Browman et al, Couple RFQs as compensated structures, Linac90, Albuquerque, p. 70.

64. A Pisent, R Celentano R Zennaro, Equivalent Lumped Circuit Study for the field stabilization of a long four-vanes RFQ, Linac 1998, p. 968.

65. C K Allen and T P Wangler, Beam halo definitions based upon moments of the particle distribution, Phys. Rev. ST AB, Vol. 5, 124202 (2002).

66. T P Wangler et al., Dynamics of Beam Halo in Mismatched Beams, Proceeding of Linac 96, Geneva, August 26-30.